Petrology and Geochemistry of Selected Quaternary Volcanoes from Vardenis Volcanic Highland (South Armenia)

Thomas Ronayne

Student ID: 201202428

Supervisor: Dr I. Savov

Submitted in accordance with the requirements for the degree of

MSc by Research.

University of Leeds

Institute of Geophysics and Tectonics, School of Earth and Environment, Leeds

December 2022

Word count: 12,558

Acknowledgements

This thesis has been completed under the guidance of my supervisor Ivan Savov, who has helped me greatly to make this the piece of work it is today.

I was also assisted extensively by lab manager Jason Harvey, who showed me how to conduct the lab-based research required for this thesis.

I would like to thank my fellow post-graduate research students, especially Eilish Brennan, who offered me support throughout my project, especially when I was struggling with external issues.

Samuele Agostini and the team at CNR Pisa, who showed me how to complete my boron analysis and were very welcoming during my time in Italy.

Khachik Meliksetian and the team in Armenia, for showing me some of the amazing volcanology in their country and for organising our fieldwork.

Abstract

Vardenis Volcanic Highland (VVH) is a region in Armenia that plays host to continental collision zone volcanism and is part of the wider Lesser Caucasus Volcanic zone. The new dataset presented here aims to further our understanding of the petrological and geochemical complexities of this highland, aiming to bring this under-researched area onto parr with the comparatively well-studied adjacent regions of E. Anatolia and S. Armenia (Syunik and Gegham). A $\delta^{11}B$ range of -5.8 to -1.5‰ (as well as other trace element metrics) corroborates the previously determined pre-collisional (subduction) signature thought to be imparted to the mantle source by a sediment melt. The generally low [B] values (1.4-7.2ppm) indicate a dehydrated source, which combined with the range of $\delta^{11}B$, highlights a distinctive mantle reservoir. The Sr-Nd isotope systematics for the new VVH dataset also show significant overlap between VVH and Syunik, extending the outline of the enriched mantle domain under the Armenian part of the Lesser Caucasus.

Abbreviations

AECZ – Arabia-Eurasia Collison Zone
AOC – Altered Oceanic Crust
BCC – Bulk Continental Crust
B-P – Bitlis-Pütürge
BSE – Bulk Standard Earth
B-Z – Bitlis-Zagros
DMM – Depleted MORB Mantle
EMPA – Electron Microprobe Analysis
GCB – Greater Caucasus Basin
GLOSS – Global Subducting Sediment
GVH – Gegham Volcanic Highland
HFSE – High Field Strength Element
IAEA – International Atomic Energy Agency
ICP-ES – Inductively Coupled Plasma Emission Spectrometer
ICP-MS – Inductively Coupled Plasma Mass Spectrometer
LILE – Large Ion Lithophile Elements
LREE – Light Rare Earth Elements
MNPP – Metzamor Nuclear Power Plant
MORB – Mid-Ocean Ridge Basalt
MSF – Melt or Supercritical Fluid
P-T – Pressure-Temperature
REE – Rare Earth Elements
SAB-ATA – South Armenian Block-Taurides-Anatolides
SEM – Scanning Electron Microscope
SLC – Southern Lesser Caucasus
SVH – Syunik Volcanic Highland
TAC – Tezhsar Alkaline Complex
TAS – Total Alkalis vs Silica
TIMS – Thermal Ionisation Mass Spectrometry
VVH – Vardenis Volcanic Highland

Contents

Figures & Tables

1. Introduction

Modern continent-continent collision zones are not known for being volcanically active. Typically, only active deformation (orogenesis) and seismic activity dominate such regions (Schoenbohm, 2013). However, the Arabia-Eurasia collision zone (AECZ) (Figure 1.1) presents an anomaly to this trend, with widespread volcanism from the Miocene to recent times.

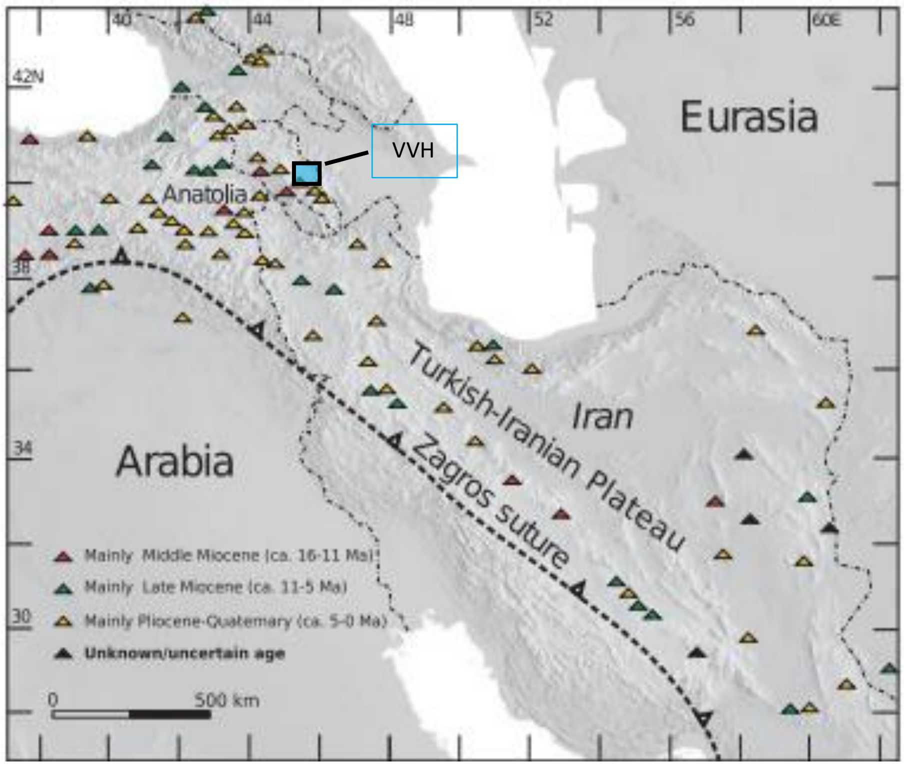

Figure 1.1: Volcanism in Arabia-Eurasia collision zone**.** Map showing Middle Miocene to recent volcanic centres across the Arabia-Eurasia collision zone. Marked in a light blue box is the area of study for this thesis, the Vardenis Volcanic Highland (VVH). Modified from Kaislaniemi et al. (2014).

Within this collision zone are the Lesser Caucasus Mountains (Figure 1.2). Located largely in the territory of Armenia, this mountain range is oriented approximately NW-SE and plays host to several volcanic highlands (Figure 1.2). These are Shirak & Lori (NW Armenia), Aragats and the surrounding volcanoes (W Armenia), Gegham (Central Armenia), Syunik (S Armenia) and Vardenis (E Armenia), the latter of which is the subject of this thesis. Adjacent to the Lesser Caucasus and the volcanoes of Armenia are two other volcanically and tectonically active regions: Eastern Anatolia to the west, and Northwest Iran to the southeast. The shared tectono-volcanic setting of these regions, paired with the large spatial and temporal variations in volcanism and seismicity that have been observed here (Allen et al., 2013 – Kurdistan Province of NW Iran. Keskin, 2007; Di Giuseppe et al., 2017 – Eastern Anatolia) has led to the AECZ becoming a point of interest for many geological disciplines.

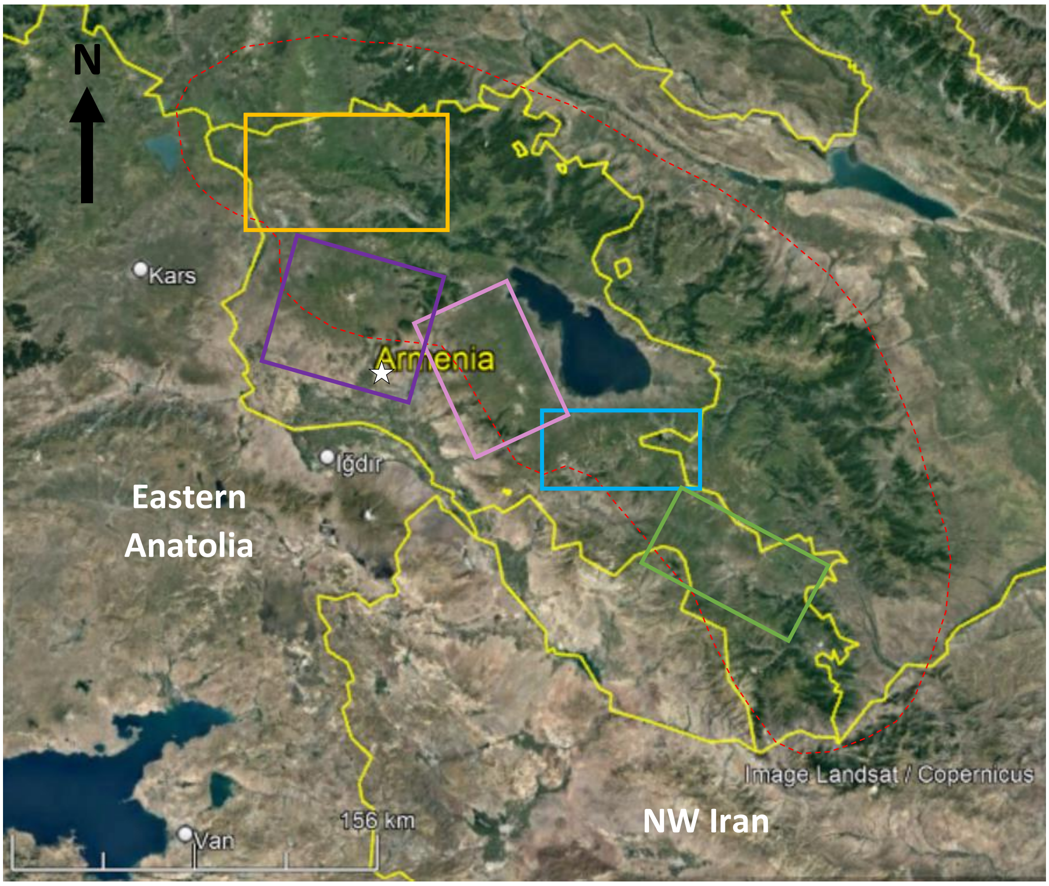

Figure 1.2: Satellite image with current international borders overlayed in yellow (from Google Earth, 2022). Approximate area of the Lesser Caucasus mountains, running from NW-SE across Armenia and the surrounding countries, outlined in a dashed red line. The study area (Vardenis Volcanic Highland - VVH) is highlighted by the light blue box. The other volcanic highlands of Armenia are also identified: Syunik (green box), Gegham (pink box), Shirak & Lori (gold box), and Aragats (and its surrounding volcanos) are in purple. The white star represents the Metzamor nuclear power plant (MNPP).

The Vardenis Volcanic Highland (VVH) is located in the SE of the Lesser Caucasus (Figure 1.2). It is closely related to the adjacent volcanic highlands of Gegham (to the NW) and Syunik (to the SE), from which it has been separated by largely arbitrary geographical boundaries. Prior to this study, the petrological and geochemical data for Vardenis was either of low quality and/or scarce, with most such data reported for the adjacent Syunik or Gegham volcanic highlands (e.g., Karapetian et al., 2001; Sugden et al., 2019; Lebedev, 2021). This project aims to report a new, high quality dataset and contribute to more comprehensive understanding of the VVH and the region as a whole.

Armenian volcanism (and wider tectonic activity) has been the subject of increasing investigation in recent years. The Shirak & Lori region in the north of Armenia, close to the Georgian border, has been mapped and sampled for petrochemical analysis (Neill et al., 2013; 2015). Armenia is very seismically active. In 1988, the Spitak earthquake hit NW Armenia, near the city of Gyumri. This *M*7 earthquake occurred on a NE dipping reverse slip fault plane, causing at least 25,000 deaths and leaving many more injured and without jobs or homes (Balassanian et al., 1995; Wyss & Martirosyan, 1998). In 2007, it was proposed that a new unit be built at the Metzamor nuclear power plant (MNPP) in the west of the country (Figure 1.2). As the MNPP is located within the volcano-tectonically active region surrounding the large Quaternary Aragats stratovolcano, a considerable amount of research was embarked on to conduct a state of the art volcano-tectonic risk assessment (Karakhanian et al., 2003; Connor et al., 2011; Aspinall et al., 2016). It was concluded that the benefits outweighed the risks, and the new reactor was approved in 2014. Understanding the volcano-tectonic hazards of Armenia is imperative to protecting the Armenian population, many of whom live near to recently active volcanoes and faults.

Research Questions

- What is the mineralogy, petrology and chemical make-up of post-collisional VVH and what is this telling us for the source of volcanism?
- What are the $^{87}Sr/^{86}Sr$, $^{143}Nd/^{144}Nd$ and $\delta^{11}B$ signatures of post-collisional Vardenis volcanic magmatism and what do they reveal about the pre-conditioning of the mantle source and possible crustal storage of magmas at VVH?
- How do the new results relate to the published Gegham, Syunik and very limited VVH datasets (Sugden et al., 2019, 2020), as well as the adjacent regions of Iran-Anatolian Plateau?

2. Literature Review

2.1 Geological Setting

The Lesser Caucasus mountains are in Western Asia, comprised of territory in modern Armenia, Georgia, and Azerbaijan. The region is located to the NE of the Bitlis-Zagros (B-Z) suture, which marks the collision of the Arabian and Eurasian continental plates, as well as the closure of the Neotethys ocean (Yılmaz et al., 1998; Seyitoğlu et al., 2019). During the final subduction phase (and subsequent collision), the slab of Neotethyan oceanic crust dipped to the north, inducing ample magmatism in Anatolia, Iran, and the Lesser Caucasus (Şengör & Yılmaz, 1981; Rolland et al., 2012). The closure of the Neotethys was a complex collisional event. Multiple microplates became accreted to the larger continental masses, as were ophiolites (Rolland et al., 2020) and antecedent marine sediments (Figure 2.1). This multifaceted collision has resulted in a complex basement geology across the AECZ (Rolland, 2017).

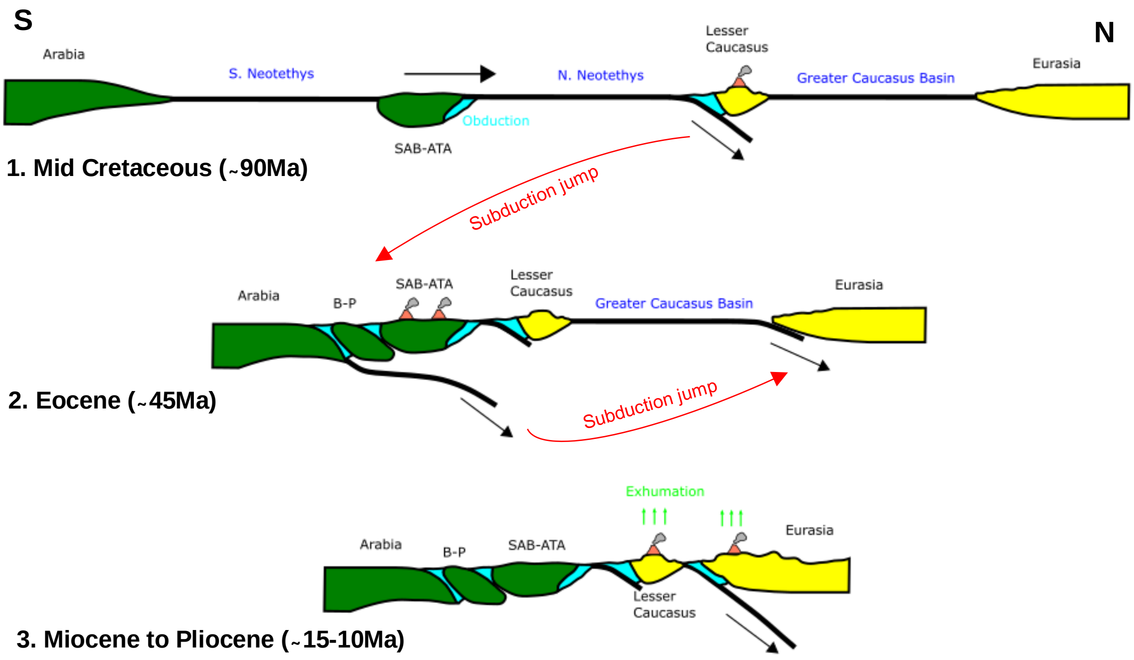

Figure 2.1.1: The collision of the Arabian and Eurasian plates/ the closure of the Neotethys ocean. Adapted from Rolland (2017). **(1)** Initial subduction beneath the Lesser Caucasus as the North Neotethys ocean began to close. This was a period of (pre-collisional) volcanism in the Lesser Caucasus. Also showing the beginning of the obduction of ophiolitic planes to the continental terranes. **(2)** Post-collision of several Arabian terranes (which are experiencing volcanism) and the Lesser Caucasus. Also shown is the initiation of subduction under Eurasia, and the final closure of the Greater Caucasus Basin (GCB) to the north of the Lesser Caucasus. **(3)** The re-initiation of volcanism in the Lesser Caucasus occurs (alongside high exhumation rates) in the Miocene following the closure of the GCB, with the final 'hard' collision coming in the Pliocene. Acronyms: B-P = Bitlis – Pütürge; SAB-ATA = Taurides-Anatolides-South Armenian Block.

The AECZ is a very volcanically active area. Geographically, the Lesser Caucasus is the central region of this volcanic zone, and it is flanked by E Anatolia to the west, and NW Iran to the southeast (Figure 1.1). AECZ volcanism can be divided into post- and pre-collisional types. Prior to the Miocene completion of Arabia-Eurasia collision, convergent margin volcanism and eruption of arc magmas was widespread (Figure 2.1.1 (1)). Pre-collisional volcanic material outcrop across the modern AECZ in areas that have not since been covered by post-collisional volcanics (Mederer et al., 2013; Kharazyan, 2005). There is evidence of two distinct phases of pre-collisional volcanism (first Late Cretaceous-Early Palaeocene, the second Early to Middle Eocene) (Schleiffarth et al., 2018) before the 'hard' collision of the Miocene-Pliocene (Figure 2.1 (3)). After the collision, the tectonic setting of the region had changed; from a subduction (with classical, deep-sea, sedimentary trench-volcanic arc front) setting to a continental collision zone with elevated plateaus, mountain ranges and folding. The post-collisional volcanism in this region is unique as it is happening above actively deforming and colliding tectonic plates. Post-collisional outcrops are abundant across the AECZ, with many relatively fresh exposures being found in the semi-arid, high altitude environment. Samples from such outcrops in the Southern Lesser Caucasus are the focus of this contribution.

The Armenian Lesser Caucasus hosts several major post-collisional volcanic highlands (Figure 1.2). In the southeast of the range is the VVH, flanked by Gegham to the NW and Syunik to the SE. It is an ~180km^2 area comprised of ~110 volcanoes. Monogenetic cones (vents that only experience one eruptive phase (Smith & Németh, 2017)) are the most abundant features in the VVH, found both discretely and on the flanks of the larger and older polygenetic volcanoes; Porak, Sandukansaar, Smbatasar (Figure 3.1.1) and Vayotssar. Cenozoic volcanic material dominates the arid, outcrop-rich landscape, with archaeological evidence of flows as young as 3000 years old at Porak (Figure 3.1.1) (Karakhanian et al., 2002). See Figure 3.1.2 for the most recent geological map of the VVH.

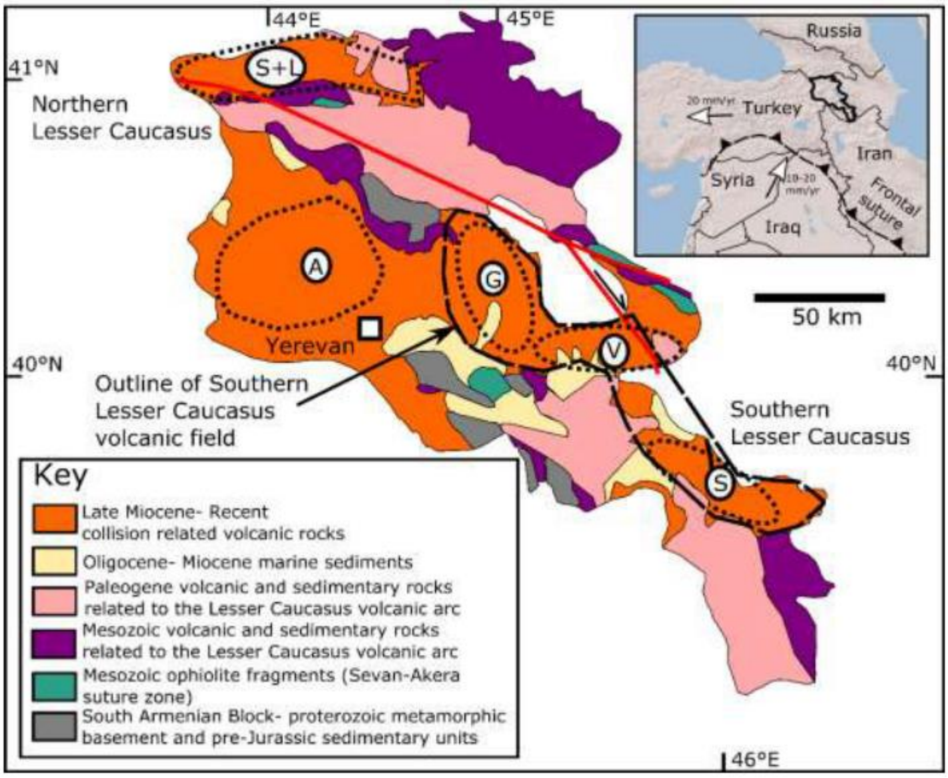

Figure 2.1.2: Geological map of Armenia from Sugden (2021) (and references therein), highlighting the post-collisional volcanic highlands

As detailed in Sugden (unpublished), the inset shows Armenia (outlined in bold) in relation to the wider AECZ, as well as showing the Bitlis-Zagros suture and local plate velocities. Volcanic Highlands: S+L = Shirak & Lori; A = Aragats and its surrounding volcanoes; G = Gegham; V = Vardenis; S = Syunik.

The distinction between the Gegham, Vardenis and Syunik highlands is largely arbitrary (based on geographically/geomorphology defining features) and they are often considered together as a single, extensive system when investigating the origins of magmatism in the area (Sugden et al, 2019). The other major volcanic highlands of the Armenian Lesser Caucasus are the large

Aragats stratovolcano and Arailer polygenetic centre in the west of the country (Connor et al., 2011) and the Shirak & Lori highland in the north (Neill et al, 2015) (Figure 2.1.2). The Lesser Caucasus is often considered as a whole system, and thus the highlands are compared and researched together. In Sugden (2019), a holistic model for volcanism across the Lesser Caucasus was generated. This work proposes that in the NW Lesser Caucasus melting occurs via delamination at the base of the thin lithosphere, whilst in the SE (in NW Iran), melting occurs in the middle of the much thicker lithosphere (Figure 2.1.3). As the Southern Lesser Caucasus (SLC) lies at an intermediate point between these two extremes of lithospheric thickness, it is thought that Gegham, Vardenis and Syunik are fed by a mixture of both mantle sources, creating a gradient of geochemical change across the region (Sugden et al., 2019). This contribution aims to determine whether an increased Vardenis dataset fits this hypothesis at a mid-way point between its more extensively researched neighbours, Gegham and Syunik.

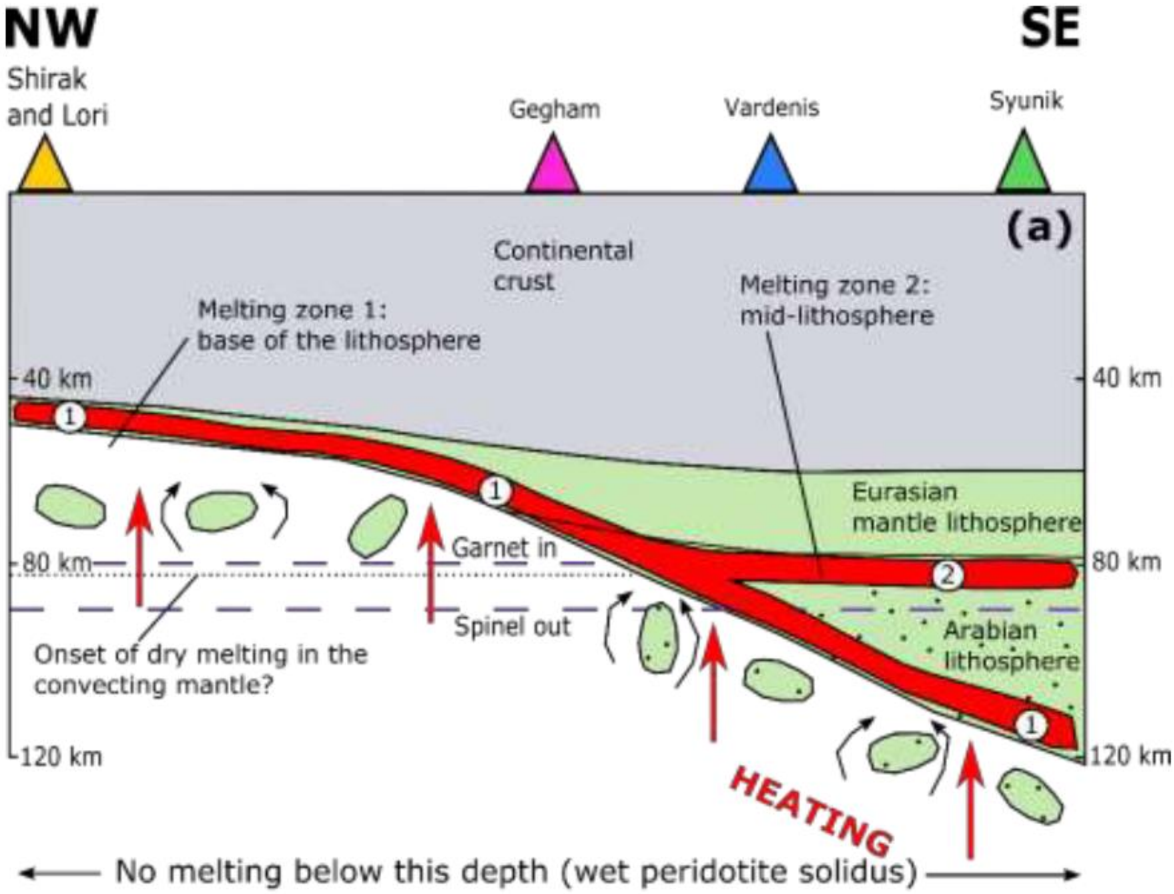

Figure 2.1.3: Model of magmatism for the Lesser Caucasus from Sugden et al. (2019).

Model shows the increasing lithospheric thickness from NW to SE (lithosphere shown in light green). Two mantle melting zones were identified feeding the SLC (labelled 1 & 2) that interact to fuel volcanism in this region. Also labelled are further mechanisms, explained in detail in Sugden et al. (2019)

2.2 Petrogenesis

The post-collisional volcanic rocks of the Lesser Caucasus cross a compositional spectrum from basanites to rhyolites (Figure 2.2.1). They also vary widely in texture, from mafic scorias to lavas (Sugden et al., 2019). The compositional range of post-collisional volcanic rocks in the VVH lies between trachybasaltic andesites to rhyolites. Via thin section petrographic observations, plagioclase feldspar was determined to be a ubiquitous phenocryst phase throughout the VVH. The more mafic samples also commonly contain clinopyroxene and olivine, whilst biotite, quartz and orthoclase feldspar were found only in rare felsic lithologies. Phenocrystic and glomerocrystic textures were common. Plagioclase, Fe-Ti oxides and clinopyroxene were the most common groundmass minerals, with groundmass textures varying between pilotaxitic, seriate and sub-ophitic. According to Sugden et al. (2019), the order of crystallisation in the VVH is olivine + Fe-Ti oxides ± apatite → clinopyroxene + Fe-Ti oxides ± olivine ± amphibole → clinopyroxene + plagioclase + Fe-Ti oxides ± amphibole ± phlogopite → plagioclase + potassium[K] feldspar + Fe-Ti oxides ± phlogopite.

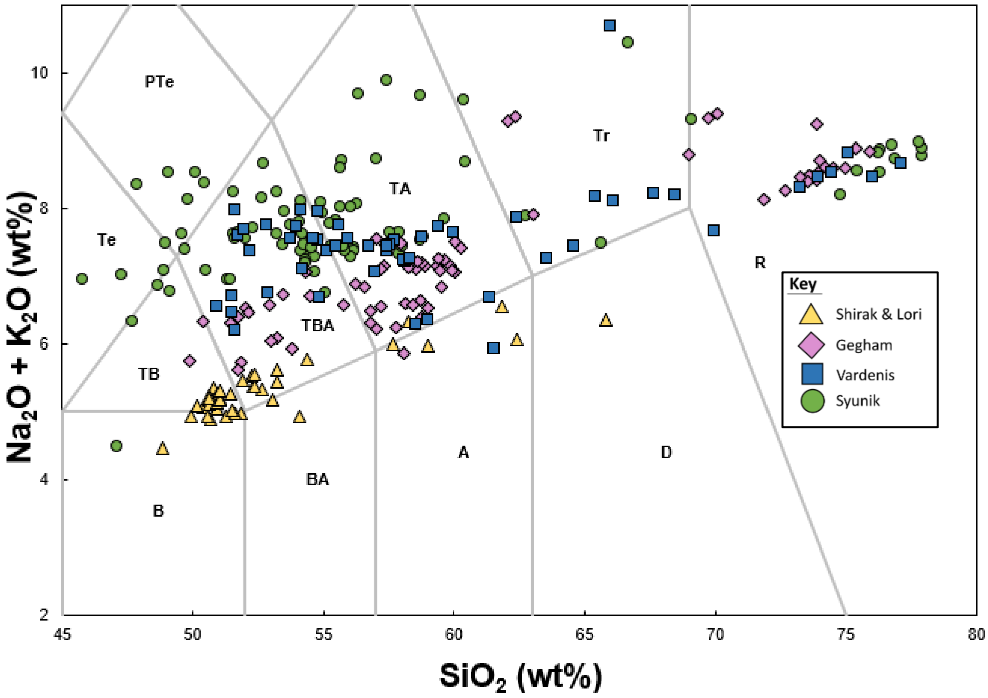

Figure 2.2.1: TAS (total alkalis vs silica) diagram showing data from across the Armenian Lesser Caucasus. Data from the VVH shows a compositional range from trachybasaltic andesite to rhyolite.

Data for Syunik & Vardenis from Sugden et al. (2019); Gegham from Savov (unpublished); Shirak & Lori from Neill et al. (2015).

The post-collisional rocks of the Southern Lesser Caucasus display a wide range of K_2O. The samples from Vardenis plot across the high-K calc-alkaline and alkaline/shoshonitic series (Figure 2.2.2). Across the Lesser Caucasus, MgO and P_2O_5 display curved patterns when plotted against SiO_2 (Figure 2.2.3), which suggests magma differentiation as the source of the more evolved lithologies (as opposed to crustal contamination) (Keskin et al., 1998). Furthermore, P_2O_5 becomes generally more enriched in the volcanic material when moving from NW-SE, suggesting a potential increase in apatite in the source (Sugden et al., 2019).

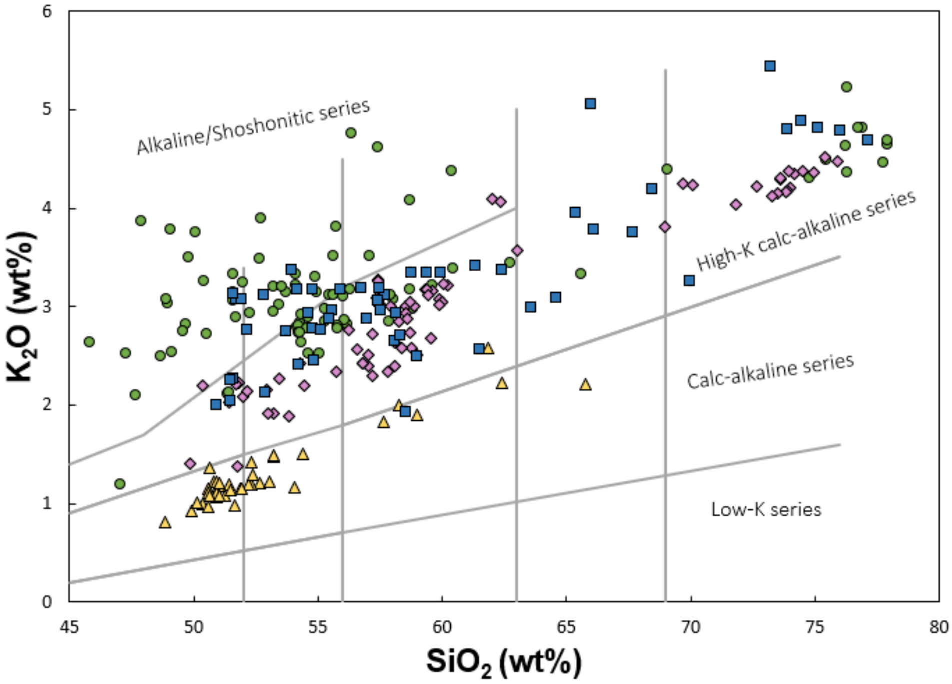

Figure 2.2.2: K_2O vs SiO_2 for the Armenian Lesser Caucasus. VVH dataset is mostly in the high-K calc-alkaline series.

Data sources are the same as in Fig. 2.2.1.

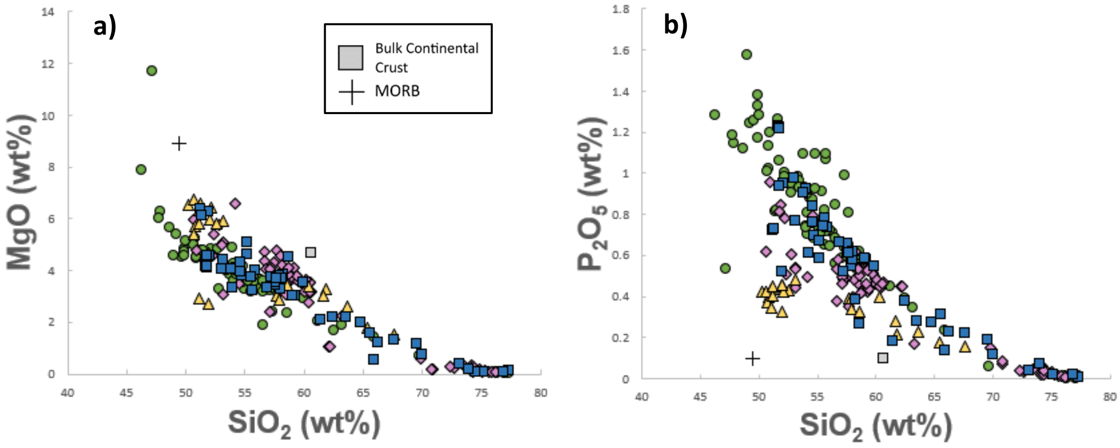

Figure 2.2.3: a) MgO vs SiO_2 – the gently curved trend of MgO with increasing SiO_2 indicates that gradual magmatic differentiation is what produced the more evolved volcanic material in the Southern Lesser Caucasus, as opposed to crustal contamination (Keskin et al., 1998). **b)** P_2O_5 vs SiO_2 – the same curved trend as in MgO vs SiO_2 is clearly visible. There is also a clear increase in P_2O_5 from NW (Shirak & Lori) to SE (Syunik) that Sugden et al. (2019) attribute to an increased amount of apatite in the melt source.

Data sources are the same as Fig. 2.2.1. MORB from Sun & McDonough (1989).

The trace element signature (MORB-normalised) of these rocks indicates a subduction component in the source (Figure 2.2.4) (Pearce et al., 2006). These indicators include enrichments in some of the large ion lithophile elements (LILE) (Ba, K and Sr) and ‘depletions’ in Nb, Ta and Ti (high field strength elements (HFSE)) relative to the other trace elements. This signature is omnipresent in the Lesser Caucasus post-collisional sequence, meaning that this subduction component is a part of the source of all Armenian volcanism. There are trace element variations across the Lesser Caucasus that may indicate a variation in the amount of the slab component in the mantle source (Sugden et al., 2019).

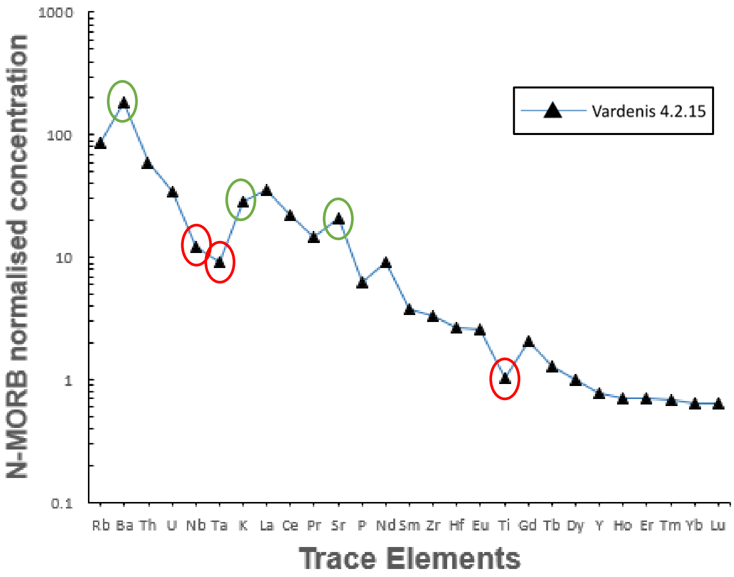

Figure 2.2.4: N-MORB normalised trace element plot for sample 4.2.15, one of the most mafic (highest MgO wt%) samples in the Sugden et al. (2019) Vardenis suite. Circled are the enrichments and depletions indicative of a subduction signature in arc rocks (Pearce et al., 2006).

2.3 Isotope Geochemistry

Isotopic ratios are an invaluable tool for understanding and identifying a plethora of geological mechanisms and phenomena. Sr and Nd isotopes are commonly used in igneous petrology to explore the origins of mantle sources, whilst B is a more novel and less commonly explored isotope in this field.

Use of Sr and Nd

Radiogenic isotope ratios (such as ^{87}Sr/^{86}Sr & ^{143}Nd/^{144}Nd) are used to identify the characteristics of the melt source and to reveal insights into the melting mechanics of a magma. These ratios compare the proportion of a stable isotope with its radiogenic counterpart. The radiogenic component forms from the decay of a different element (for ^{87}Sr this is Rb), which typically behaves differently to the measured element during either melting, fractionation, or another composition-altering mechanism. However, when it comes to determining mantle sources, the ratios looked at are the original ratios before melting or crystallisation. Thus, only isotope systems unaffected by these processes can be used. Sr and Nd ratios (^{87}Sr/^{86}Sr & ^{143}Nd/^{144}Nd respectively) are two such systems and are used extensively as mantle tracers (Cohen and

O'Nions, 1982; White, 1995). Mantle is considered to be 'enriched' when it has high $^{87}Sr/^{86}Sr$ and low εNd (Figure 2.3.1).

$$\varepsilon Nd = \left[\frac{\left(\frac{^{143}Nd}{^{144}Nd}\right)_{sample}}{\left(\frac{^{143}Nd}{^{144}Nd}\right)_{BSE}} - 1 \right] \times 10^4$$

Figure 2.3.1: The calculation used to calculate εNd. Bulk Standard Earth (BSE) values was the 'Chondrite Uniform Reservoir' value from Jacobsen and Wasserburg (1980).

In their investigation of the Southern Lesser Caucasus, Sugden et al. (2019) used $^{87}Sr/^{86}Sr$ & $^{143}Nd/^{144}Nd$ ratios to determine that there was no crustal contamination of the magma source, utilising a database of samples from Vardenis and Syunik. The data showed very little isotope ratio variability with SiO_2 (Figure 2.3.2). As the Armenian basement rocks are not exclusively arc volcanics (metamorphic rocks and Mesozoic-Cenozoic sediments (Mederer et al., 2013)), crustal contamination would have caused a distinct difference between the mafic and felsic Sr and Nd values in the post-collisional rocks.

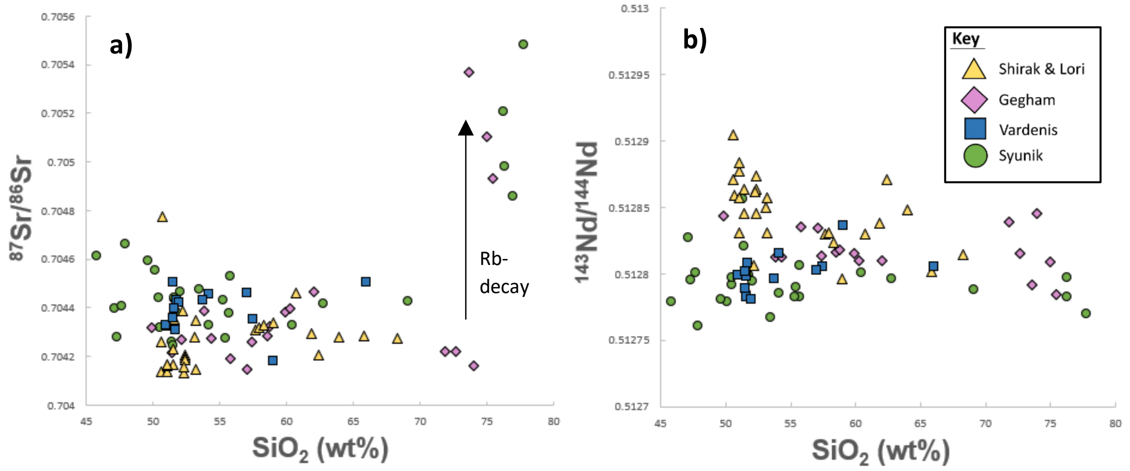

Figure 2.3.2: Sr and Nd isotopic ratios vs SiO_2. **a)** Most samples show no variation in $^{87}Sr/^{86}Sr$ with increasing SiO_2. There is a slight increase in the most felsic samples, but this was attributed to Rb-decay post-crystallisation (Sugden et al., 2019). **b)** No variation in $^{143}Nd/^{144}Nd$ with increasing SiO_2, indicating that there was likely no crustal contamination.

Data sources are the same as in Fig. 2.2.1.

The Sr/Nd isotope systematics plot the Lesser Caucasus array between the MORB and Bulk Earth compositional endmembers (Figure 2.3.3). There is also a trend of increasing Sr ratios and decreasing Nd from NW to SE (from Shirak & Lori to Syunik), indicating a source enrichment along this transect (Sugden et al., 2019) (Figure 2.3.3).

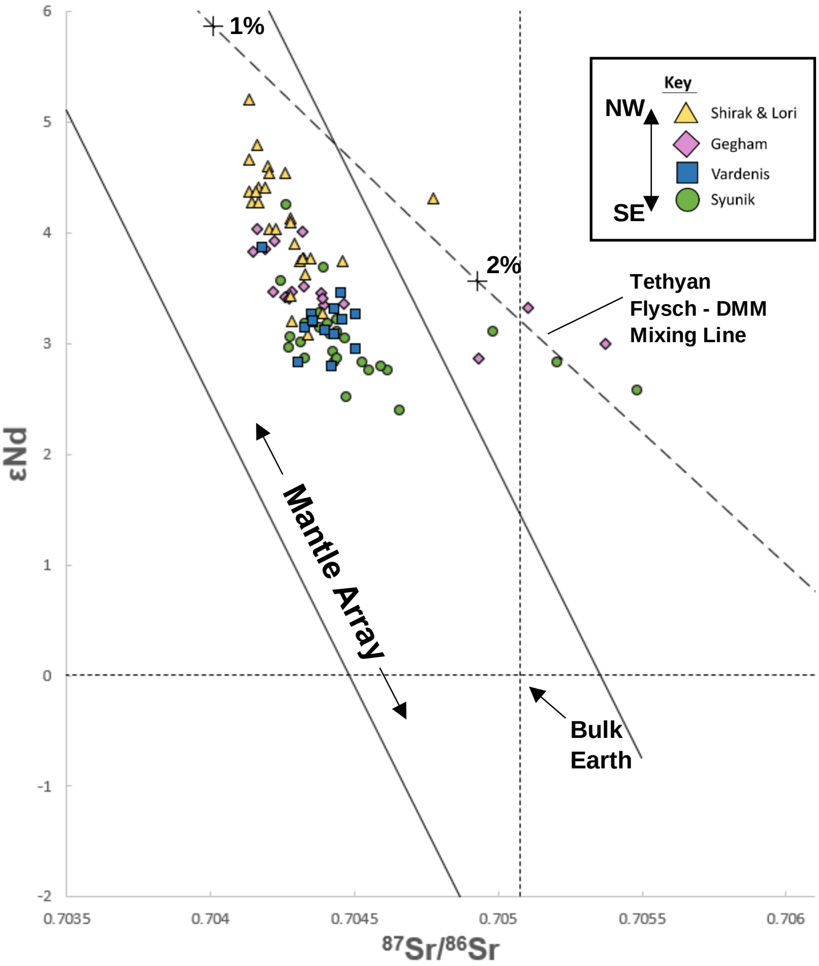

Figure 2.3.3: Sr-Nd isotope systematics of the Armenian Lesser Caucasus. Clear trend of increasing mantle source enrichment from Shirak & Lori in the NW to Syunik in the SE. Vardenis fits this trend, being slightly less enriched than Syunik but generally more enriched than Gegham.

Data sources are the same as in Fig. 2.2.1. Mantle Array and Bulk Earth values from Rollinson (1993). The mixing line is between depleted MORB mantle (DMM) (White and Hofmann, 1982) and Tethyan Flysch (Prelević et al., 2008). Graph is adapted from Sugden et al. (2019).

Use of B

Boron (B) is a fluid mobile trace element commonly used as a tracer for recycled material in the mantle source (Ishikawa and Tera, 1999). During subduction, a substantial amount of hydrated, seawater-altered material is entrained and pulled down into the mantle. As the subducted slab migrates deeper into the mantle, the increasing temperature and pressure begins to dehydrate the recycled sediments, releasing the fluid component into the mantle wedge (and continental slab) above. This results in an enrichment of fluid-mobile elements (such as B) in the mantle wedge and a depletion of them in the dehydrated slab (Ishikawa and Nakamura, 1994; Tonarini et al., 2005). Furthermore, for B, this process causes an isotopic fractionation. The two major stable isotopes of B are ^{10}B and ^{11}B. Comparatively, ^{11}B preferentially fractionates into the trigonal molecular sites of aqueous fluids, whilst ^{10}B prefers the tetrahedral sites of silicate melts and minerals (Kakihana et al., 1977). As a result of this, dehydrated sediment has isotopically light B, as a much larger fraction of the heavy ^{11}B was lost to the fluid than of ^{10}B. This isotopic fractionation is recorded as $\delta^{11}B$, a measurement which compares the recorded B isotope ratio to that of the NIST 951 standard (Figure 2.3.4).

$$\delta^{11}B = \left(\left[\frac{\frac{^{11}B}{^{10}B}_{sample}}{\frac{^{11}B}{^{10}B}_{NIST951}}\right] - 1\right) \times 1000$$

Figure 2.3.4: $\delta^{11}B$ calculation from Ni et al. (2010).

Primitive upper mantle, most commonly sampled at ocean ridges as MORBs, is depleted in B (0.19ppm) and has a $\delta^{11}B$ of -7.1 ± 0.9‰ (Marschall et al., 2017). In contrast, seawater and seawater-altered materials (such as oceanic sediments, crust, and serpentinites) are enriched in B and often have comparatively heavy $\delta^{11}B$ ratios (+2 to +26‰ for marine sediments and +7 to +20‰ for oceanic serpentinites) (De Hoog & Savov, 2018). This means that, during subduction dehydration, the overlying mantle wedge (and subsequently the continental crust) becomes significantly enriched in high [B], heavy $\delta^{11}B$ fluids from the subducted slab. These fluids can be transitory (not imparting their slab signature to the mantle wedge) but on some occasions the B-enriched signature is preserved in the lithospheric mantle in repository minerals, such as metasomatic amphibole and phlogopites (Mandler & Grove, 2016). Meanwhile, the dehydrated slab now has a low [B] signature with $\delta^{11}B$ significantly lighter than the primitive mantle (e.g. La Palma averages -10.5 ± 0.7‰) (Walowski et al., 2019). This is then preserved in the intermediate/deep mantle, which is resultantly never replenished in elemental B, and has an extremely light $\delta^{11}B$.

A major reason why B is a good tracer for these sediments is that its distinctive isotopic signature is well preserved in the intermediate/deep mantle. Furthermore, [B] and $\delta^{11}B$ are minimally affected during the return to the surface and melting. However, B can be altered by assimilation of crust, which would likely increase [B] and lighten $\delta^{11}B$, as the crust is enriched in B and has a typically light $\delta^{11}B$ (-9.1 ± 2.4‰) (Marschall et al., 2017). To safeguard against this bias, analysis of B for global databases utilises volcanic glasses and olivine melt inclusions, as these are the most pristine record of a melt source (Walowski et al., 2019; Walowski et al., 2021).

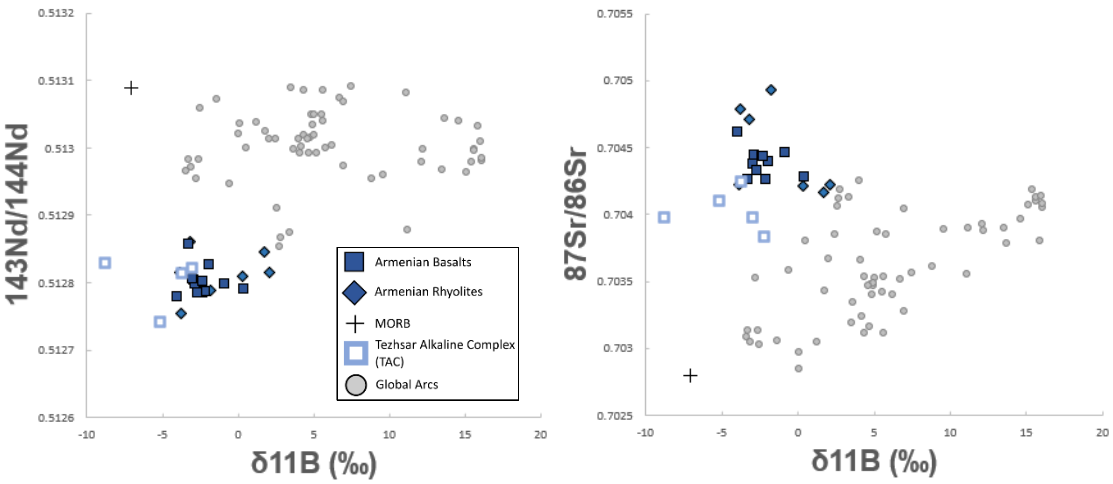

Figures 2.3.5: Sr and Nd isotope ratios against $\delta^{11}B$ for post-collisional Armenian volcanics. Graphs highlighting that post-collisional volcanics have a heavier $\delta^{11}B$ than the MORB average, as well as their deviation from the $\delta^{11}B$ of other arc volcanics from across the world. The Armenian data shows a $\delta^{11}B$ range of -5.81 to +2.1‰, whilst the MORB figure is -7.1‰ (Marschall et al., 2017).

Global Arcs from De Hoog and Savov (2018); MORB from Marschall et al. (2017) and White and Hofmann (1982); TAC data from Sokół et al. (2018); and post-collisional basalt and rhyolite data from Sugden et al. (2020), after which the graphs are also adapted.

Sugden et al. (2020) have completed limited B analysis on post-collisional basalts and rhyolites from across Armenia. All the samples have relatively light $\delta^{11}B$ (-5 to +2‰) and low [B] content but are shown to have heavier $\delta^{11}B$ than the primitive mantle (Figure 2.3.5). It is thus clear that Armenian volcanism is not derived from the melting of dehydrated slab material. It is instead thought that the slab signature in Armenia resulted from the formation of a sediment melt that entered the lithospheric mantle and was preserved there in metasomatic amphiboles whilst the mantle was subsequently dehydrated. The signature was later imparted to future melts.

3. Methods

3.1 Sampling

The VVH rocks used in this study were collected over several summer-autumn field campaigns in the period of 2008- 2019 by the main supervisor (I. Savov) and co-workers from Armenia, as well as abroad (USA, Germany, Italy, UK). In 2019 alone, 26 of the freshest and most representative samples were collected across the VVH from 16 different mapped Quaternary to Holocene volcanoes (Figure 3.1.2).

Samples were selected based on appearance of freshness (dark colour, no clear secondary mineralogy and alteration). Sampling was hindered by the often mountainous landscape, as some outcrops are inaccessible.

Samples from many lava flows, quarries and road cuts were collected. The majority are from monogenetic cones, but also some were collected from the slopes of the large, polygenetic volcanoes of the region (e.g., Smbatasar (Figure 3.1.1a) or Porak (Figure 3.1.1b)). The latter is the site of Vardenis' most recent volcanic activity (~3000 years ago; Karakhanian et al., 2002).

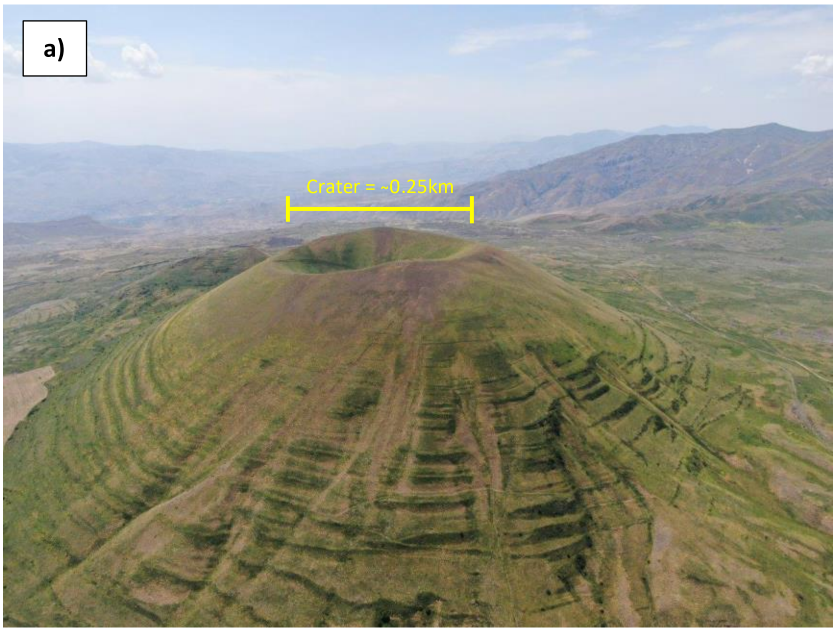

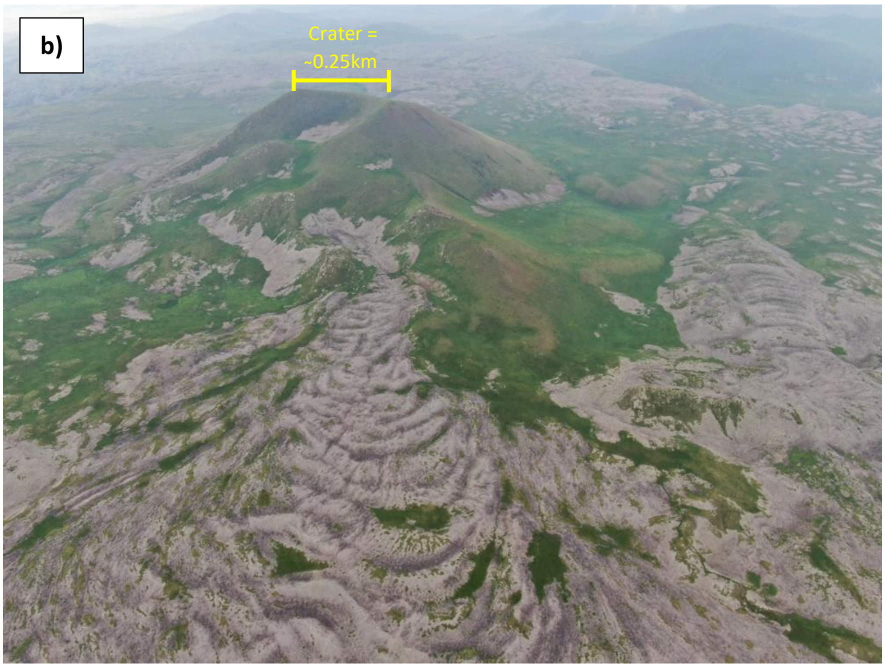

Figure 3.1.1: a) Drone photo of Smbatasar volcano that last erupted basalt-andesites in historical times (Karakhanian et al., 2002). This volcano is situated in the middle of the VVH. Photo credit – Dr. Khachik Meliksetian (Armenian Academy of Sciences). **b)** Drone photo of Porak volcano, situated in the NE of the VVH. This is the site of the last Holocene volcanism in Vardenis. Photo credit – Dr. Khachik Meliksetian. Scales approximated from Google Earth.

The new dataset, in combination with aerial and satellite images, has been used to construct a geological map for the VVH (Figure 3.1.2). The current number of samples from the VVH is 109 and details of these rocks are listed in Table 3.1.3.

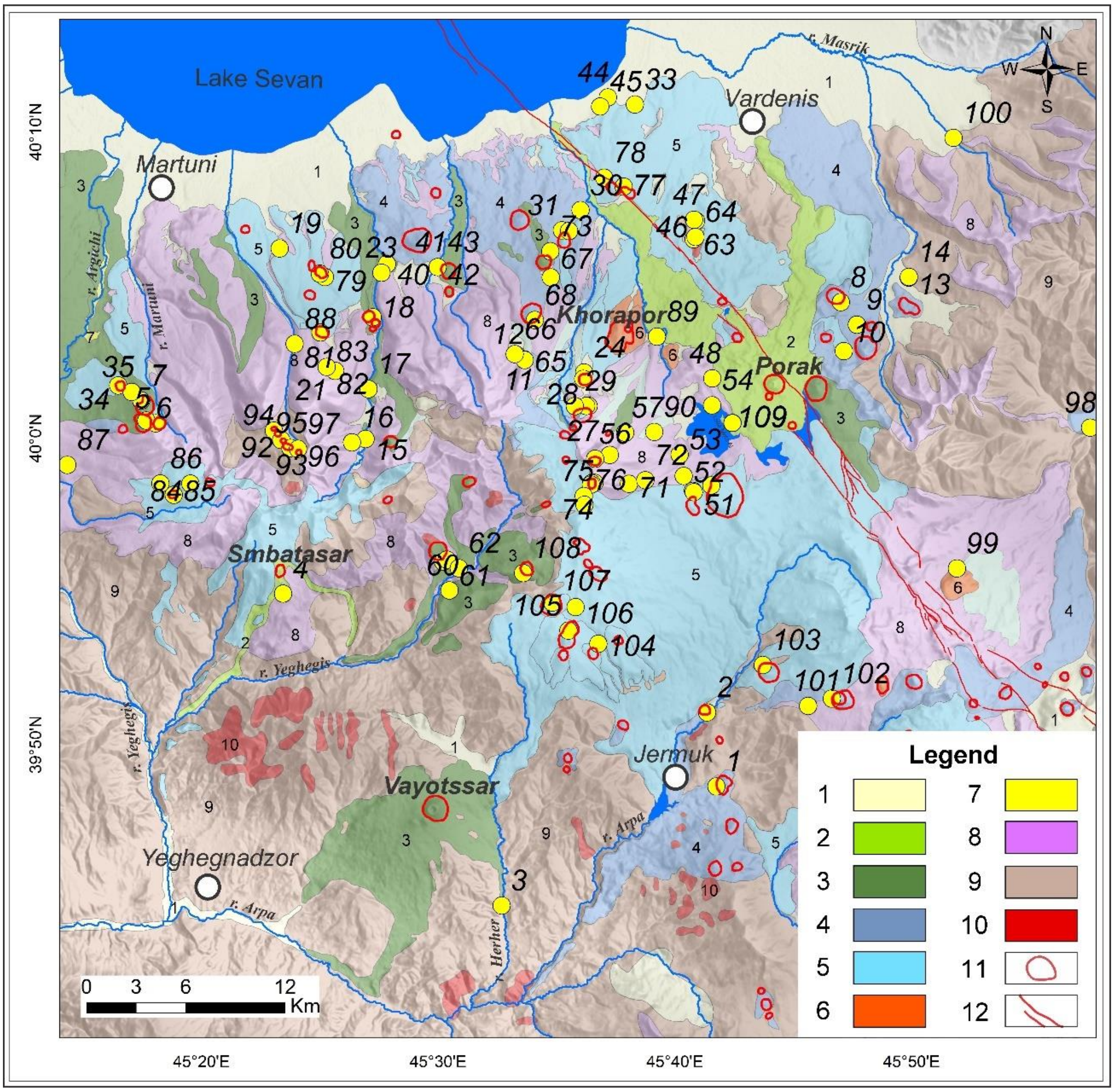

Figure 3.1.2: Geological map of the VVH with sample locations shown. See Table 3.1.3 for details on sample IDs and Figure 3.1.4 for stratigraphic and lithological details for the units 1-12. (11) in the legend are cinder cones, and (12) are active faults. Map compiled by S. Karapetyan, K. Meliksetian, G. Navasardyan and I. Savov.

Table 3.1.3: All samples from Vardenis (shown on 3.1.2), compiled by the same authors as Fig. 3.1.2. Those highlighted in blue are included in the new petrological and geochemical dataset analysed in this work.

Sample # on the map	Sample ID	Volcano name/Place of sample	Sample type	Composition
1	6-2-13	Hamazaspablur	Lava	Basaltic trachyandesite
2	6-1-13	Vardenis mountain	Lava	Basaltic trachyandesite
3	5-2-13	Vardenis mountain	Lava	Trachyandesite
4	5-1-13	Vardenis mountain	Lava	Basaltic trachyandesite
5	4-3-13	Putputaqar	Lava	
6	4-2-13	Sevkar	Scoria	Trachyandesite
7	4-1-13	Sevkar	Scoria	Trachyandesite
8	3-3-13	Aregon	Lava	Basaltic trachyandesite
9	3-2-13	Spandaramet	Lava	Basaltic trachyandesite
10	3-1-13	Spandaramet	Lava	Andesite
11	2-2-13	Vardenis mountain		
12	2-1-13	Vardenis mountain		
13	1-1-13	Amanor	Lava	Basaltic trachyandesite
14	1-2-13	Amanor	Lava	Basaltic trachyandesite
15	1-1-12	Near the village Zolaqar	Lava	Rhyolite
16	1-2-12	Amanor	Lava	
17	1-3-12	Arpa-Sevan3	Lava	Trachyandesite
18	1-4-12	Arpa-Sevan1	Bomb	
19	2-1-12	Near the village Zolaqar	Lava	Basaltic trachyandesite
20	2-2-12A	Mredivar	Lava	Trachyandesite
21	2-2-12B	Mredivar	Lava	Trachydacite
22	2-3-12	Arpa-Sevan1	Lava	Trachyandesite
23	2-4-12	Near the road up to Arpa-Sevan1	Lava	Trachyandesite
24	3-1-12	Spandaramet	Lava	Trachyandesite
25	3-2-12	Spandaramet	Lava	
26	3-3-12A	Sandukhqasar	Lava	
27	3-3-12B	Sandukhqasar	Lava	Trachydacite
28	3-3-12C	Sandukhqasar	Lava	
29	3-3-12D	Sandukhqasar	Lava	Trachydacite
30	3-4-12	Mzkitaver	Lava	Trachyandesite
31	3-5-12	Mkhitaver	Lava	Basaltic trachyandesite
32	3-6-12	Near the village Mkhitaver	Lava	
33	4-1-12	Near the village Tsovak	Lava	Rhyolite
34	4-2-12	Yanikh	Lava	
35	4-3-12	Sevqar	Lava	
36	6-27-08	Khrbekner	Lava	Basaltic trachyandesite
37	7-28B-08	Khorapor	Lava	Rhyolite
38	7-29-08	Khonarasar	Lava	Basaltic trachyandesite
39	7-30-08	Sankar	Bomb	Basaltic trachyandesite
40	7-31-08	Sankar	Lava	Trachydacite
41	7-32-08	Sankar	Lava	Basaltic trachyandesite
42	8-33-08	Srpidar	Lava	Trachyandesite
43	8-34-08	Karmravor	Lava	Basaltic trachyandesite
44	4-1-15	West of Tsovak village	Pumice	Rhyolite
45	4-2-15	West of Tsovak village	Lava	Basaltic trachyandesite
46	5-1-15	Subatan tuff, quarry, Geghakar village	Ignimbrite	Trachyandesite
47	5-2-15	Flow, covers Subatan tuff in quarry	Lava	Trachyandesite
48	5-3-15	Porak	Lava	Trachyandesite
49	5-4-15	Zhiligyol	Lava	Trachyandesite
50	5-5-15	Rhyolite west of Zhiligyol volcano	Lava	Rhyolite

Table 3.1.3 continued.

Sample # on the map	Sample ID	Volcano name/Place of sample	Sample type	Composition
51	5-6-15	West of Zhiligyol volcano	Lava	Basaltic trachyandesite
52	5-7-15	West of Zhiligyol volcano	Lava	Trachydacite
53	5-8-15	West of Zhiligyol volcano	Lava	Rhyolite
54	5-9-15	Lake Al-Lich	Agglomerate	Trachydacite
55	6-2-15	Torgomayr	Lava	Trachydacite
56	6-3-15	Torgomayr	Lava	Basaltic trachyandesite
57	6-4-15	2 km NE of Torgomayr volcano	Lava	Basaltic trachyandesite
58	7-1-15	Trdatanist	Lava	Trachyandesite
59	7-2-15	Old dome east of Trdatanist volcano	Lava	Rhyolite
60	7-3-15	South slopes of Vardenis ridge	Lava	Trachyandesite
61	7-4-15	South slopes of Vardenis ridge	Lava	Trachyandesite
62	7-5-15	South slopes of Vardenis ridge	Lava	Basaltic trachyandesite
63	1-1-17	Valley south of Subatan quarry	Plutonic	Trachyandesite
64	1-2-17	Valley South of Subatan quarry	Lava	Trachyandesite
65	2-1-17	Valley SE of Vardenis Mountain	Lava	
66	2-2-17	Valley NW of Vardenis Mountain	Lava	
67	2-3-17	Triator	Lava	Trachyandesite
68	2-4-17	Triator	Lava	Trachydacite
69	3-1-17S	Narekanun	Scoria	Trachybasalt
70	3-1-17b	Narekanun	Lava	Basaltic trachyandesite
71	3-2-17	Narekanun	Lava	Amphibole trachydacite
72	3-3-17	Narekanun	Lava	Trachydacite
73	2-5-17	Yervandapal	Lava	Basaltic trachyandesite
74	3-5-17	Narekanun, N slope	Lava	Trachyandesite
75	3-6-17	New volcanic cone	Lava	Basaltic trachyandesite
76	3-7-17	Semasar, S slope	Lava	Basaltic trachyandesite
77	1-1-19	Khonarasar	Bomb	Basaltic trachyandesite
78	1-2-19	Khonarasar	Lava	Basaltic trachyandesite
79	2-1-19	Khrbakner	Lava	Basaltic trachyandesite
80	2-2-19	Khrbakner	Lava	Basanite-tephrite
81	2-3-19	Sardarivar	Lava	Trachybasalt
82	2-4-19	North part of Sardarivar volcano	Lava	
83	2-5-19	North part of Sardarivar volcano	Lava	Trachyandesite
84	3-1-19	NE of Avdoikar volcano	Lava	Trachydacite
85	3-2-19	Avdoikar	Lava	
86	3-4-19	NW of Avdoikar volcano	Lava	Trachydacite
87	3-5-19		Lava	Basaltic trachyandesite
88	4-1-19	S from village Zolaqar	Lava	Trachyandesite
89	4-2-19	Abandoned village	Block	
90	4-3-19	NE of Poqr Khlis	Dike	Trachyandesite
91	4-4-19	Pzuk	Lava	Trachyandesite
92	4-5-19	Poqr Khlis	Lava	Basaltic trachyandesite
93	4-6-19	Poqr Khlis	scoria	Basaltic trachyandesite
94	4-7-19	Poqr Khlis	scoria	Basaltic trachyandesite
95	4-8-19	Khlis	Lava	Basaltic trachyandesite
96	4-9-19	Karmirdosh	Lava	Trachyandesite

Table 3.1.3 continued.

Sample # on the map	Sample ID	Volcano name/Place of sample	Sample type	Composition
97	4-10-19	Karmirdosh	Lava	Trachyandesite
98	5-1-19	Road up to Tsar village (Karabakh)	Lava	
99	5-2-19	Chaghatsar (Qechaldagh)	Lava	Rhyolite
100	5-3-19	On the road back into Armenia, near the village Azat	Lava	
101	6-1-19	Karmitglukh	Lava	Basaltic trachyandesite
102	6-2-19	Karmitglukh	Scoria	Trachybasalt
103	6-3-19	Archisar	Lava	Basaltic trachyandesite
104	7-1-19	Ananaun	Lava	Basaltic trachyandesite
105	7-2-19	Muradsar	Lava	Basaltic trachyandesite
106	7-3-19	E of Kyazhsar	Lava	
107	7-4-19	Kyazhsar	Scoria	Basaltic trachyandesite
108	7-5-19	Getik	Lava	Basaltic trachyandesite
109	12-39-04	Porak	Lava	Basaltic trachyandesite

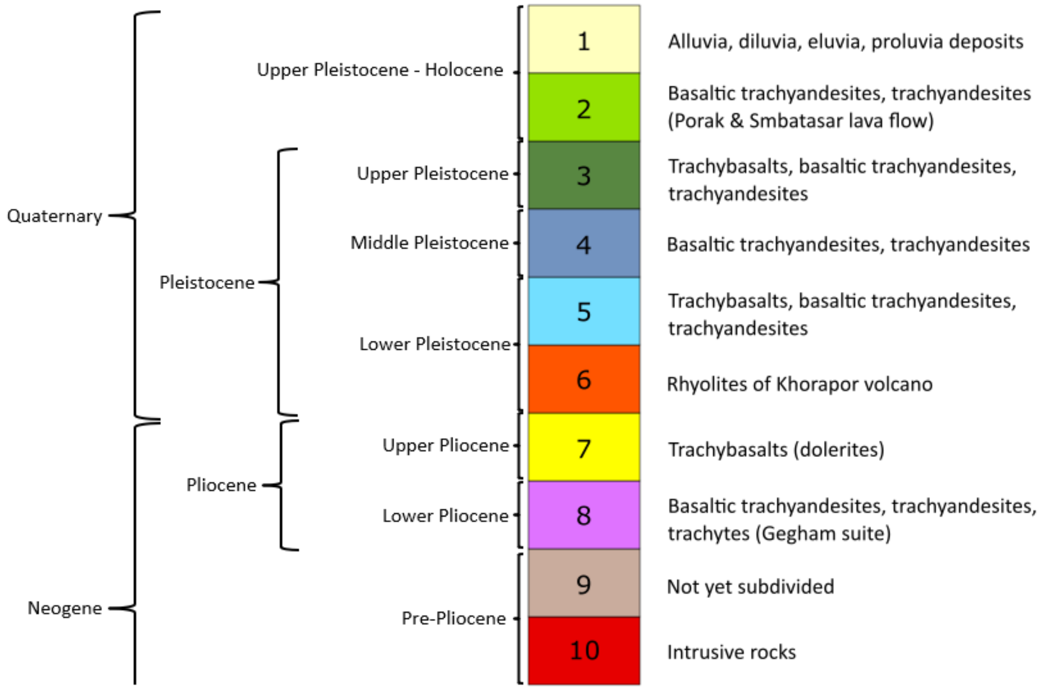

Figure 3.1.4: Stratigraphic column for the VVH. The numbers and colours correspond to the unit on the legend of Fig. 3.1.2. Information from the same authors as Fig. 3.1.2. Unit thickness is not to scale.

In May 2022, Ivan Savov and Thomas Ronayne (alongside our Armenian colleagues) completed 4 days of fieldwork across the Gegham Volcanic Highland (GVH). The collected GVH samples will be utilised in future research to further expand the petrological and geochemical studies of volcanism in the Lesser Caucasus. Some key outcrops of the VVH were revisited and inspected, for example the long Holocene lava flows of the Porak volcano or the VVH lava flows with unknown sources (vent) in the vicinity of lake Sevan shores and the town on Vardenis.

3.2 Boron Isotope Analysis

For B isotope analysis, a carefully selected representative suite was prepared, processed, and measured at the IGG Labs at CNR Pisa, Italy. Approximately 0.3g of sample powder was fused with a K_2CO_3 flux in a 40ml platinum crucible, with a flux to sample ratio of 4:1. The fusion cakes were then crushed and centrifuged with B-free (and high pH) water to extract the boron. The solution was then further purified using anion and cation exchange columns. The procedure comprised of a run through an anion column (packed with Amberlite® IRA-643 boron-specific anion exchange resin), followed by a cation-exchange column (packed with AG 50W-X8 resin) step, and then a repeat of the anion column step to produce the purified boron solution (procedure described in detail by Tonarini et al. (1997)). The boron isotope composition of the samples were measured on a Thermo Scientific^{TM} *Neptune* series multi-collector (MC)-ICP-MS, also at IGG-CNR Pisa, which was specifically tuned for $^{11}B/^{10}B$ analysis (following Foster, 2008). The samples were diluted to contain ~20ppb B. To correct for machine induced mass fractionation, they were bracketed with NBS 951 boric acid standard solution of the same concentration. The samples were then run through the (MC)-ICP-MS, measuring both the boron concentration and $\delta^{11}B$. This data was then converted into sample concentrations using the precise and accurate sample weights and reagent volumes.

The run errors within the measurements are between 0.02 and 0.54‰. The measurement accuracy was monitored as follows: 19 replicate analyses of NBS 951 giving an average $\delta^{11}B$ value of -0.71±0.42‰ (2σ). Once corrected for NBS 951, the one analysis of IAEA standard B5 (basalt) gave a $\delta^{11}B$ value of -5.15±0.14‰ (accepted value ~-6±0.6‰; Paul et al., 2023 - under review), the two replicate analyses of IAEA standard B6 (obsidian) gave an average $\delta^{11}B$ of -4.09±0.26‰ (accepted value ~-3.9±0.5‰; Paul et al., 2023 – under review) and the one analysis of NIST 612 gave a $\delta^{11}B$ value of -2.20±0.04‰ (accepted value ~-1.07‰; Kasemann et al., 2001).

3.3 Major and Trace Element Analysis

During sample preparation, ~50g of each sample was crushed in an agate mill. The samples underwent $HF-HNO_3$ digestions. At ALS labs in Vancouver, Canada, ICP-ES analysis was used to take major (and minor) element measurements, whilst ICP-MS was used to analyse the trace elements (see https://www.alsglobal.com/en/geochemistry/rock-characterisation/whole-rock-analysis for methodology).

Duplicate analyses of the major elements showed a reproducibility of within 4% (for oxides >1wt%), and of 10% or better for most trace elements. The accuracy was monitored using the following internal standards: AMIS0085, AMIS0167, AMIS0304, AMIS0547, BCS-512, CDN-W-4, OREAS 146, OREAS-101b, and SY-4. The relative standard deviation of the standards was better than 5% for all major oxides >1wt% (and within range to the literature values), whilst all trace element measurements were within the expected range.

3.4 Sr-Nd isotope analysis

For the analysis the $^{87}Sr/^{86}Sr$ and $^{143}Nd/^{144}Nd$ ratios, Thermal Ionisation Mass Spectrometry (TIMS) was used. To extract the Sr and Nd, each unspiked rock powder was dissolved in an HNO_3: HF mixture (1:4), subsequently dried and taken up in 12M HNO_3, dried again and taken up in 12M HCl, dried and finally taken up in 2M HNO_3. The solutions then underwent conventional ion-exchange chromatographic column techniques at the University of Leeds, comprising of two (repeated) Sr-spec resin elutions, a Tru-spec elution and an LN-spec elution. The Sr and Nd isotope ratios were measured on a Thermo Scientific^{TM} *Triton* multi-collector mass spectrometer running in static mode. Sr was measured on a 1-5V ^{88}Sr signal, whilst Nd was measured on a 0.3-0.8V ^{144}Nd signal. The normalisation value for mass spec fractionation of $^{87}Sr/^{86}Sr$ was $^{86}Sr/^{88}Sr = 0.1194$; and for $^{143}Nd/^{144}Nd$ the value was $^{146}Nd/^{144}Nd = 0.7219$. Instrument errors for the $^{87}Sr/^{86}Sr$ and $^{143}Nd/^{144}Nd$ measurements are reported as the standard error; (2σ – 2 standard deviations about the mean of the 200-240 measurements collected per sample for Nd and 120-140 measurements per sample for Sr). Replicate measurements of primary standards with each batch of samples were used to calculate external precision (2σ). All measured samples were then corrected to these primary standards. For Sr, the NIST SRM-987 International Reference Standard was used and showed a 2σ better than 30ppm across six runs ($^{87}Sr/^{86}Sr$ average = 0.710278, with a standard deviation of 8.8×10^{-6}). For Nd, the La Jolla Nd International Reference Standard was used and showed a 2σ of ~6ppm out of four different runs ($^{143}Nd/^{144}Nd$ average = 0.511829). USGS standards AGV-1, AGV-2, G-2, and BCR-2 were also run for both $^{87}Sr/^{86}Sr$ and $^{143}Nd/^{144}Nd$. The corrected BCR-2 samples and G-2 standards reproduced the respective $^{87}Sr/^{86}Sr$ literature values to within 2σ (0.705013 and 0.709770 respectively; Weis et al., 2006). BCR-2 also reproduces the $^{143}Nd/^{144}Nd$ literature value of 0.512637. The total chemistry blanks of Sr were negligible during measurement (~100ng).

3.5 Electron Microprobe Analysis (EMPA)

This method is adapted from the one detailed in Sugden (2021)

In-situ major element olivine, clinopyroxene, orthopyroxene and amphibole compositions were ascertained on a JEOL8230 electron microprobe at the University of Leeds. A focused beam, with a 20KeV acceleration voltage, was used for the analysis. During each analysis, the major elements underwent 30 seconds of analysis on peak and with a 30 nA beam current. The minor elements were run for 80 to 120 seconds on peak with a 100nA beam current.

The main standard used were the San Carlos olivine, the Smithsonian Kakanui hornblende and the GEO2 diopside (Jarosewich et al., 1980) (the spot analysis for each standard is provided in Appendix 3). San Carlos olivine spot analyses were on average within 0.5wt% of the expected oxide abundances, with any variations from the literature being corrected for before the data was examined (specifically on FeO, SiO_2, MgO, CaO and MnO). The GEO2 diopside analyses for the measured oxides were within 0.3wt% of the expected abundances on average and were also individually corrected for (specifically FeO, SiO_2, MgO and CaO). Analysis of the Kakanui hornblende displayed some larger, systematic error in some oxides, most notably Al_2O_3 (0.9wt% offset on average). Said offsets were corrected for (in all oxides except for Cr_2O_3) and then the data was screened. During data screening, spot analyses with totals outside of the accepted range (99-101wt% for olivine and clinopyroxene; 96-104wt% for amphibole) were removed from the dataset.

4. Results

4.1 Petrography

Thin sections of the new Vardenis samples underwent petrographic analysis using an *Olympus* light microscope. A condensed account of the observed features is reported in Table 4.1.1, while more details can be found in Appendix 1.

Mafic samples (Basanites, Trachybasalts and Trachybasaltic Andesites)

A porphyritic texture was observed in most of the mafic samples, with olivine phenocrysts appearing in all such samples (Figure 4.1.2a&b). Clinopyroxene is also prevalent in these samples (Figure 4.1.2c), found in all but one of the mafic samples. The two aphyric samples do not host any observable olivines. A few of the majority mafic samples have more felsic xenocrysts, often dominated by quartz (Figure 4.1.2d), but these are rare. More common are mafic (often gabbroic) glomerocrysts.

Table 4.1.1: Condensed thin section petrography of the new Vardenis dataset. More information, including sections on textures and alteration, in Appendix 1.

Rock Name abbreviations: R = Rhyolite; TA = Trachyandesite; TB = Trachybasalt; TBA = Trachybasaltic andesite; Te = Tephrite/Basanite; Tr = Trachyte/Trachydacite. Mineral abbreviations: amph = amphibole; bt = biotite; cpx = C=clinopyroxene; kspar = K feldspar; ol = olivine; opx = orthopyroxene; ox = Fe-Ti oxides; plag = plagioclase feldspar; px = pyroxene; qtz = quartz. Texture abbreviations: xen = xenocryst; pseud = pseudomorph.

Sample	Volcano/Place	Eruptive Type	Rock Name	#Mg	Phenocrysts	Groundmass
1.1.19	Khonarasar	Bomb	TBA	56.3	ol, opx	plag, px, ol
1.2.19	Khonarasar	Lava	TBA	57.4	ol, qtz (xen)	plag, ol, cpx, ox
2.1.19	Khrbekner	Lava	TBA	49.3	cpx, ol, amph (pseud)	plag, ol, cpx, ox
2.2.19	Khrbekner	Lava	Te	55.5	cpx, ol	plag, ox, ol, clays
2.3.19	Sardarivar	Lava	TB	54.7	ol, cpx	plag, cpx, ox
2.5.19	N of Sardarivar	Lava	TA	53.6	cpx, ol	plag, cpx, ox
3.1.19	NE of Avdoikar	Lava	Tr	44.1	plag, amph, cpx, ol, kspar	plag, ox, cpx
3.4.19	NW of Avdoikar	Lava	Tr	43.6	plag, cpx, ol	50%crystalline, 50%glass
3.5.19	Unknown	Lava	TBA	43.9	cpx, amph (pseud), ol, plag (xen), qtz(xen)	plag, ox, ol
4.1.19	S of Zolaqar village	Lava	TA	51.8	plag, cpx, ol	plag, cpx, ol, ox
4.3.19	NE of Poqr Khlis	Dyke	TA	37.7	plag, ox, cpx, ol	plag, cpx, ox
4.4.19	Pzuk	Lava	TA	44.6	plag, cpx, amph (pseud)	plag, cpx, glass
4.5.19	Poqr Khlis	Lava	TBA	47.5	plag, cpx, ol	plag, cpx, ox, ol
4.6.19	Poqr Khlis	Scoria	TBA	42.1	ol, plag	glass
4.7.19	Poqr Khlis	Scoria	TBA	46.6	plag, bt, ol, cpx	plag, cpx, ol, ox, bt
4.8.19	Khlis	Lava	TBA	46.2	plag, bt, cpx, ol	plag, cpx, ol, ox, bt
4.9.19	Karmirdosh	Lava	TA	49.5	plag, cpx, ol	plag, ox, cpx
4.10.19	Karmirdosh	Lava	TA	46.6	plag, cpx, qtz, ol	plag, cpx, ox
5.2.19	Chaghatsar (Qechaldagh)	Lava	R	11.9	aphyric	glass
6.1.19	Karmitglukh	Lava	TBA	49.6	cpx, ol	plag, cpx, ox
6.2.19	Karmitglukh	Scoria	TB	51.0	cpx (xen)	plag, cpx
6.3.19	Archisar	Lava	TBA	47.9	aphyric	plag, ox, bt, px
7.1.19	Ananaun	Lava	TA	48.2	plag, cpx, amph (pseud), ox, qtz (xen)+ ol (pseud)	plag, cpx, ox
7.2.19	Muradsar	Lava	TA	48.2	aphyric	plag, px, ox
7.4.19	Kyazhsar	Scoria	TA	47.5	aphyric, qtz (xen)	plag, ol, cpx, ox, glass
7.5.19	Getik	Lava	TBA	53.2	plag (xen), qtz (xen), cpx, ol	plag, ox, ol, cpx

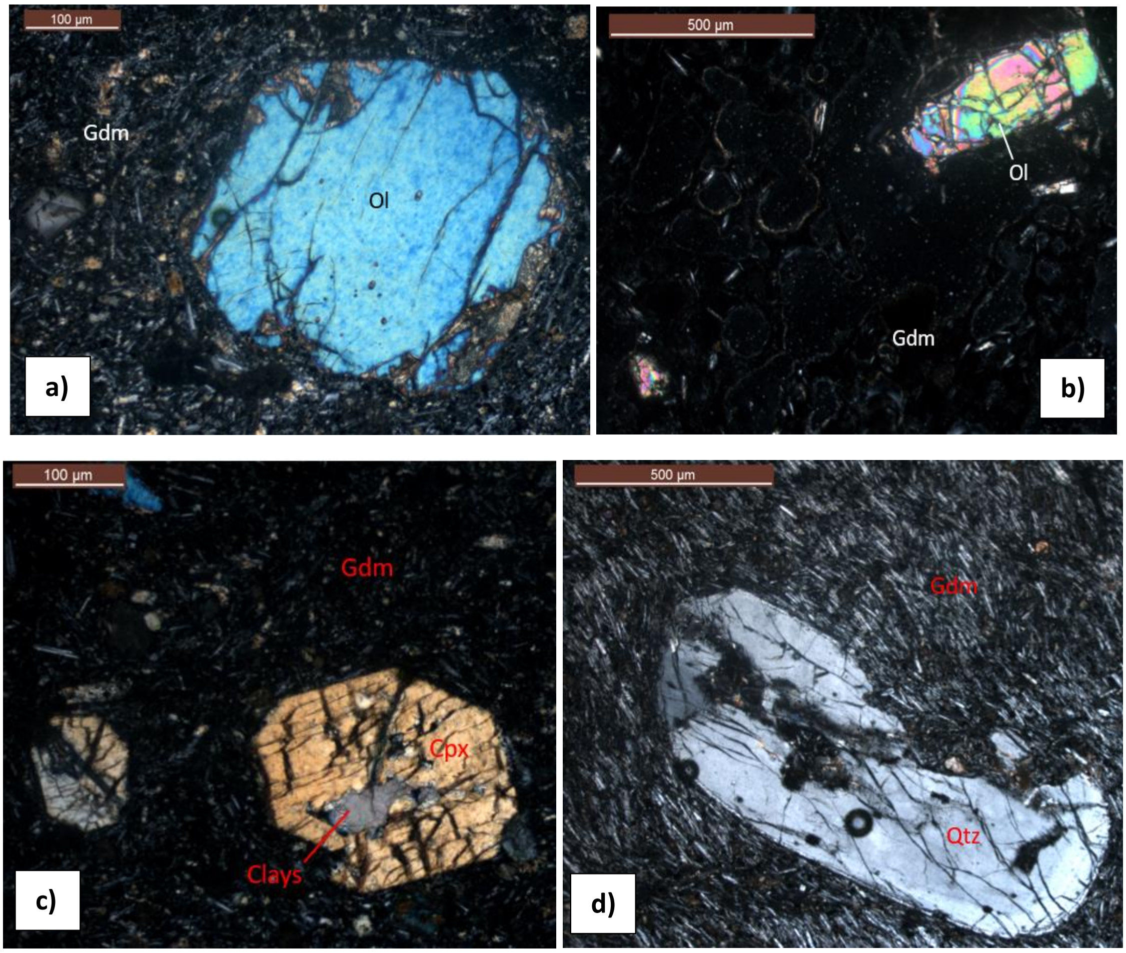

Figure 4.1.2: Petrographic phenomena from the mafic samples. **a)** Large olivine (Ol) phenocryst in basanite/tephrite sample 2.2.19. Slight alteration to clays on parts of the rim. Seriate groundmass (Gdm). **b)** Olivine phenocryst in highly vesicular and glassy trachybasaltic andesite (sample 4.6.19). **c)** Clinopyroxene (Cpx) phenocryst in a seriate groundmass (sample 2.2.19). Patch of clays originating from alteration of the cpx. **d)** Quartz crystal (Qtz) within a pilotaxitic, plagioclase dominated groundmass (sample 3.5.19). Determined to be a xenocryst by the rounded nature and contrast to overall mafic composition of the sample.

The groundmasses of the mafic samples always contain plagioclase; clinopyroxene, Ti-mag and sometimes olivine are also common. It is also sometimes glassy. The most common groundmass textures are pilotaxitic or seriate, but a couple of the samples were sub-ophitic. These rare, sub-ophitic samples are dominated by plagioclase and display rare biotites, both as microphenocrysts and in the groundmass (Figure 4.1.3). Altered amphibole have also been observed in some samples. These more intermediate minerals (biotite and amphibole) and sub-ophitic textures were exclusively observed in trachybasaltic andesites.

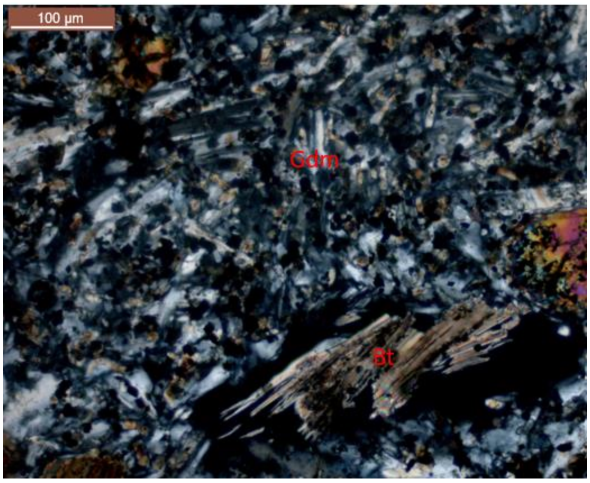

Figure 4.1.3: Biotite (Bt) phenocrysts in sample 4.7.19, a trachybasaltic andesite with a sub-ophitic groundmass texture. Biotite phenocrysts are typically found within vesicles, as can be observed here. The biotite could also be phlogopite, but this is difficult to distinguish from petrography alone.

Intermediate samples (Trachyandesites)

The majority of the trachyandesite samples are porphyritic. Plagioclase feldspar is always present as a phenocryst, with olivine, clinopyroxene, Ti-Mag and amphiboles with altered rims also appearing. Gabbroic glomerocrysts (Figure 4.1.4) and felsic xenocrysts are also observed, as with the mafic suite.

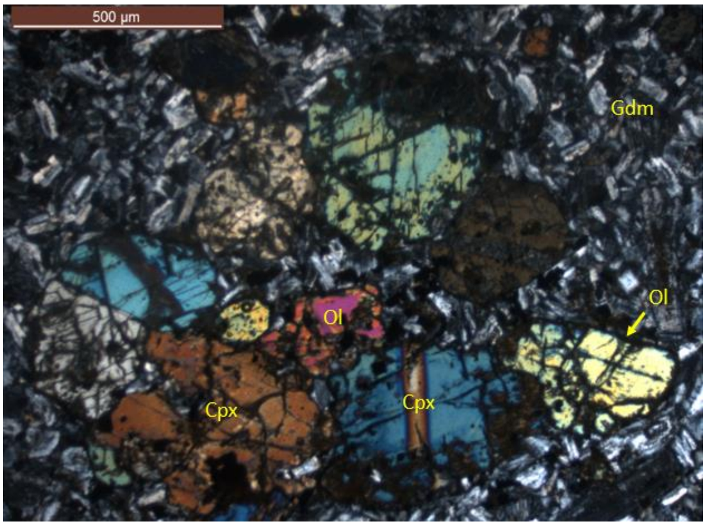

Figure 4.1.4: Gabbroic glomerocryst primarily composed of olivine (Ol) and clinopyroxene (Cpx) in trachyandesite 4.3.19. The groundmass (Gdm) is sub-ophitic, dominated by plagioclase with rare clinopyroxene and oxides.

In the groundmass, plagioclase is ubiquitous, with clinopyroxene and Ti-mag only slightly less prevalent. Olivine is also observed, but rarely. Sub-ophitic and dacitic textures are more common in the intermediate groundmass than was the case for the mafic samples.

Felsic samples (Trachydacites and Rhyolites)

The only rhyolitic sample is an obsidian, and thus thin-section petrography did not provide much insight.

The trachydacites are both porphyritic, with plagioclase, clinopyroxene and rare olivine phenocrysts. Sample 3.1.19 also has K feldspar and largely unaltered amphibole phenocrysts (Figure 4.1.5c). A sub-ophitic texture was observed between plagioclase and amphibole in this sample (Figure 4.1.5a&b).

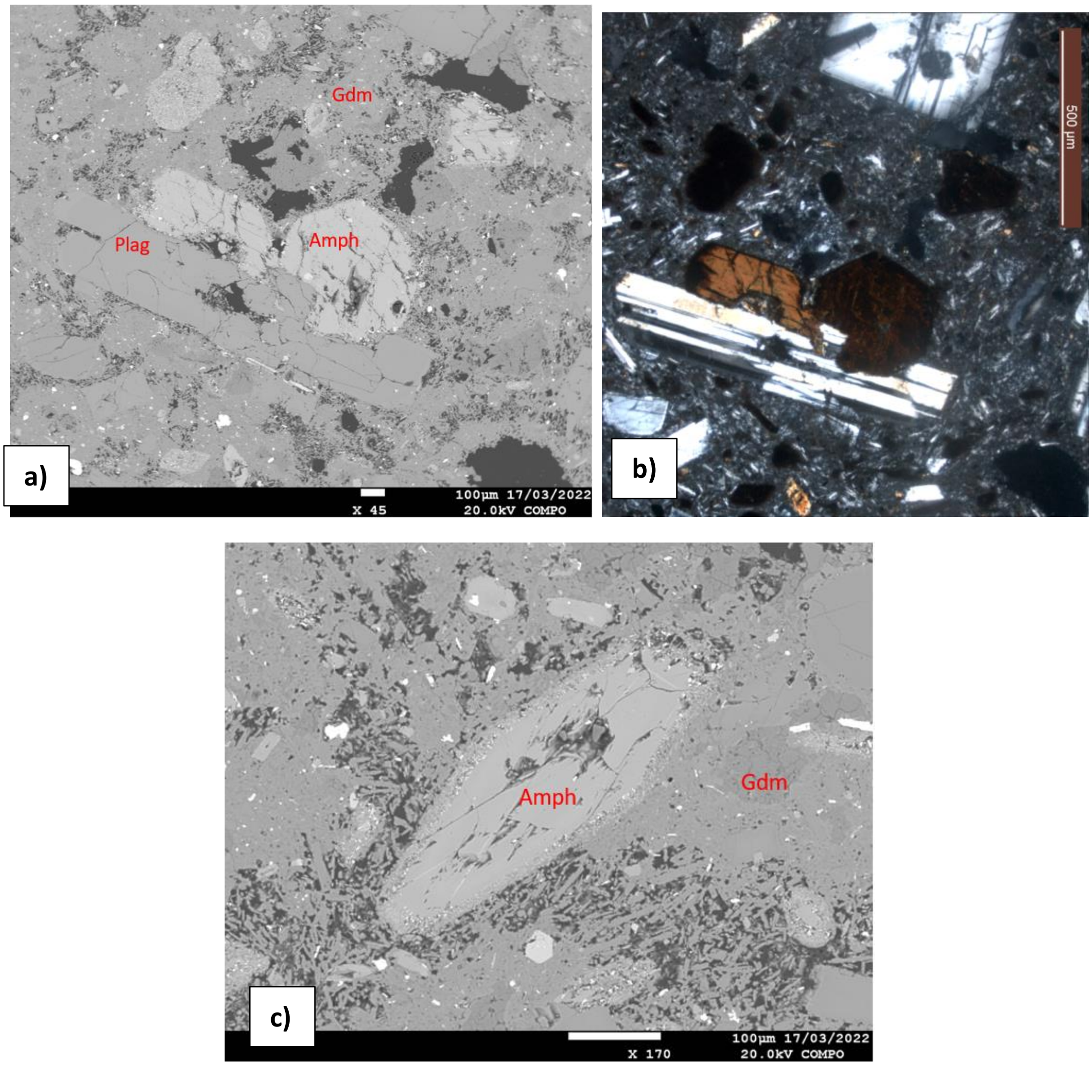

Figure 4.1.5: Images from Trachydacite sample 3.1.19. **a)** Sub-ophitic relationship between an amphibole (Amph) and plagioclase (Plag) phenocrysts photographed via the Scanning Electron Microscope (SEM). A reaction rim is present on the amphiboles, except for on the surfaces in contact with the plagioclase, showing that alteration occurred after these crystals grew into contact of one another. Seriate groundmass. **b)** Light microscope image of the same relationship shown in 4.1.5a. **c)** A euhedral amphibole microphenocryst. Distinct and consistent reaction rim around the amphibole.

The groundmass contains plagioclase, Ti-mag and cpx, as well as being somewhat glassy. Seriate texture dominates the crystalline groundmass, but in one sample this only makes up approximately 50%.

Crystallisation Order

After extensive petrographic investigation, the crystallisation order for the new Vardenis dataset was determined to be the same as that identified by Sugden et al. (2019); olivine + Fe-Ti oxides ± apatite → clinopyroxene + Fe-Ti oxides ± olivine ± amphibole → clinopyroxene + plagioclase + Fe-Ti oxides ± amphibole ± phlogopite/biotite → plagioclase + potassium[K] feldspar + Fe-Ti oxides ± phlogopite/biotite.

4.2 Geochemical Data

This project focuses on expanding the geochemical database for the Vardenis Volcanic Highland. Samples were collected from across the highland (see Table 4.2.3 & Figure 3.1.2). This sampling pattern was not restricted to a certain area of the stratigraphy but is likely biased towards the youngest lithologies, which have more abundant fresh outcrop. A wide compositional range was collected, varying from tephrites/basanites to rhyolites.

Major Element Characteristics

Each of the samples underwent major and trace element analysis via ICP-MS. This analysis confirmed the field observations of a wide compositional range from basanite to rhyolite. The new Vardenis dataset exceeds the SiO_2 range reported for Vardenis in Sugden et al. (2019) but are encompassed by the total alkali [Na_2O + K_2O] and K_2O ranges reported in the same work (Figures 4.2.1 and 4.2.2). The latter identifies the new dataset as high-K calc-alkaline to alkaline/shoshonitic series.

When SiO_2 is plotted against other major elements in Harker diagrams, the new data continues to fit the trends identified by Sugden et al. (2019). MgO and P_2O_5 both show a curved decrease with the increase of SiO_2 (Figure 4.2.4), indicative of fractional crystallisation.

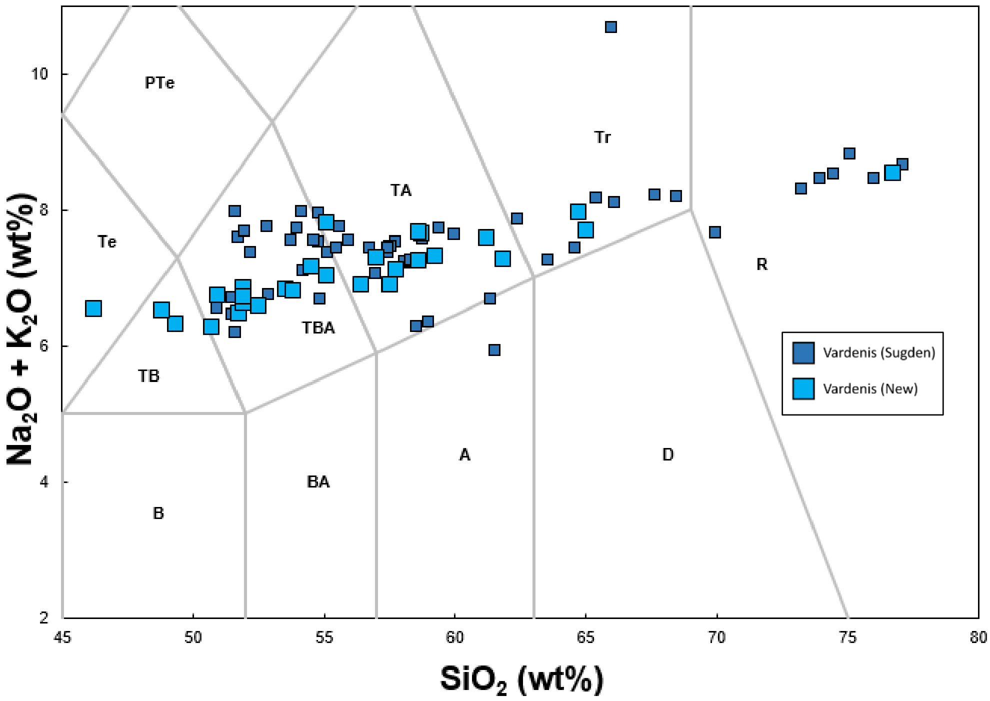

Figure 4.2.1: Total Alkalis vs SiO_2 plot, showing the new Vardenis dataset against that of Sugden et al. (2019). There is a clear spread of samples across the compositional range.

A-Andesite; B-Basalt; BA-Basaltic Andesite; D-Dacite; PTe-Phonotephrite; R-Rhyolite; TA-Trachyandesite; TB-Trachybasalt; TBA-Trachybasaltic Andesite; Te-Tephrite/Basanite; Tr-Trachyte/Trachydacite. Plot template from Le Bas et al. (1986).

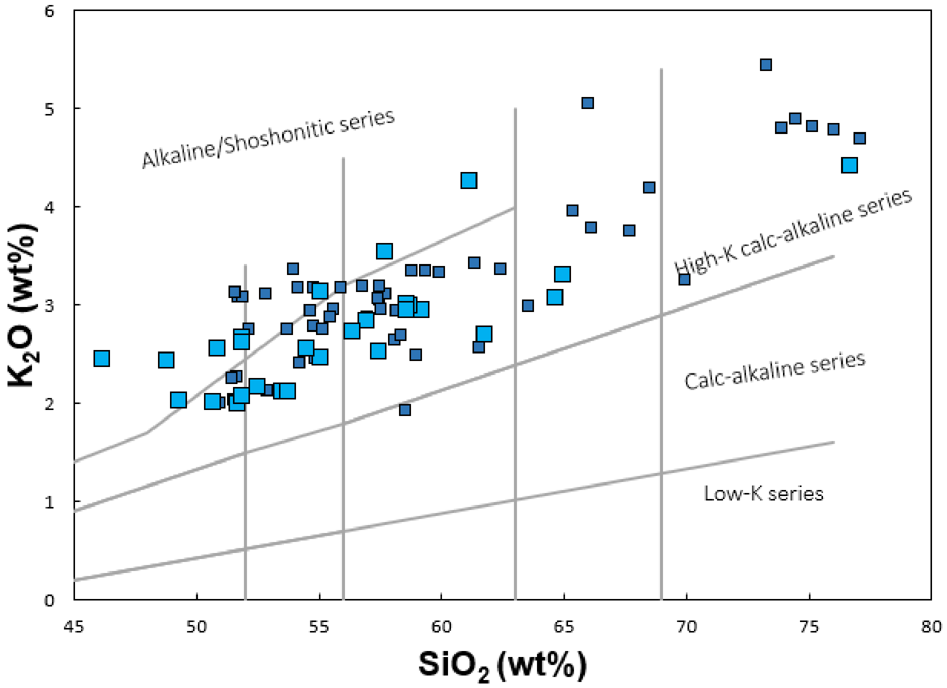

Figure 4.2.2: K_2O vs SiO_2. The new dataset is generally enriched in K_2O, falling in 'High-K calc-alkaline series' and 'Alkaline/Shoshonitic series'. This is in line with the findings of Sugden et al. (2019).

Plot template from Ewart (1982).

Table 4.2.3: Whole rock major and trace element compositions of all samples from the new Vardenis dataset. Analysed by ALS labs, Vancouver, Canada. Data can also be seen in Appendix 2. Major oxides (SiO_2 -BaO) are given in wt%; trace elements (Ba-Zr) are given in ppm.

Sample	1.1.19	1.2.19	2.1.19	2.2.19	2.3.19
Latitude	40.13540	40.14032	40.08715	40.08903	40.05707
Longitude	45.63475	45.62102	45.42273	45.41922	45.41943
Volcano/Location	Khonarasar	Khonarasar	Khrbekner	Khrbekner	Sardarivar
Sample Type	Bomb	Lava	Lava	Lava	Lava
SiO_2	50.7	51.7	51.9	46.2	49.3
Al_2O_3	16.3	16.5	17.65	17.25	16.55
Fe_2O_3	9.48	9.11	9.12	9.82	10.55
CaO	8.27	8.4	8.61	11.15	9.53
MgO	6.17	6.2	4.48	6.18	6.43
Na_2O	4.27	4.5	4.21	4.11	4.3
K_2O	2.01	1.99	2.66	2.45	2.02
Cr_2O_3	0.021	0.017	0.009	0.007	0.025
TiO_2	1.34	1.34	1.13	1.31	1.25
MnO	0.15	0.14	0.14	0.15	0.15
P_2O_5	0.74	0.75	0.9	0.93	0.85
SrO	0.15	0.15	0.19	0.19	0.18
BaO	0.09	0.08	0.11	0.12	0.1
Total	100.61	101.26	101.78	100.43	101.37
LOI	0.92	0.38	0.67	0.56	0.13
#Mg	56.3	57.4	49.3	55.5	54.7
Ba	744	751	964	1025	853
Ce	101	101	138.5	127.5	105
Cr	160	130	70	50	190
Cs	0.45	0.43	0.62	1.24	0.7
Dy	4.4	4.34	3.88	4.2	3.8
Er	2.6	2.39	1.98	2.09	2.05
Eu	1.9	1.91	2.09	2.38	1.99
Ga	18.6	18.8	20.3	20.2	19
Gd	5.56	5.69	5.79	6.81	5.85
Hf	4.2	4.1	4.4	4.2	3.3
Ho	0.92	0.9	0.74	0.81	0.76
La	55.8	55.6	73.5	63.2	52.5
Lu	0.34	0.33	0.26	0.28	0.26
Nb	19.8	19.8	26.9	27	21.4
Nd	39.8	40.2	52.6	55.4	46.1
Pr	11.3	11.3	15.6	15.35	12.45
Rb	32.1	32.5	42.7	49.6	43
Sm	6.99	7.13	8.48	9.69	7.76
Sn	2	1	2	1	1
Sr	1255	1260	1655	1635	1490
Ta	0.9	0.9	1.1	1	1
Tb	0.82	0.81	0.74	0.85	0.75
Th	4.8	4.85	7.93	7.08	4.64
Tm	0.35	0.34	0.26	0.28	0.29
U	1.09	1.22	1.42	1.72	1.26
V	182	180	191	267	239
W	1	<1	1	1	<1
Y	23.5	22.8	19.5	21.4	19.2
Yb	2.4	2.36	1.78	1.97	1.84
Zr	206	207	214	196	153

Table 4.2.3 continued

Sample	2.5.19	3.1.19	3.4.19	3.5.19	4.1.19
Latitude	40.03827	39.97513	39.97522	39.98555	40.05092
Longitude	45.42363	45.32697	45.30572	45.23988	45.40112
Volcano/Location	N of Sardarivar	NE of Avdoikar	NW of Avdoikar		S of Zolaqar village
Sample Type	Lava	Lava	Lava	Lava	Lava
SiO_2	55.1	65	64.7	55.1	59.2
Al_2O_3	16.15	15.85	16.5	17.2	16.55
Fe_2O_3	6.9	5.25	4.31	7.28	5.87
CaO	7.95	4.13	4.42	7.37	5.99
MgO	4.03	2.09	1.68	2.87	3.18
Na_2O	4.69	4.41	4.91	4.59	4.38
K_2O	3.13	3.3	3.06	2.46	2.94
Cr_2O_3	0.009	0.005	0.004	0.011	0.009
TiO_2	0.9	0.57	0.53	0.98	0.75
MnO	0.12	0.08	0.09	0.12	0.09
P_2O_5	0.66	0.31	0.34	0.72	0.51
SrO	0.17	0.1	0.11	0.14	0.13
BaO	0.11	0.1	0.1	0.09	0.11
Total	101.27	101.43	101.35	100.22	100.31
LOI	1.35	0.23	0.6	1.29	0.6
#Mg	53.6	44.1	43.6	43.9	51.8
Ba	1005	862	892	821	934
Ce	117.5	79.4	91.2	105.5	92.4
Cr	70	40	30	80	60
Cs	0.92	1.66	1.6	0.64	1.22
Dy	3.08	2.29	2.55	3.25	2.63
Er	1.59	1.2	1.4	1.59	1.38
Eu	1.66	1.1	1.17	1.64	1.39
Ga	19	18.8	19.6	19.2	18.8
Gd	4.84	3.15	3.47	4.76	4.04
Hf	4.4	4.2	5	3.9	4.4
Ho	0.59	0.48	0.5	0.61	0.51
La	63.8	45.6	49.4	57.7	51.3
Lu	0.19	0.19	0.22	0.25	0.18
Nb	27.1	18.3	26.9	19.8	18.7
Nd	43.7	29.2	33.4	40.2	35.6
Pr	12.95	8.52	9.86	11.7	10.4
Rb	58.8	88.3	88.4	38.5	59.4
Sm	6.92	4.45	5.19	6.22	5.82
Sn	1	1	1	1	2
Sr	1400	799	922	1230	1060
Ta	1.3	1.1	1.6	0.9	0.9
Tb	0.62	0.43	0.47	0.59	0.53
Th	10.6	15.85	20.4	6.6	9.82
Tm	0.23	0.18	0.22	0.22	0.21
U	2.87	4.84	5.72	1.44	2.43
V	160	78	78	154	124
W	1	1	2	3	1
Y	16	12.3	13.7	16.2	13.4
Yb	1.61	1.21	1.43	1.56	1.44
Zr	213	185	221	182	206

Table 4.2.3 continued

Sample	4.3.19	4.4.19	4.5.19	4.6.19	4.7.19
Latitude	40.00185	40.00378	39.99865	39.99865	39.99865
Longitude	45.65522	45.38612	45.39123	45.39123	45.39123
Volcano/Location	NE of Poqr Khlis	Pzuk	Poqr Khlis	Poqr Khlis	Poqr Khlis
Sample Type	Dike	Lava	Lava	Scoria	Scoria
SiO_2	58.7	57.5	53.5	52.5	51.9
Al_2O_3	16.6	16.45	16.9	17.25	16.35
Fe_2O_3	6.48	7.22	9.41	9.34	9.43
CaO	4.46	5.95	7.52	7.09	7.23
MgO	1.98	2.94	4.29	3.43	4.16
Na_2O	4.68	4.38	4.74	4.43	4.56
K_2O	2.99	2.52	2.11	2.16	2.07
Cr_2O_3	0.011	0.006	0.008	0.006	0.009
TiO_2	0.85	1.02	1.35	1.34	1.3
MnO	0.18	0.14	0.14	0.12	0.14
P_2O_5	0.56	0.64	0.79	0.75	0.77
SrO	0.14	0.12	0.15	0.14	0.15
BaO	0.11	0.09	0.09	0.09	0.08
Total	100.5	99.39	101.1	99.76	98.23
LOI	2.76	0.41	0.1	1.11	0.08
#Mg	37.7	44.6	47.5	42.1	46.6
Ba	971	847	752	757	758
Ce	102	98.7	104.5	101.5	107
Cr	80	40	60	50	60
Cs	1.41	0.47	0.25	0.24	0.18
Dy	2.97	3.28	4.2	3.96	4
Er	1.57	1.86	2.17	2.33	2.1
Eu	1.58	1.53	1.8	1.88	1.96
Ga	19.1	20	19.6	19.2	19.2
Gd	4.62	4.61	5.48	5.76	5.83
Hf	4.5	4.7	4.2	4.2	4.1
Ho	0.61	0.71	0.8	0.83	0.77
La	55.1	54.8	56	56.3	58.5
Lu	0.22	0.25	0.28	0.3	0.29
Nb	21.3	20.7	20.9	20.9	21.2
Nd	39.4	37.7	42.3	42.4	43
Pr	11.35	10.95	11.95	11.95	12.3
Rb	64.6	50.1	29.7	34.1	30
Sm	6.7	6.47	7.35	7.67	7.38
Sn	1	1	1	3	2
Sr	1065	1045	1265	1215	1295
Ta	1.1	1	0.9	1	1
Tb	0.59	0.67	0.79	0.8	0.74
Th	11.5	9.28	4.58	4.73	4.71
Tm	0.21	0.25	0.31	0.3	0.31
U	2.95	2.17	0.96	1.05	1.02
V	138	171	192	190	192
W	1	1	<1	<1	1
Y	15.6	18.3	21.4	21.4	21.8
Yb	1.44	1.82	2.22	2.09	2.07
Zr	212	216	202	203	200

Table 4.2.3 continued

Sample	4.8.19	4.9.19	4.10.19	5.2.19	6.1.19
Latitude	39.99425	39.99373	39.99373	39.92623	39.85217
Longitude	45.39775	45.40313	45.40313	45.86838	45.76233
Volcano/Location	Khlis	Karmirdosh	Karmirdosh	Chaghatsar (Qechaldagh)	Karmitglukh
Sample Type	Lava	Lava	Lava	Lava	Lava
SiO_2	53.8	57	61.8	76.7	51.9
Al_2O_3	17.2	16.25	16.6	12	16.8
Fe_2O_3	9.26	7.39	5.13	0.88	9.07
CaO	7.64	6.15	4.88	0.47	8.08
MgO	4.01	3.65	2.26	0.06	4.5
Na_2O	4.71	4.47	4.59	4.14	4.11
K_2O	2.11	2.83	2.7	4.41	2.61
Cr_2O_3	0.006	0.005	0.005	0.002	0.003
TiO_2	1.38	0.86	0.76	0.1	1.36
MnO	0.14	0.12	0.05	0.06	0.14
P_2O_5	0.8	0.6	0.46	0.01	1
SrO	0.15	0.12	0.11	<0.01	0.22
BaO	0.09	0.1	0.1	<0.01	0.12
Total	101.69	99.48	100.28	99.44	100.56
LOI	0.39	-0.07	0.83	0.61	0.65
#Mg	46.2	49.5	46.6	11.9	49.6
Ba	827	920	935	32.4	1080
Ce	107.5	105.5	89.3	55	143
Cr	40	40	40	20	20
Cs	0.26	0.59	2.11	3.68	0.36
Dy	4.3	3.37	3.75	1.32	4.22
Er	2.37	1.85	2.07	1.03	2.09
Eu	1.99	1.53	1.56	0.17	2.35
Ga	18.3	17.4	18	14.7	17.6
Gd	5.35	4.36	4.81	1.16	6.2
Hf	4.1	4.3	4.2	3.5	4.1
Ho	0.82	0.67	0.74	0.29	0.79
La	60.6	63.3	48	36.9	75.1
Lu	0.3	0.24	0.27	0.21	0.28
Nb	21.8	20.6	19.6	34.2	24.1
Nd	44	37.8	37.9	12.6	61.5
Pr	13	12.05	11.05	5.1	18.05
Rb	30.2	57.4	63.4	152	32.6
Sm	7.44	6.13	6.46	1.71	9.45
Sn	1	1	1	1	1
Sr	1385	1075	989	15.1	2020
Ta	1	0.9	1.1	2.2	0.9
Tb	0.78	0.62	0.71	0.2	0.8
Th	5.08	9.72	10.95	28.1	4.38
Tm	0.31	0.24	0.29	0.2	0.27
U	1.11	2.21	2.98	8.29	1
V	204	139	126	<5	220
W	<1	1	1	3	<1
Y	23	18.2	22.7	10.1	21.5
Yb	2.09	1.68	1.98	1.28	1.89
Zr	198	206	186	108	196

Table 4.2.3 continued

Sample	6.2.19	6.3.19	7.1.19	7.2.19	7.4.19	7.5.19
Latitude	39.85605	39.87460	39.88688	39.89410	39.90945	39.92560
Longitude	45.77918	45.73065	45.61458	45.59363	45.58232	45.56187
Volcano/Location	Karmitglukh	Archisar	Ananaun	Muradsar	Kyazhsar	Getik
Sample Type	Scoria	Lava	Lava	Lava	Scoria	Lava
SiO_2	48.8	50.9	58.6	58.6	56.4	54.5
Al_2O_3	15.8	16.65	15.15	15.5	16.9	16.15
Fe_2O_3	8.29	8.73	6.42	6.52	8.26	7.47
CaO	7.53	7.65	6.6	5.82	6.41	6.9
MgO	4.35	4.05	3.01	3.06	3.78	4.28
Na_2O	4.1	4.2	4.69	4.32	4.18	4.63
K_2O	2.42	2.55	3	2.94	2.72	2.55
Cr_2O_3	0.004	0.004	0.008	0.007	0.013	0.013
TiO_2	1.24	1.3	0.97	0.82	0.96	1.03
MnO	0.13	0.13	0.1	0.11	0.13	0.13
P_2O_5	0.94	0.93	0.72	0.61	0.72	0.78
SrO	0.2	0.21	0.14	0.11	0.13	0.13
BaO	0.11	0.11	0.1	0.11	0.1	0.1
Total	94.58	98.03	99.82	99.78	101.6	98.89
LOI	0.67	0.62	0.31	1.25	0.9	0.23
#Mg	51.0	47.9	48.2	48.2	47.5	53.2
Ba	1050	1075	965	998	929	891
Ce	138	137.5	110.5	106.5	116	115.5
Cr	30	20	60	50	90	90
Cs	0.36	0.18	1.24	0.92	0.73	0.4
Dy	4.1	4.13	3.48	3.35	3.74	3.76
Er	1.98	2.12	1.87	1.8	2.02	1.92
Eu	2.13	2.22	1.72	1.54	1.74	1.72
Ga	17.3	18	17.6	17.5	17.9	18
Gd	6.23	6.03	5.04	4.52	4.82	4.99
Hf	3.9	4	4.2	4.6	4.5	4.6
Ho	0.76	0.81	0.69	0.67	0.73	0.77
La	73	73.7	63.3	64.4	68	67.1
Lu	0.27	0.27	0.25	0.25	0.29	0.28
Nb	22.9	23.6	24.2	22.1	24.7	24.2
Nd	59.1	57.9	43.4	39	43.5	43.3
Pr	17.15	16.95	13.05	12.25	13.65	13.25
Rb	32.2	32.2	69.7	68.1	45.9	46.3
Sm	9.35	9.19	7.24	5.99	7.08	7.17
Sn	2	1	1	13	9	1
Sr	1920	1900	1335	1060	1205	1215
Ta	0.9	1	1.2	1.1	1.1	1
Tb	0.8	0.79	0.68	0.6	0.7	0.74
Th	4.29	4.51	11.1	11	8.54	7.29
Tm	0.29	0.3	0.26	0.24	0.27	0.29
U	0.89	0.94	3.7	2.48	2.16	1.67
V	199	185	134	128	146	157
W	1	<1	1	1	1	1
Y	20.9	21.5	19	17.7	20.4	20.5
Yb	1.92	1.8	1.75	1.55	1.8	1.79
Zr	190	198	197	224	220	220

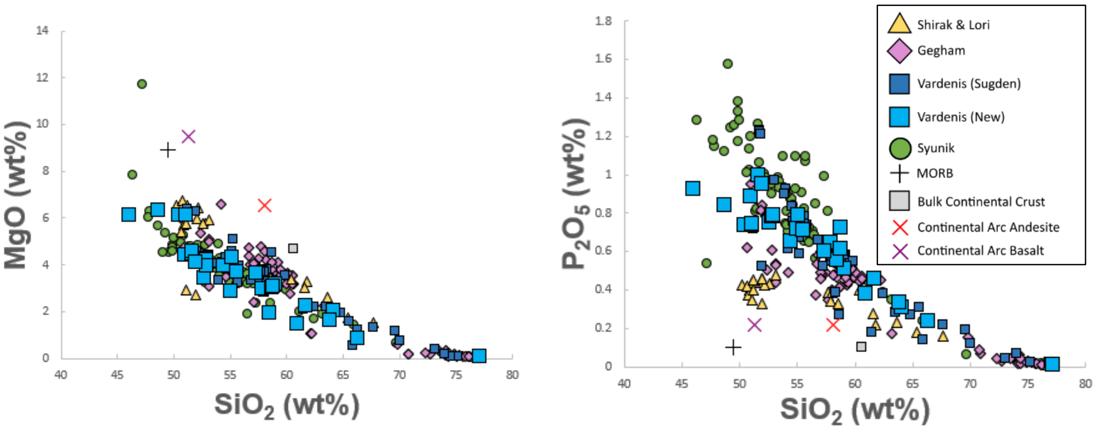

Figures 4.2.4: Select Harker diagrams for MgO and P_5O_5. Clear curved, negative trends between both MgO and P_2O_5 and SiO_2 are evident.

Vardenis and Syunik data from Sugden et al. (2019), Gegham data from Savov et al. (unpublished), Shirak & Lori data from Neill et al. (2015). MORB data is averaged from Sun et al. (1979). Continental Arc Basalt and Continental Arc Andesite from Kelemen et al. (2003).

Trace Element Characteristics

Upon being normalised to N-MORB, the trace element profiles for the new Vardenis dataset show several anomalies. There are enrichments in the Light Rare Earth Elements (LREE), Ba and Sr, as well as in K. In contrast, the High Field Strength Elements (HFSE) Nb, Ta and Ti all show a depletion in respect to the other trace elements (Figure 4.2.5). When considered together, these anomalies are indicative of a subduction-modified mantle source (Pearce et al., 2006).

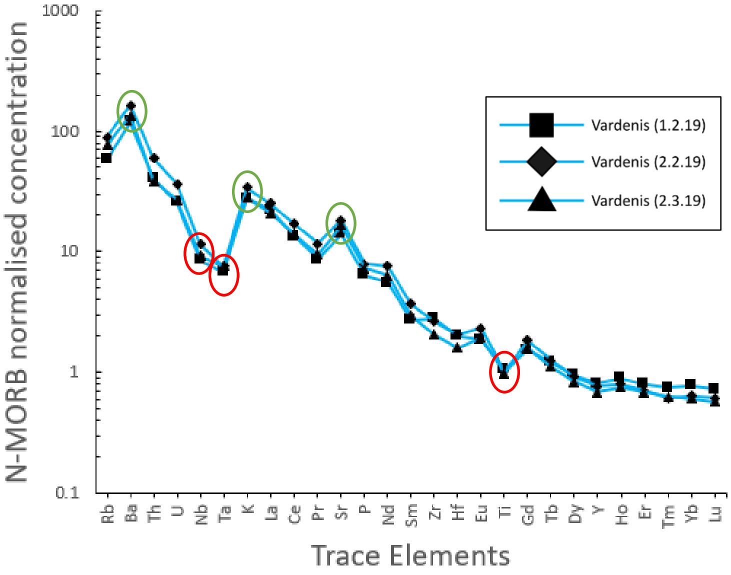

Figure 4.2.5: N-MORB normalised trace element profile for the three most mafic (highest MgO wt%) samples from the new Vardenis dataset. Enrichments of the profiles are circled in green, whilst depletions are circled in red.

N-MORB data from Sun & McDonough (1989).

When compared to the surrounding volcanic highlands, a pattern of increasing LREE enrichment in the southward direction is evident (Figure 4.2.6). This could indicate an increasing subducted-component contribution to the mantle source or a different degree of melting.

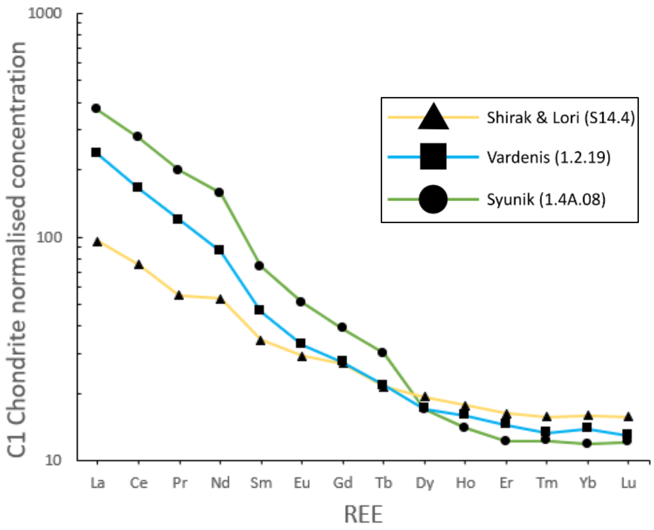

Figure 4.2.6: Chondrite (C1) normalised REE profiles for the most mafic samples in Shirak & Lori (6.6wt%), Syunik (5.2wt%), and the new Vardenis dataset (6.4wt%). There is a clear difference in the profiles, with the northern-most region (Shirak & Lori) having the shallower (and thus more similar to Continental Arc average) profile, whilst Syunik has the steepest.

Chosen samples had the highest MgO wt% in their respective datasets. Vardenis sample from the new dataset; Syunik from Sugden et al. (2019); Shirak & Lori from Neill et al. (2015). C1 Chondrite data from Sun & McDonough (1989).

In conflict with this is the Th/Yb vs Ta/Yb graph (Figure 4.2.7). Th and Ta have similar degrees of incompatibility during melting or crystallisation of mafic or intermediate minerals. All Lesser Caucasus samples show an enrichment in Th/Yb relative to MORB but maintain a sub-parallel nature with the expected profile of mantle fractional crystallisation. Th is a melt-mobile element, and as such its ubiquitous enrichment indicates an input of arc melt (the subducted component) across the region (Keskin et al., 1998), which has subsequently undergone the expected fractional crystallisation to create the wide compositional range observed across Armenia. This anomaly doesn’t vary significantly across the region, especially not between the adjacent highlands of Gegham, Vardenis and Syunik. This suggests that the arc melt input does not vary significantly from the NW to the SE of the Lesser Caucasus.

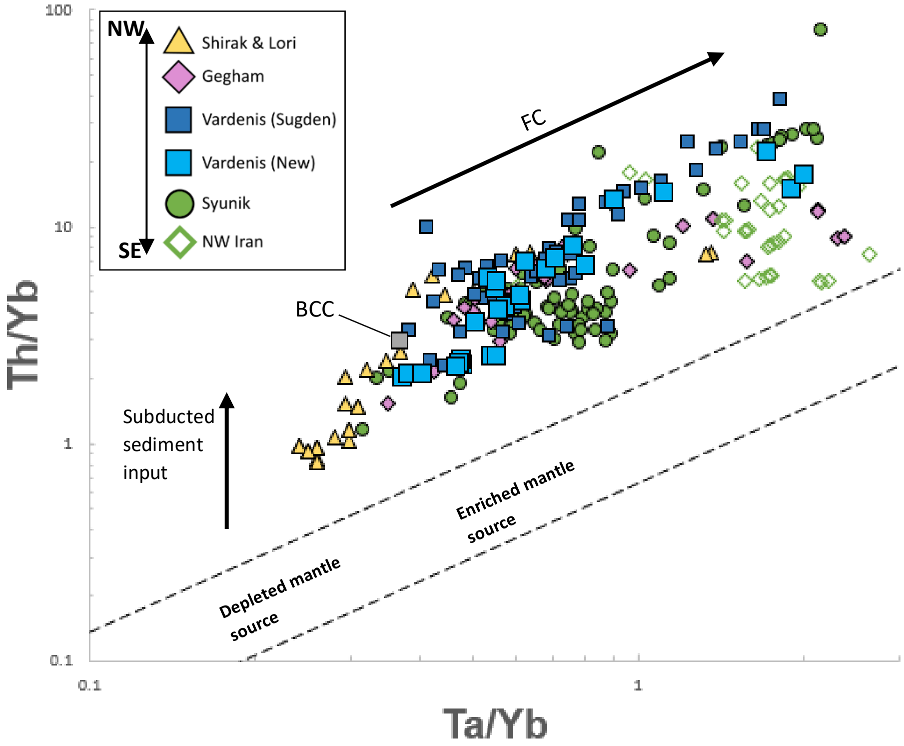

Figure 4.2.7: Th/Yb vs Ta/Yb plot after Pearce (1983), specifically the fractional crystallisation vector and mantle source array. For all Lesser Caucasus (and NW Iran) data there is a clear input of metasomatised material ('subducted sediment input'), raising the otherwise normal fractional crystallisation pattern to be more enriched in Th than the normal mantle source array.

Data from four different volcanic highlands across the Lesser Caucasus (from NW to SE: Shirak & Lori (Neill et al., 2015); Gegham (Savov, unpublished); Vardenis (New dataset and Sugden et al., 2019); Syunik (Sugden et al., 2019)) and from NW Iran (Allen et al., 2013) (the south-eastern endmember of the system). Bulk Continental Crust (BCC) data from Rudnick & Gao (2003).

Sr-Nd isotopes

The new Vardenis dataset reveals $^{87}Sr/^{86}Sr$ ratios that show relatively narrow range of 0.703993-0.705029 (Table 4.2.8). This is a significantly wider range of Sr isotopes than in the Vardenis range reported in Sugden et al. (2019) (0.70418-0.70451). However, this wide range is established by two outlying samples (the higher of which is felsic, so likely more radiogenic); the majority of the values are similar to the previously established data. The new εNd range is relatively restricted (2.46-3.61) and shows a good similarity to the Sugden et al. (2019) Vardenis dataset (2.79-3.86). In both $^{143}Nd/^{144}Nd$ and εNd, this suite of Vardenis samples has some of the lowest values of any previously analysed Lesser Caucasus samples (similar to those measured for Syunik), disrupting the previously established NW-SE trend of increasing enrichment (Sugden et al., 2019) (Figure 4.2.9).

Table 4.2.8: Sr & Nd isotope ratios for the new Vardenis dataset.

Samples analysed for Sr and Nd at the University of Leeds with Ivan Savov and Jason Harvey.

	Rock Type	**$^{87}Sr/^{86}Sr$**	**±2σ ($x10^{-6}$)**	**$^{143}Nd/^{144}Nd$**	**±2σ ($x10^{-6}$)**	**εNd**
1.1.19	TBA	0.704444	4	0.512784	6	2.85
1.2.19	TBA	0.704377	6			
2.1.19	TBA	0.704259	8	0.512823	4	3.61
2.2.19	Te	0.704402	6			
2.3.19	TB	0.704687	4	0.512764	2	2.46
2.5.19	TA	0.704291	5			
3.1.19	Tr	0.704473	5			
4.1.19	TA	0.704439	6	0.512789	7	2.95
4.3.19	TA	0.704507	6	0.512768	6	2.54
4.4.19	TA	0.704463	4			
4.5.19	TBA	0.704370	9	0.512779	8	2.75
4.6.19	TBA	0.704407	4	0.512810	5	3.36
5.2.19	R	0.705029	5	0.512782	21	2.81
6.1.19	TBA	0.704380	5			
6.2.19	TB	0.704321	6	0.512773	5	2.63
7.4.19	TA	0.704336	6			
7.5.19	TBA	0.703993	5	0.512794	3	3.04

All values were corrected to standard averages: NBS 987 standard for $^{87}Sr/^{86}Sr$; La Jolla International standard for $^{143}Nd/^{144}Nd$.

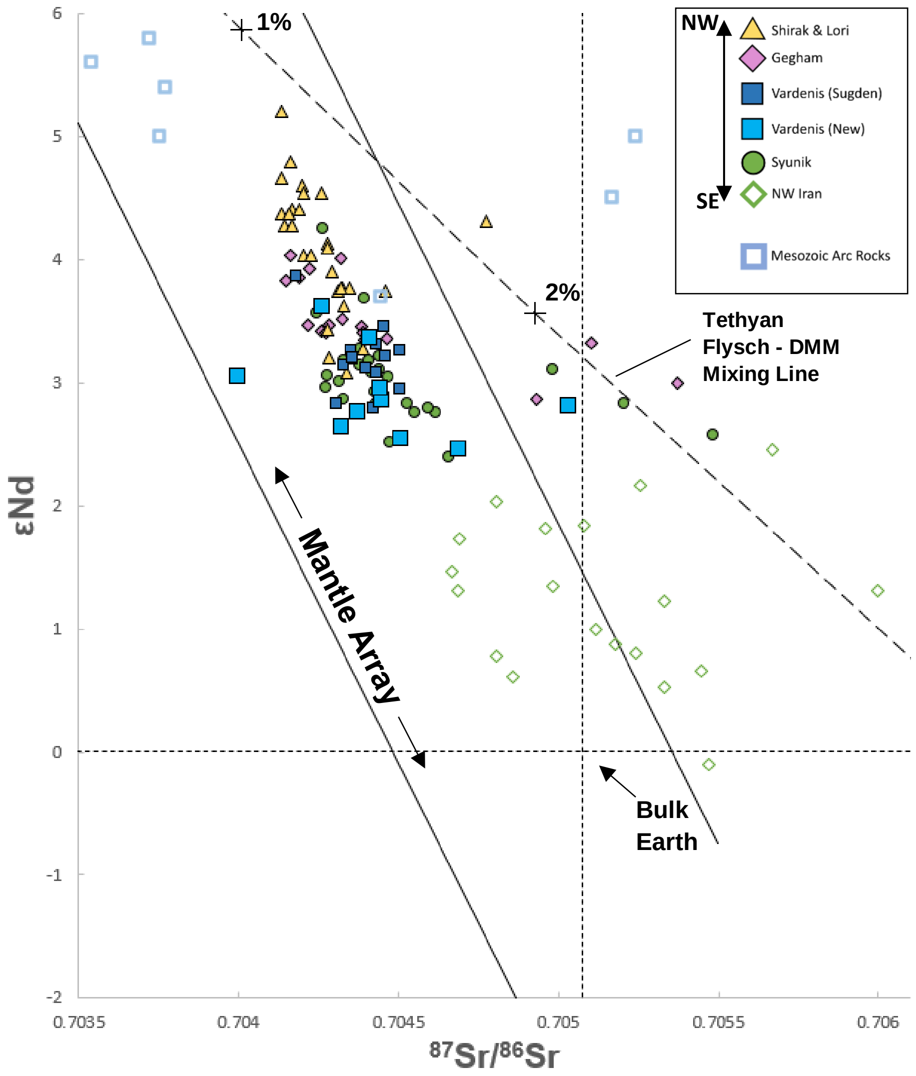

Figure 4.2.9: εNd vs $^{87}Sr/^{86}Sr$. Isotope data from across Armenia showing variation from NW (Shirak & Lori) to SE (Syunik) in the post-collisional magmatic rocks. New Vardenis dataset plots out of pattern (largely overlapping with the Syunik data), potentially suggesting a connection in the magmatic systems of the Vardenis and Syunik volcanic highlands. The Mesozoic Arc Rocks display a pre-collisional example of magmatism, whilst the NW Iran dataset represents a more enriched endmember than that of Syunik or the new dataset.

'Vardenis (Sugden)' and Syunik data from Sugden et al. (2019); Shirak & Lori from Neill et al. (2015); Gegham from Savov et al (unpublished); NW Iran from Allen et al. (2013). Mesozoic Arc Rocks from Mederer et al. (2013). Mantle Array and Bulk Earth values from Rollinson (1993). The mixing line is between depleted MORB mantle (DMM) (White and Hofmann, 1982) and Tethyan Flysch (Prelević et al., 2008). Graph is adapted from Sugden et al. (2019)

[B] and $\delta^{11}B$ systematics

The samples selected for whole rock B analysis were those determined to be the most mafic after geochemical analysis (as well as the only rhyolite in the suite). However, due to delays in receiving the data, not all of the most mafic samples were analysed, and not all of the samples selected were as mafic as hoped (lower MgO wt% than expected).

Upon analysis, a [B] range of 1.44-7.17ppm was determined, within which both Vardenis samples from Sugden et al. (2020) fall. For $\delta^{11}B$, the new dataset ranges from -0.75 to -5.1‰ (Table 4.2.10), which overlaps well with the previous data from the SLC. (Figure 4.2.11).

Table 4.2.10: Data from the B analysis for the new Vardenis dataset shown alongside SiO_2 and MgO whole rock data. B analysis at CNR Pisa with Samuele Agostini. Whole Rock analysis completed by ALS labs, Vancouver.

	Rock Type	[B] (ppm)	$\delta^{11}B$	±2σ ($x10^{-6}$)	SiO_2	MgO
New Vardenis						
1.1.19	TBA	1.6	-5.1	0.21	50.7	6.17
2.3.19	TB	1.44	-1.45	0.15	49.3	6.43
4.1.19	TA	5.13	-0.75	0.03	59.2	3.18
4.3.19	TA	4.8	-4.95	0.03	58.7	1.98
4.6.19	TBA	2.31	-2.82	0.05	52.5	3.43
5.2.19	R	7.17	-4.1	0.02	76.7	0.06
6.2.19	TB	1.59	-3.52	0.14	48.8	4.35

When compared to MORB ([B]=0.19 (primitive mantle) & $\delta^{11}B$ = -7.1±0.9‰ (Marschall et al., 2017)), the Vardenis values are consistently enriched in B, indicating the imparting of B to the mantle source from a fluid component, likely derived from subduction influence (Sugden et al., 2020). However, the low B/Nb values (0.07-0.21) indicate a source comparatively depleted in fluid-mobile elements (Figure 4.2.11).

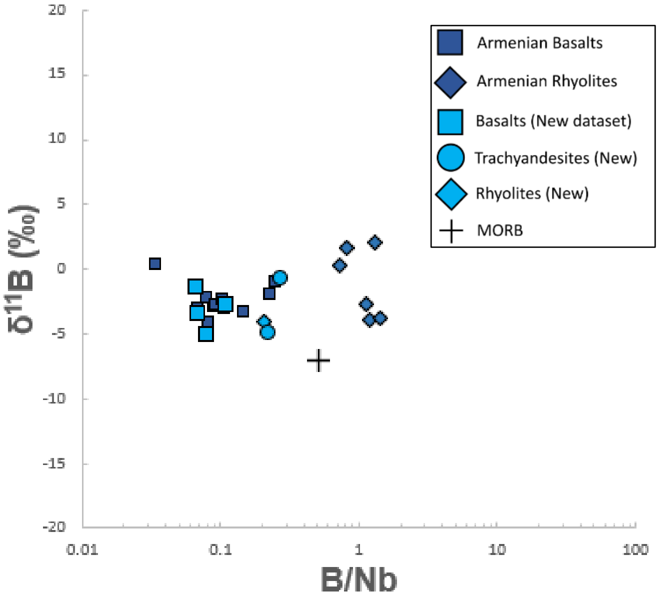

Figure 4.2.11: $\delta^{11}B$ vs B/Nb. B/Nb is an indicator for hydration of the mantle source. B and Nb are equally compatible during melting, but only B preferentially enters aqueous fluids. The low B/Nb ratios of the Armenian volcanics indicate a dehydrated source.

'Armenian Rhyolite' and 'Armenian Basalt' are the pre-existing dataset compiled in Sugden et al. (2020). MORB from Marschall et al. (2017).

Electron Microprobe Analysis (EMPA)

EMPA was carried out on olivines, clinopyroxenes and amphiboles across six samples. These samples were selected via thin section petrography. Olivine was investigated in samples 1.2.19, 3.1.19, 3.4.19, 4.6.19 & 4.7.19; clinopyroxene in 3.1.19, 3.4.19 & 4.7.19; orthopyroxene in 3.1.19 & 3.4.19; and amphibole in 3.1.19 & 4.4.19. For each measured grain, four spots were taken (two in the core and two in the rim). Detailed major oxide analysis was carried out at each spot. Averages were then taken for the cores and rims, giving a final database of two measurements per grain (see Appendix 3). These were analysed for Mg# (Ridolfi et al. (2010)'s method used for amphiboles). Sample wide averages were also calculated (Table 4.2.12).

Table 4.2.12: Electron microprobe analysis results for all six analysed samples, divided by analysed mineral. Each measurement is an average of all grains measured in that sample (n = number of grains averaged). The individual analyses can be found in Appendix 3.

	SiO_2	TiO_2	Al_2O_3	FeO	MnO	MgO	CaO	Na_2O	K_2O	**Total**	**#Mg**
Amphiboles											
3.1.19 core (n=16)	43.89	3.24	11.82	11.81	0.17	14.60	11.60	2.53	1.07	101.59	68.54
3.1.19 rim (n=16)	44.27	3.05	11.46	12.25	0.19	14.52	11.55	2.52	1.09	102.36	67.84
4.4.19 core (n=23)	42.33	3.45	12.69	12.32	0.16	14.20	11.44	2.60	0.95	102.61	67.24
4.4.19 rim (n=23)	42.41	3.54	12.58	12.23	0.16	14.20	11.47	2.55	0.97	102.92	67.41
Olivines											
1.2.19 core (n=9)	40.43	0.02	0.03	15.01	0.26	44.53	0.09	0.00		100.68	83.86
1.2.19 rim (n=9)	40.45	0.02	0.04	15.27	0.45	44.19	0.12	0.01		100.74	83.35
3.4.19 core (n=6)	42.67	0.06	0.25	15.01	0.34	41.86	0.20	0.00		100.59	82.44
3.4.19 rim (n=6)	44.22	0.07	0.27	15.65	0.41	39.72	0.25	0.01		100.77	81.04
4.6.19 core (n=1)	39.44	0.01	0.00	18.22	0.31	41.97	0.08	0.01		100.23	80.15
4.6.19 rim (n=1)	39.17	0.01	0.02	18.47	0.36	41.69	0.08	0.01		99.99	79.78
4.7.19 core (n=8)	38.44	0.02	0.00	23.25	0.80	37.53	0.12	0.00		100.18	73.55
4.7.19 rim (n=8)	38.62	0.03	0.01	23.00	0.82	37.61	0.11	0.00		100.23	73.78
Clinopyroxenes											
3.1.19 core (n=20)	51.89	0.43	2.85	8.29	0.23	15.59	20.90	0.48		100.89	88.71
3.1.19 rim (n=20)	51.85	0.47	2.85	8.58	0.21	15.62	20.81	0.47		101.00	89.49
3.4.19 core (n=20)	51.96	0.69	2.78	7.87	0.23	15.27	21.75	0.51		101.30	77.13
3.4.19 rim (n=20)	51.72	0.72	2.85	8.85	0.27	15.02	21.36	0.52		101.36	74.67
4.7.19 core (n=13)	49.97	1.08	4.99	9.00	0.19	14.89	19.92	0.55		100.91	74.18
4.7.19 rim (n=13)	49.77	1.22	4.47	9.01	0.21	14.36	21.00	0.58		100.82	73.48
Orthopyroxenes											
3.1.19 core (n=12)	54.08	0.17	1.16	16.41	0.62	26.36	0.62	0.01		99.49	73.34
3.1.19 rim (n=12)	54.34	0.19	1.26	15.01	0.50	27.29	0.69	0.01		99.37	75.78

The observed olivines were commonly found as phenocrysts in the more mafic samples, but they are also prevalent in the groundmass. No clear zoning was visible under light microscope, but on rare occasions zonation was observed under SEM. The observed olivines mostly have a massive, rounded habit (Figure 4.2.13). Inclusions were common and some olivines exhibited alteration to clays. The olivine crystals that underwent EMPA displayed a predominantly forsterite composition. They also showed varying types of zonation on the basis of Mg#. Grains with normal and reverse zoning, as well as many grains without clear zonation, were found in all samples.

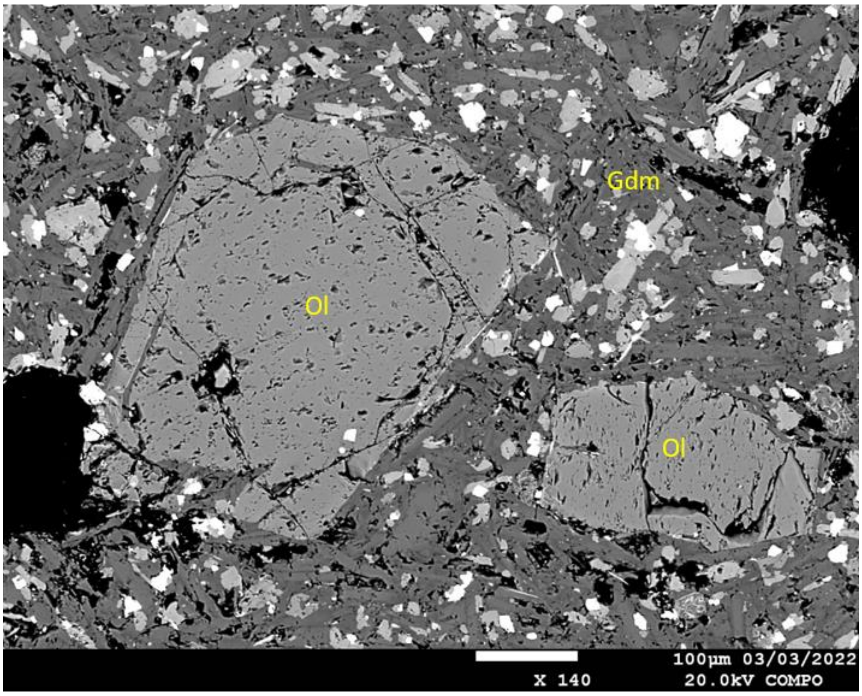

Figure 4.2.13: SEM image of two olivine phenocrysts in sample 1.2.19. The crystals have massive habits and contain many inclusions.

The clinopyroxenes commonly occurred as phenocrysts in samples across the compositional spectrum. When viewed under SEM, zonation was observed rarely. Clinopyroxenes were observed in a variety of habits, both euhedral and anhedral. The analysed clinopyroxenes were of an augite ($(Ca,Mg,Fe)_2Si_2O_6$) composition (Morimoto et al., 1988). As with the olivines, there was no clear pattern of zonation across the samples, with evidence of both normal and reverse zoning present in all samples.

Amphiboles generally were found to have a euhedral habit, with well-defined crystal shape (Figure 4.1.4c). They almost always had large reaction rims, and sometimes were found as fully reacted remnants. There are several instances of amphiboles found in a sub-ophitic texture with plagioclase, with the crystal face enclosed by the plagioclase resisting any alteration (Figure 4.1.4a). There was no clear visible zonation in the observed amphiboles. Using Ridolfi (2010)'s method, the amphiboles that underwent EMPA were identified to be magnesiohastingsites. The amphiboles show a variety of zoning types on the basis of Mg#, with no clear pattern constrained to each sample.

5. Discussion

5.1 Crustal Contamination

When looking at the distinct geochemical signatures of the rocks from Vardenis (and the wider Lesser Caucasus), it is important to first examine the potential role of crustal contamination, to ensure that features initially attributed to the mantle source are not obscured or induced by this late-stage process (Hawkesworth & Vollmer, 1979; Keskin et al., 2006).

The continental crust in the SLC is composed of metamorphic basement rocks, Mesozoic-Cenozoic sediments and Mesozoic arc volcanics (Mederer et al., 2013). Aside from the arc volcanics, the assimilation of the crustal rock by ascending post-collisional melts would create a notable deviation in the geochemical data, especially in Sr and Nd isotope ratios.

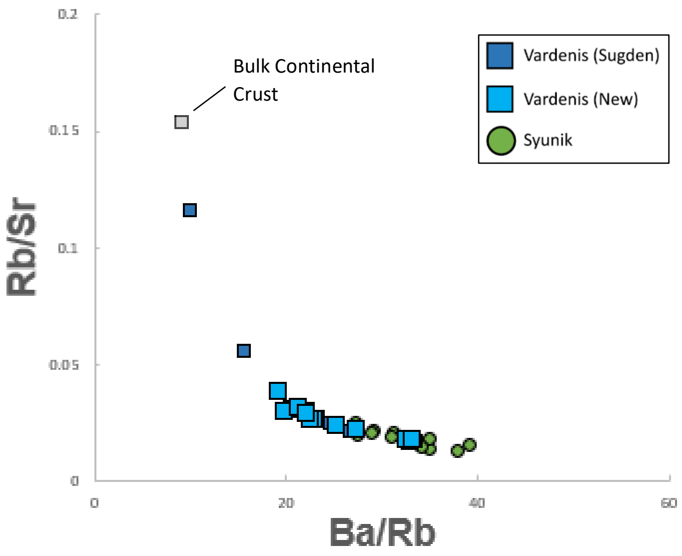

Figure 5.1.1: Rb/Sr vs Ba/Rb. The majority of SLC samples show a comparative depletion in Rb and enrichments in Sr and Ba.

Bulk Continental Crust data from Rudnick & Gao (2003); Vardenis (Sugden) and Syunik from Sugden et al. (2019).

In Vardenis this is not the case. Firstly, the trace element data does not suggest that crustal contamination is prevalent. All samples from the new dataset have very low Rb/Sr (<0.05), which is not indicative of crustal input, as continental crust is comparatively enriched in Rb and depleted in Sr (See Figure 5.1.1). Furthermore, there is very little variability in $^{87}Sr/^{86}Sr$ or $^{143}Nd/^{144}Nd$ when plotted against SiO_2 (Figure 5.1.2), indicating that crustal contamination is unlikely to have occurred. If continental crust had been assimilated, there would be large deviations from the average in the more evolved samples observed across both isotopes. The more evolved samples would display these anomalies as the contaminants inherently enrich the melt in SiO_2, such as in Eastern Anatolia, where crustal assimilation induced $^{87}Sr/^{86}Sr$ values of up to 0.7065 (Pearce et al., 1990). There is a slight $^{87}Sr/^{86}Sr$ enrichment in the most evolved Vardenis sample, but this is not considered to be significant. Sugden et al. (2019) attributed a similar $^{87}Sr/^{86}Sr$ spike in rhyolites from Syunik to Rb source enrichment and their subsequent post-crystallisation decay (see Figure 5.1.2). There is risk that crustal contamination via antecedent arc volcanics has occurred – these metrics cannot prove this one way or the other. The presence of quartz xenocrysts identified in the petrography do suggest some contamination, but they are very rare and thus their impact on the geochemistry is negligible. Therefore, it is most likely that crustal contamination has simply not played a major role in the Vardenis post-collisional melts.

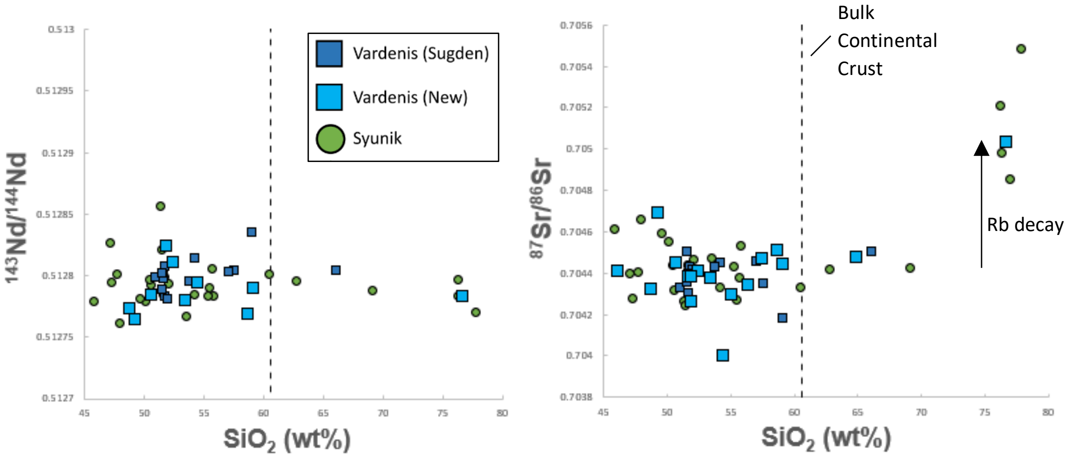

Figures 5.1.2: Isotope ratio vs SiO_2 for all analysed post-collisional samples from Vardenis and Syunik. Arrow displaying displacement attributed to post-crystallisation decay of Rb in the most evolved samples. This alteration is clearly not caused by assimilation of either the Southern Armenian Block basement ($^{87}Sr/^{86}Sr$ = ~0.7303) (Baghdasaryan and Ghukasyan, 1985) or of Tethyan sediments (Tethyan Flysch from Prelević et al. (2008) has an $^{87}Sr/^{86}Sr$ of 0.7112).

Syunik and 'Vardenis (Sugden)' data from Sugden et al. (2019). Bulk Continental Crust (SiO_2 = 60.6wt%) from Rudnick & Gao (2003).

This is concurrent with the MgO and P_2O_5 Harker diagrams, in which the samples from Vardenis show clear, smooth trends with increasing SiO_2 (see Figure 4.2.4). This is a further indicator that the evolved suite of volcanics in the Lesser Caucasus was generated by fractional crystallisation during emplacement and storage, as opposed to by assimilation of crustal material.

5.2 The origin of the subduction signature

As crustal contamination has been determined not to have played a role in Vardenis, we can assume that it has also not impacted the Boron (B) systematics of the sample suite. There has also been no physical evidence of any kind for the presence of xenoliths. As a result, analysis of B is the main method used in this study to interrogate the origin of the subduction signature observed in the trace element profiles.

The newly collected data suite from Vardenis has [B] abundances ranging from 1.4 to 7.2ppm and δ^{11}B of -5.1 to -0.75‰. This δ^{11}B data agrees well with the Syunik and (limited) Vardenis samples reported in Sugden et al. (2020), as well as with the δ^{11}B ratios reported by Sokół et al. (2018) for the Tezhsar Alkaline Complex (TAC) (an Eocene-age volcanic complex in northern Armenia). The new Vardenis data further supports the conclusion that the subduction signature has been consistent since at least 41Myrs ago (the age of the TAC) when subduction was still active.

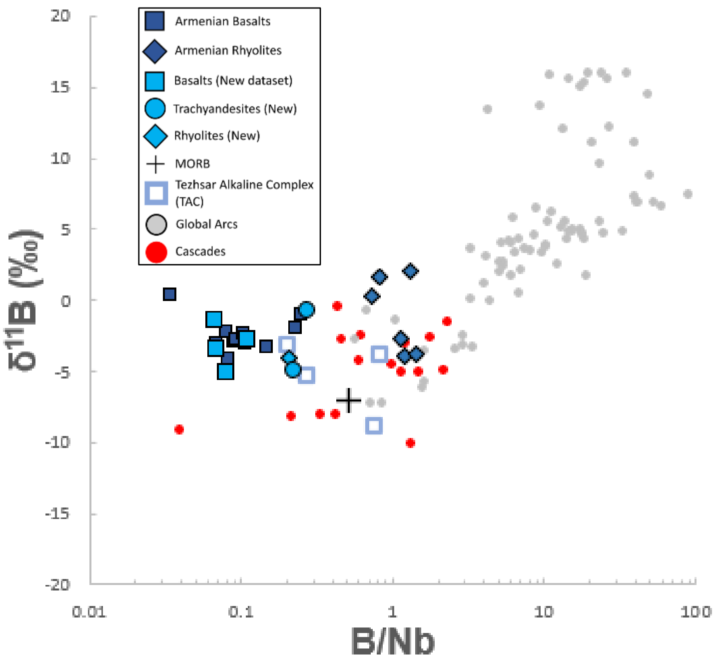

Figure 5.2.1: δ^{11}B vs B/Nb. Both the pre-existing and new dataset from Armenia forms a mostly distinct reservoir from other global arcs. Instead, they have a low B/Nb ratio, indicating dehydration. They share this feature with the Cascades: a hot, fluid-depleted arc system.

'Armenian Basalt' and 'Armenian Rhyolite' includes data from Vardenis (Sugden et al., 2020), Syunik (Sugden et al., 2020) and NPP (Connor et al., 2011). Global Arcs data from De Hoog & Savov (2018); Cascades data from Leeman et al. (2004). MORB from Marschall et al. (2017). TAC data from Sokół et al. (2018).

Compared to MORB (-7.5‰; Marschall et al., 2017), the new Vardenis suite is somewhat enriched in boron and has a slightly heavier δ^{11}B ratio. This shows that the metasomatising agents (melts or fluids) released during subduction dehydration of the slab have in some way altered the overlying mantle wedge. However, most arcs are created in H_2O-saturated environment (Gaetani & Grove, 1998), with B/Nb ratios well above 1. The Vardenis (and wider SLC) dataset oppose this trend, forming a distinct reservoir with low B/Nb indicative of a fluid-depleted source, similar to that of the Cascades (a hot, dehydrated arc system (Leeman et al., 2004)) (Figure 5.2.1). This post-metasomatic dehydration has led to the depletion in B, and the decrease of the δ^{11}B ratio, relative to the typical volcanic arc fronts (DeHoog and Savov, 2018), but also explains the remaining relative B enrichment and slightly heavier δ^{11}B ratios in respect to MORB.

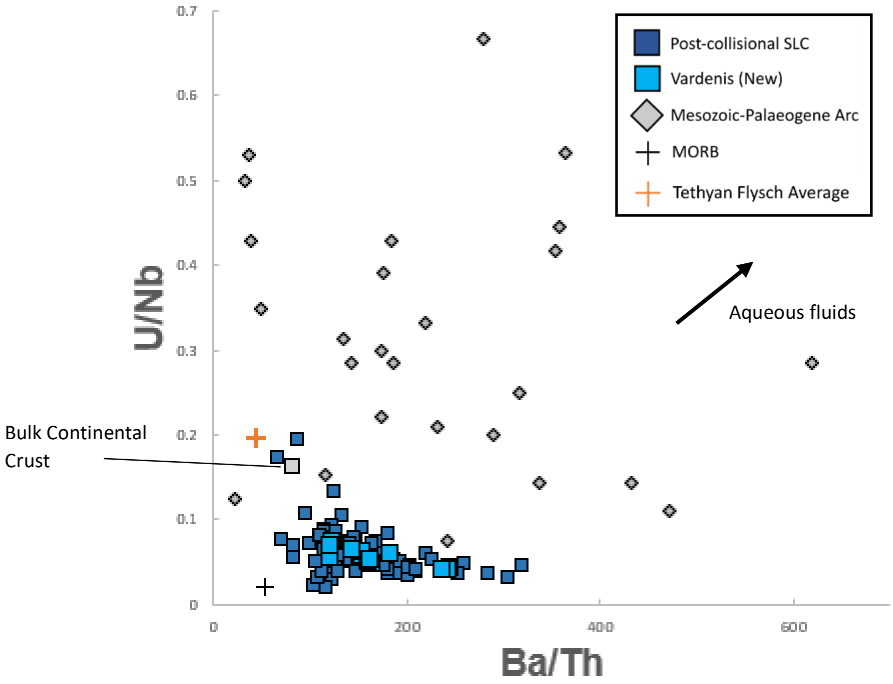

Figure 5.2.2: U/Nb vs. Ba/Th diagram for Mesozoic to Modern collision-related mafic volcanic arc rocks. U, Ba, Nb and Th all have a similar compatibility during melting, so would show no variation from MORB if only melting had occurred. U and Ba are fluid-mobile, whilst Nb and Th are fluid-immobile. Increases in U/Nb and Ba/Th indicate the influence of aqueous fluids (Plank & Langmuir, 1998).

'Post-collisional SLC' includes data from Syunik and Vardenis (Sugden et al., 2019), Gegham (Savov, *unpublished*), Shirak & Lori (Neill et al., 2015) and Aragats (Connor et al., 2011). 'Mesozoic-Paleogene Arc' data from Aydinçakir & Sen (2013). MORB data from Sun & McDonough (1989); Bulk Continental from Rudnick & Gao (2003) and Tethyan Flysch average calculated from Prelević et al. (2008).

In arc settings, the aqueous fluids are commonly the metasomatising agent produced by subduction (Yoshikawa et al., 2016), but it is also possible for it to be a melt or supercritical fluid (MSF) (Kessel et al., 2005). Aqueous fluids interacted with the SLC mantle source in some capacity, as indicated by the slightly raised Ba/Th and U/Nb ratios relative to MORB (Figure 5.2.2). If mixing between an aqueous fluid (for which altered oceanic crust (AOC) is a proxy) and MORB was responsible for the metasomatism, the Sr-B and Nd-B would be expected to fall on a mixing line between AOC (rich in high [B] and heavy δ^{11}B fluids from subduction dehydration) and MORB (or depleted MORB mantle (DMM)) (see Figure 5.1.4). However, the SLC suite (including the new Vardenis data) has significantly lower ^{143}Nd/^{144}Nd values than expected (Figure 5.2.3). This dismisses aqueous fluids as a possible metasomatising agent, meaning that they were likely a transitory component.

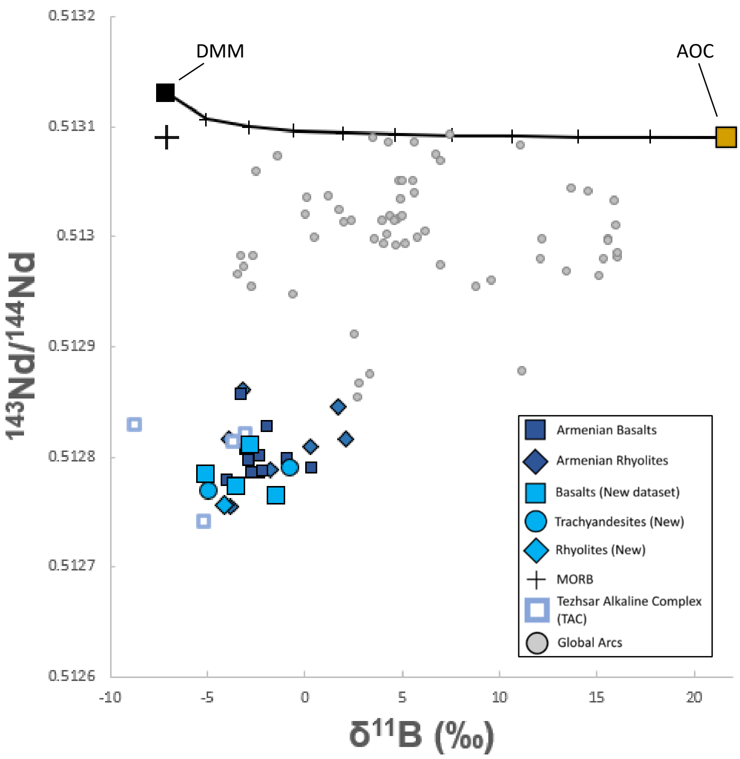

Figure 5.2.3: ^{143}Nd/^{144}Nd vs δ^{11}B. The Post-collisional dataset from Southern Armenia (both the new data and from Sugden et al. (2020)) show a distinct reservoir, with markedly lower ^{143}Nd/^{144}Nd values than other global arcs (De Hoog and Savov, 2018), MORB (Marschall et al., 2017) and the expected values from a mixing line between depleted MORB mantle (DMM) and altered oceanic crust (AOC).

Mixing line data: DMM values from Workman & Hart (2005) and Marschall et al. (2017). AOC values from McCaig et al. (2018), Marschall et al. (2017) and Sun & McDonough (1989).

This means that the metasomatic alteration was imparted by a melt or supercritical fluid originating from either altered (and thus hydrated) Tethys oceanic crust or subducted sediment. Oceanic MSFs are characteristic of adakites, which typically have MORB-like Sr-Nd isotope data, as well as lower Y and Yb values than the SLC (Castillo, 2012). Thus, the metasomatising agent must have been a sediment-derived MSF, which is reinforced by the low ^{143}Nd/^{144}Nd values of the new VVH dataset. Furthermore, there is a similarity in the Th/Rb of the SLC suite and of Tethyan Flysch reported in Prelević et al. (2008) (Figure 5.2.4). Th is a fluid-immobile element, so in order for the subducted Tethyan flysch sediments to have imparted its Th signature onto the overlying mantle, a sediment melt must have been involved (Plank & Langmuir, 1993). The exact origin of the sediment melt that fed the subduction alteration under the SLC is a subject that warrants further investigation. As δ^{11}B is unaffected by the high T processes of melt generation, the sediment source must have a ratio similar to that transferred to the mantle. Sugden et al. (2020) hypothesise that metasediments from Syros, Greece have a δ^{11}B ratio (-1.6 to + 0.9‰ (Marschall et al., 2008)) compatible with this theory, and therefore can be used as a proxy for the sediments subducted in Armenia. The new dataset complies largely with this theory, although, its δ^{11}B values extend to even lighter extremes (-5.1‰), indicating that the rocks at Syros are not an exact match.

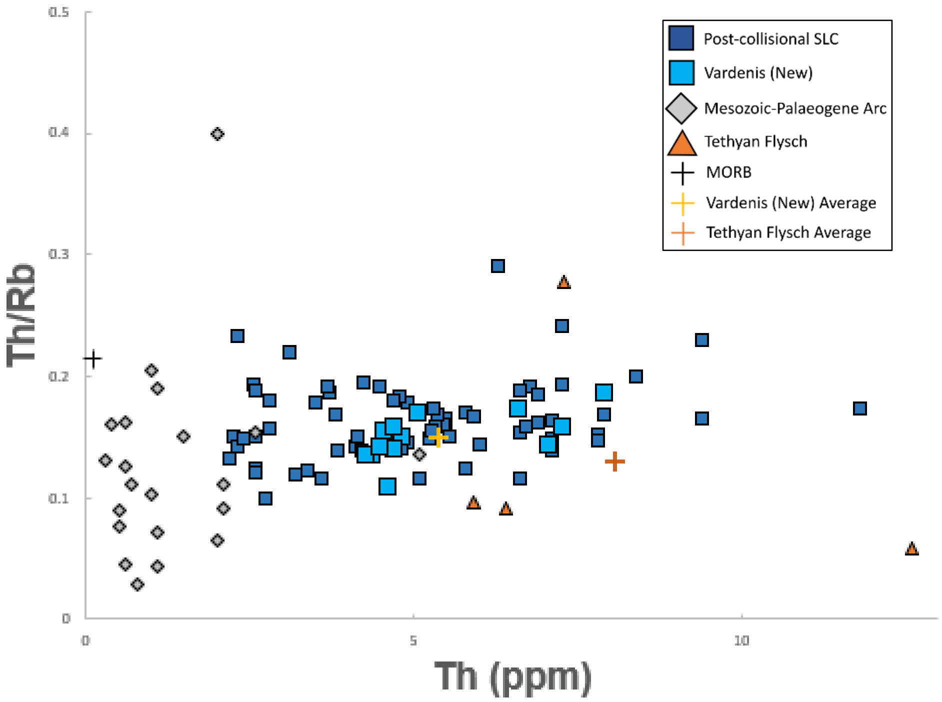

Figure 5.2.4: Th/Rb vs Th. The Armenian volcanics (both old and new datasets) show a marked enrichment in Th compared to other global arcs and MORB. The averages for the new Vardenis dataset and the Tethyan Flysch can be seen to have very similar Th/Rb ratios (0.15 and 0.13 respectively), suggesting the incorporation of a sediment melt, potentially of Tethyan Flysch origin.

Data is sourced and filtered in the manner as in Fig. 5.2.2. Tethyan Flysch data from Prelević et al. (2008). MORB from Sun and McDonough (1989).

The preservation of this signature in the mantle since the Eocene alludes to a mineral phase that can serve as a repository for the boron. Such minerals should be able to host the subduction signature for a long time, through subsequent dehydration and alteration, then release its δ^{11}B signature during melting in a post-collisional setting. Such repositories are metasomatic minerals that are stable in the lithospheric mantle, most commonly amphibole or phlogopite (Mandler & Grove, 2016). The new Vardenis dataset displays high Ba/Rb (19-33 in mafic samples) and low Rb/Sr (0.01-0.03) (Figure 5.1.1). Rb is an order of magnitude less compatible in amphibole than it is phlogopite (LaTourrette et al., 1995). Thus, these ratios suggest that amphibole is the repository mineral. Furthermore, the relatively low [B] (~1-7ppm) of the new Vardenis suite (compared to other global arcs ~12ppm; De Hoog and Savov, 2018) also suggests an amphibole source for the subduction component. Amphibole has a low B partition coefficient (Brenan et al., 1998), and thus does not preserve much B when stabilising. This low [B] pattern was also observed by Tomanikova et al. (2019) in the amphibole veins of Kamchatka arc mantle xenoliths and could contribute to the low [B] nature of the post-collisional melts in the SLC.

Finally, the Dy/Dy* and Ti/Ti* ratios indicate preferential partitioning in the SLC samples (Davidson et al. (2013); Figure 5.2.5). All of these features point towards amphibole as the repository mineral for the subduction component, supporting the conclusions made in Sugden et al. (2020).

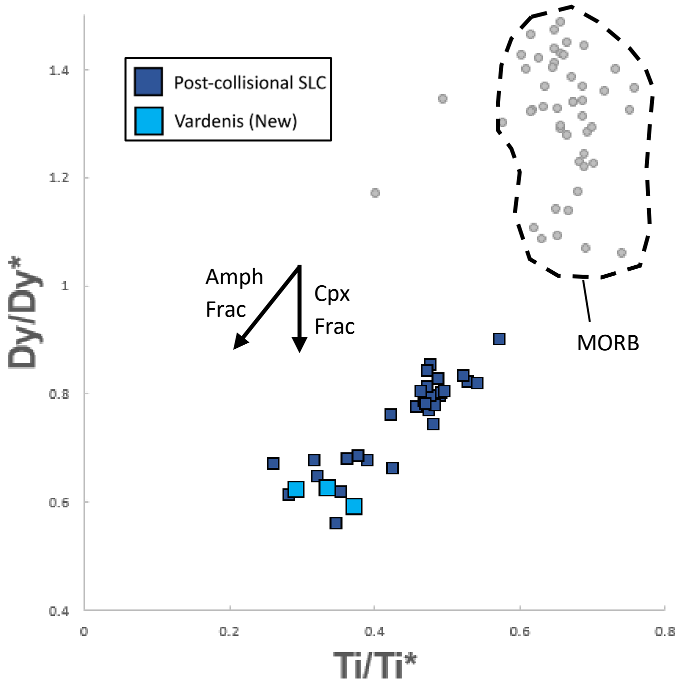

Figures 5.2.5: Dy/Dy* vs Ti/Ti*. Only amphibole preferentially partitions both Dy and Ti (in contrast to clinopyroxene which only partitions Dy). Thus, a decrease in both Dy/Dy* and Ti/Ti* is indicative of amphibole fractionation (Davidson et al., 2013). MORB field also shown (adapted from Davidson et al. (2013) and references therein) to the high right of the graph, showing that there has been no amphibole fractionation.

Only basalts used. 'Post-Collisional SLC' comprised of data from Sugden et al. (2019) and Neill et al. (2015). Both metrics are comparisons between the observed and expected values (expected are calculated by interpolating from other known trace elements).

Sugden et al. (2019) also discussed the role of apatite ($Ca_5(PO_4)_3(F,Cl,OH)$) in the Lesser Caucasus – another metasomatic mineral observed in Syunik (and NW Iran). These most SE regions show LREE enrichments (high $La/Yb_{(CN)}$ and Sr/Y) (Figure 5.2.6a&b), in line with the generally observed enrichments suggested to occur towards the SE (Sugden et al., 2019). However, these enrichments correlate clearly with an increasing P_2O_5 (Figure 5.2.6c&d), suggesting the presence of apatite as a metasomatic mineral, which is at odds with the previously determined amphibole-based metasomatism. The new Vardenis dataset did not display any apatite during petrography and does not show the same extreme level of P_2O_5 enrichment as the Syunik and NW Iran suites, but there is still overlap in the geochemical suites, and a clear trend of P_2O_5 enrichment from NW-SE across the LC. Thus, the geographical variations of apatite in the Lesser Caucasus should be further investigated.

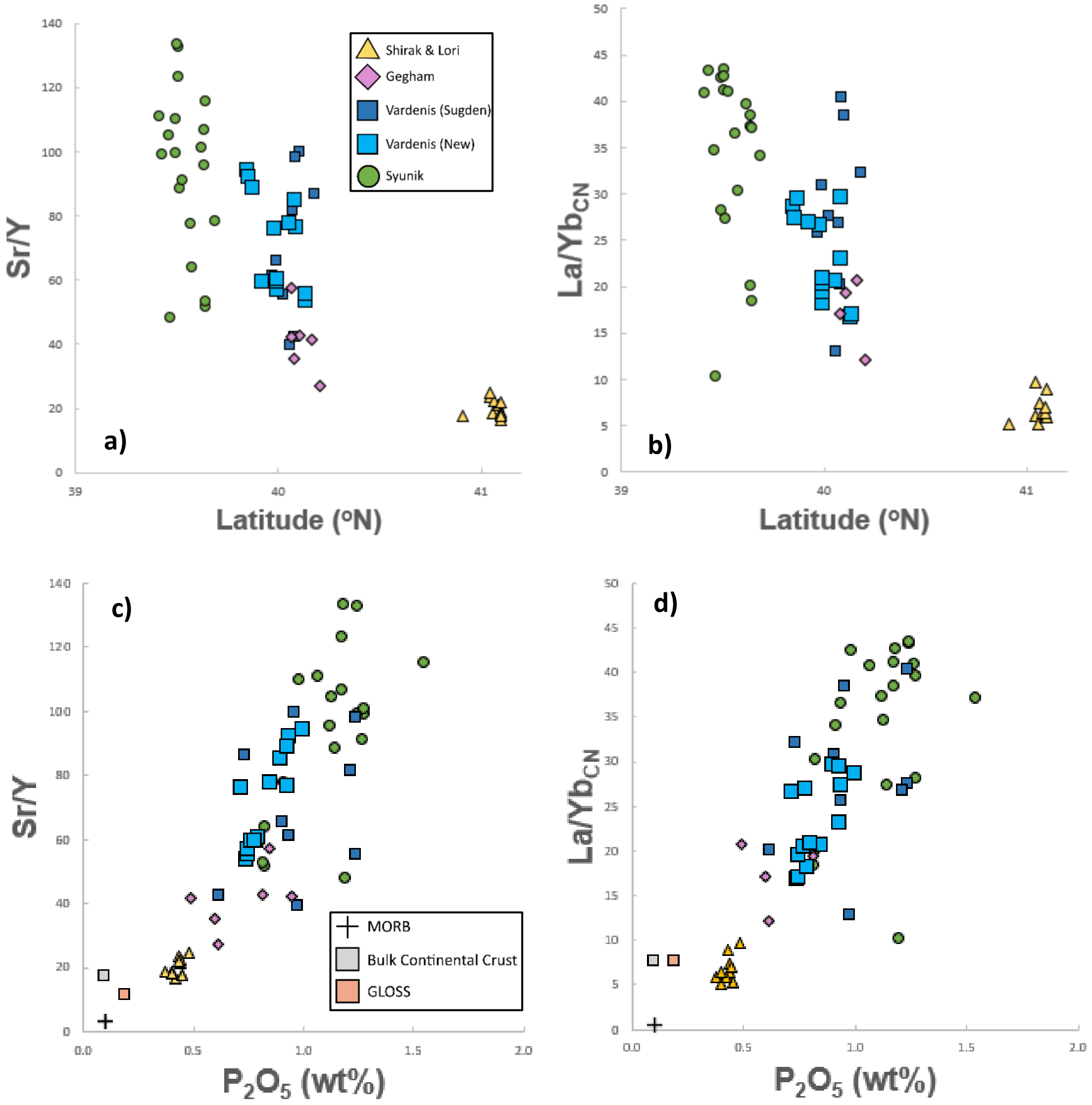

Figure 5.2.6: a & b) The variation of Sr/Y and La/Yb (chondrite normalised) across the Lesser Caucasus. There is clearly lots of overlap between the Vardenis and Syunik data sets, but the Syunik suite extends to higher levels for both ratios. **c & d)** The increases in both ratios correlate with increasing P_2O_5 enrichment, suggesting the influence of apatite.

Shirak & Lori data from Neill et al. (2015); Gegham from Savov (unpublished); 'Vardenis (Sugden)' and Syunik from Sugden et al. (2019). MORB from Sun & McDonough (1989) and Sun et al. (1979). Bulk Continental Crust from Rudnick & Gao (2003). GLOSS (Global Subducting Sediment) average from Plank & Langmuir (1998).

In summary, the mantle source was altered by a sediment melt derived from subducted Neotethyan material. This subduction signature was preserved in metasomatic amphiboles, allowing it to remain in the lithospheric mantle for at least 41Myrs, during which time the source material was dehydrated and largely stripped of elemental boron. Post-collisional melting created magmas with this preserved signature, which have since been erupted, seemingly without crustal contamination.

5.3 Potential for a shared source for the Vardenis and Syunik Volcanic Highlands (VVH and SVH)

In much of the prior research on the SLC, the Vardenis and Syunik volcanic highlands have been considered as distinct, unrelated magmatic systems with different sources (Sugden et al., 2019). The geochemistry of the new VVH dataset challenges this theory, and thus the transition between the two highlands needs to be further investigated to establish if/how they are related.

Sugden et al. (2019) considered this relationship in their interrogation of trends across the Lesser Caucasus (from Shirak & Lori in the NW to Syunik in the SE). Several trends became apparent. Firstly, in the trace element profiles (Figure 4.2.6), which displayed progressively more pronounced subduction-related anomalies moving from NW-SE. This is echoed in the radiogenic Sr-Nd isotopes for the region, which display a clear enrichment (increasing $^{87}Sr/^{86}Sr$ and decreasing εNd) from NW-SE, with each highland creating a distinct field (Figure 4.2.9). With this evidence, Sugden et al. (2019) concluded that the mantle sources did vary between these volcanically active highlands.

The new Vardenis dataset presented here does not fit the isotope trend on mantle enrichment as suggested by Sugden et al. (2019), bucking the trend of increasing enrichment expected between VVH and SVH. With some of the lowest εNd values recorded in the SLC, the new suite can be considered enriched to a similar level as the one characteristic for the Syunik.

5.4 Examination of the shared mantle source theory

A Vardenis-Syunik reservoir can be identified in the Sr-Nd isotope systematics (Figure 5.4.1). However, a wider examination of the datasets is required to confidently say that these two highlands share a distinct magma reservoir.

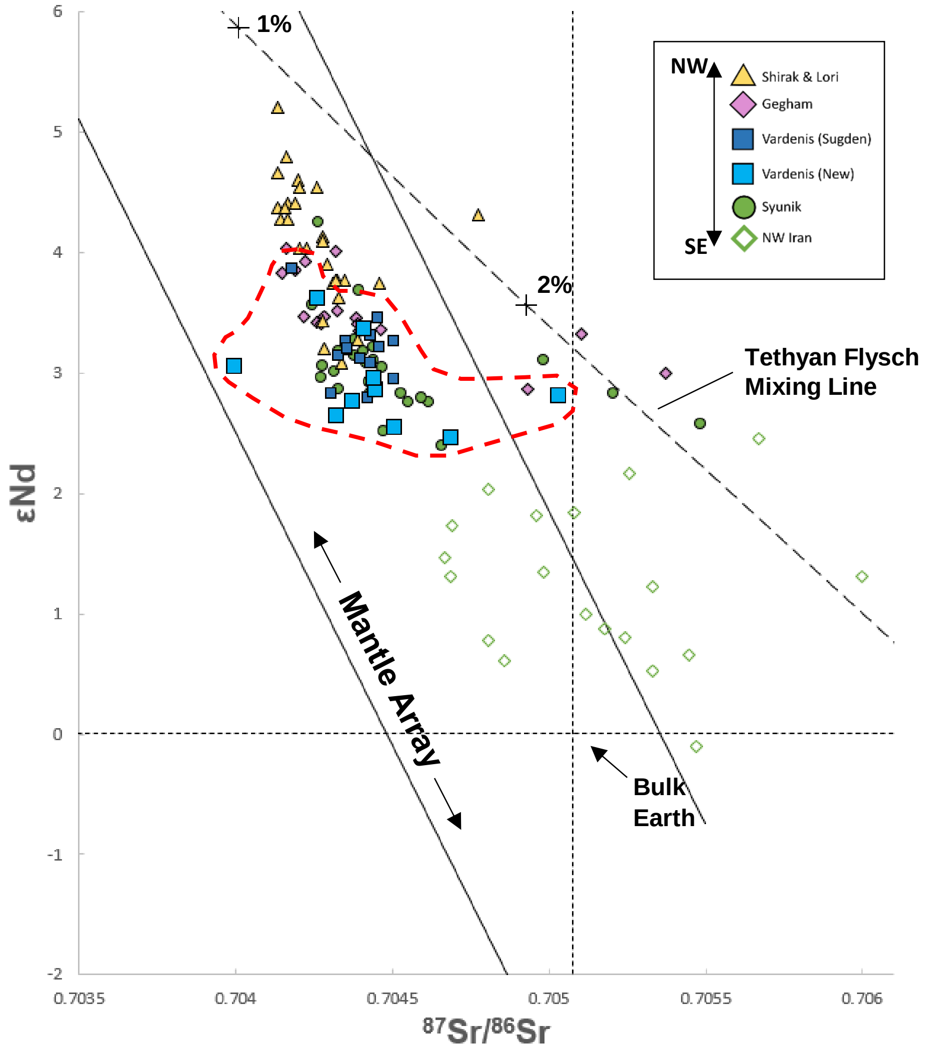

Figure 5.4.1: εNd vs $^{87}Sr/^{86}Sr$. Outlined in the dashed red line is the hypothesised Vardenis-Syunik shared mantle source, which marks the enriched endmember for the SLC.

See Fig. 4.2.9 for data sources and filtering.

When the B isotopes are considered, data from Vardenis (both the new dataset and Sugden et al. (2020)'s data) and Syunik combine to make a reservoir distinct from other global arcs. There is some overlap with the TAC (also from Armenia) and the Cascades (another hot, fluid-depleted arc), but generally a distinct grouping is observed (Figures 5.4.2). The combined SLC dataset forms a unique reservoir with a pre-conditioned mantle source. The subduction signature (imparted by a sediment melt) is preserved for millions of years, and then incorporated into a new melting regime. This Vardenis-Syunik reservoir could be applied to other volcanic regions with reworked mantle sources.

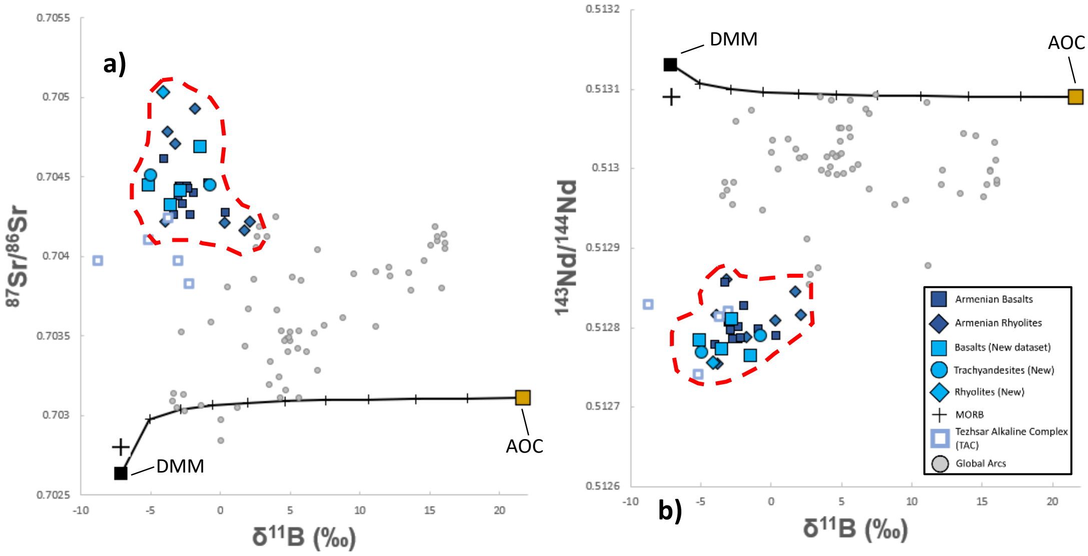

Figure 5.4.2: a) $^{87}Sr/^{86}Sr$ vs $\delta^{11}B$. **b)** $^{143}Nd/^{144}Nd$ vs $\delta^{11}B$. Circled in dashed red line - Vardenis-Syunik reservoir in Sr-Nd-B space (compiled from the new Vardenis dataset and from Sugden et al. (2020)). Clearly distinct from other global arcs (De Hoog and Savov, 2018) and from MORB (Marschall et al. (2017) and White and Hofmann (1982)). Related to but still distinct from the TAC dataset (Sokół et al., 2018). DMM-AOC mixing line data as in Figure 5.2.3, with the addition of Staudigel et al. (1995).

Furthermore, based on this study and on Sugden et al. (2019), the petrography of the two highlands has many similarities. Olivine, clinopyroxene, plagioclase and oxides are commonplace in both as phenocrysts, glomerocrysts and in the groundmass. There are no significant or pervasive differences in groundmass textures. Amphibole phenocrysts are another shared feature in many samples, as well as K feldspar in the most evolved samples. However, the regions do have petrographic differences. Both the new and old Vardenis suites showed biotite/phlogopite, whilst Syunik did not have this. Meanwhile Syunik hosts apatite, a mineral not observed in the Vardenis petrography. The petrography is not so similar that one can definitively declare them as from the same reservoir, but not so different as to say they have no relation.

The major and trace element data holds the main argument against Vardenis and Syunik sharing a mantle source. Whilst sharing a very similar compositional range of samples, the Syunik dataset is generally more alkaline (Figure 2.2.2). There are also clear differences in the trace element profiles, indicating a potential variation in the proportion of the subducted component present in the source material of the most mafic samples (Figure 5.4.3). However, metrics such as alkalinity and trace element profile (especially REE) are sensitive to degree of melting and storage modifications. They are not as reliable indicators as isotope ratios, which reflect the source (as long as there has been no crustal contamination) (White, 1995).

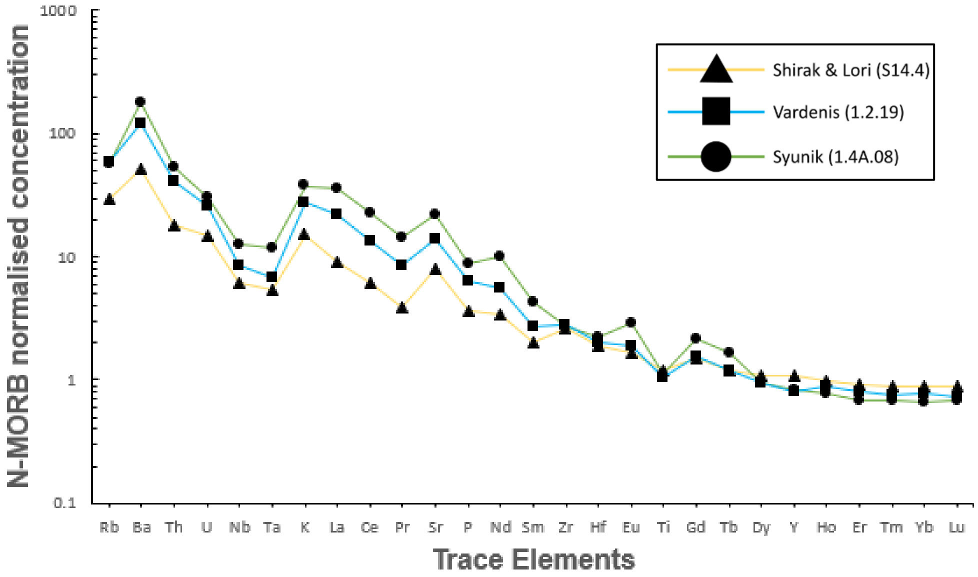

Figure 5.4.3: Comparison of the N-MORB normalised trace element profiles of the most mafic (highest MgO wt%) sample from Shirak & Lori (Neill et al., 2015), Vardenis (this study) and Syunik (Sugden et al., 2019). This graph shows that the subduction component varies across the Lesser Caucasus, more importantly between Vardenis and Syunik. Syunik has a more pronounced subduction signature (steeper line with more pronounced enrichments (e.g. Ba) and depletions (e.g. Ti)), suggesting that there is a higher proportion of the subducted component in the most primitive magmas produced there than those produced in Vardenis

In most examinations of trace element relationships, there is almost always overlap between the Vardenis and Syunik datasets, but Syunik always extends to greater extremes (Figure 5.2.6a&b). This is evident in the aforementioned investigation of apatite's role in the Vardenis-Syunik system. The Sr/Y values for Vardenis (both old and new) completely overlap with the Syunik dataset, but Syunik has a much wider spread, reaching far more enriched levels. These more enriched samples correlate to the presence of apatite (increased P_2O_5) levels. This suggests that there may be a secondary source in Syunik that is rich in apatite and contributes these more enriched samples. The shared Syunik-Vardenis mantle source may well exist, but not alone, making the comparison between the two volcanic highlands even more complex.

With such conflicting evidence, it is hard to conclude as to whether there is a shared mantle reservoir or not, and to how pervasive the role of this reservoir would be across the Vardenis and Syunik highlands. This is a topic that requires further investigation and would be greatly helped by the continued expansion of the SLC database.

5.5 Depth and Temperature of the mantle source (Geothermobarometric calculations)

From the data collected via EMPA of amphiboles, the pressure and temperature of amphibole crystallisation can be determined utilising Ridolfi et al. (2010)'s method shown in Sugden (2021). Temperature ranges from 946-986°C and pressure from 300-409MPa, which translates to 10.7-

14.6km depth (Table 5.5.1) (calculated by assuming a constant density profile of 2.8 gcm^{-3}, adapted from Sugden (2021)).

Table 5.5.1: Data post-geothermobarometric calculations for amphiboles in samples that underwent EMPA. See Appendix 4 for the original data.

	Pressure Average (MPa)	Pressure range (MPa)	**Temperature Average (°C)**	Temperature Range (°C)	Depth (km)	Depth Range (km)
3.1.19 core	**329**	232-425	**959**	917-996	11.8	8.3-15.2
3.1.19 rim	**300**	240-376	**946**	917-977	10.7	8.6-13.4
4.4.19 core	**409**	317-454	**986**	950-1011	14.6	11.3-16.2
4.4.19 rim	**398**	349-454	**984**	943-1008	14.2	12.5-16.2

Table 5.4.1 continued

	H_2O_{melt} at the source (wt%)	H_2O_{melt} range (wt%)	Average pressure uncertainty (σ_{est})	Average temperature uncertainty (σ_{est})	Average H_2O_{melt} uncertainty (σ_{est})
3.1.19 core	4.2	3.5-5.2	36	22	0.6
3.1.19 rim	4.0	3.4-5.1	33	22	0.6
4.4.19 core	4.7	4.2-5.3	45	22	0.7
4.4.19 rim	4.7	3.8-6.3	44	22	0.7

In comparison to Sugden (2021)'s pressure estimations for the adjacent Syunik volcanic highland (723-887MPa), the new dataset plots at a much lower pressure, with the averages around 400MPa lower. The temperature values are similar to that of the Syunik database (981-1013°C), whilst the H_2O_{melt} figures are also lower than Sugden's values (5.6-8wt%). Another comparison can be drawn to the Aragats region (NW of Vardenis and Syunik). With temperatures of up to 1224°C and H_2O_{melt} of 0-1.7wt% (Connor et al., 2011), this region represents a geothermal anomaly that generates exceptionally hot and dry magmas. Whilst the magmas of the SLC are generally high T and dehydrated, it is not to the same extent as in Aragats, signifying that Vardenis and Syunik likely form a separate magmatic system.

Sugden et al. (2019) determined the depth of the crust under the Syunik to be 60km, using Hu et al. (2017)'s method involving Sr/Y and La/Yb$_{(CN)}$ ratios. Meanwhile, the SLC lithosphere-asthenosphere boundary is thought to be at >100km depth (Priestley et al., 2012).

The new Vardenis dataset suggests that the crystallisation of amphibole occurs at a much shallower depth on average in Vardenis than in Syunik (10-15km as opposed to 15-40km (Sugden 2021)). It also shows a much more restricted range of values when it comes to the pressure and temperature of melting. This suggests strongly that Vardenis is fed by a single reservoir of melt that stalled at shallow depths, and thus likely also a single mantle source. In contrast, Syunik's wide range of P-T conditions lends more credence to the possibility of more than one magmatic reservoir (and source), with the lower P values potentially sharing a source with the system of Vardenis.

This is all in line with Sugden et al. (2019)'s final holistic model, which suggests two different mantle sources under the SLC – one at the lithosphere's base and the other mid-lithosphere. I hypothesise that the mixing of the two generated a shared source for Syunik and Vardenis that stalled at shallow depths of the crust and underwent fractional crystallisation there before being erupted across Vardenis and part of Syunik. It is likely that another mantle source feeds Syunik, fed only by the apatite-rich, mid lithospheric source that also feeds NW Iran (Pang et al., 2013), which creates the wide range of P-T conditions observed in Sugden (2021).

This is a topic that needs much further investigation, especially with regard to expanding the database. These hypotheses are unfortunately based on small databases. The continued development of our records on Vardenis is vital to understanding the complex magmatic system of Southern Armenia.

6. Summary and Closing Remarks

6.1 Summary

The Vardenis Volcanic Highland is home to the most recent Armenian volcanic activity (Porak circa 3,000yrs ago) and over 100 volcanoes. The new dataset presented here includes petrological and geochemical analysis of 26 samples from across the region. The dataset displays a wide compositional range (basanite to rhyolite), but shows uniformity in high K_2O values and in a ubiquitous subduction signature. The latter of these is observed widely across the rest of the Armenian Lesser Caucasus (Shirak & Lori, Gegham and Syunik volcanic highlands). The contribution of this subduction signature to the generally intraplate type volcanism in Armenia varies across the region, with the signature becoming more distinct from NW to SE. Crustal contamination has been shown to not play a major role in Vardenis, as the Sr and Nd isotope ratios ($^{87}Sr/^{86}Sr = 0.703993-0.705029$; $^{143}Nd/^{144}Nd = 0.512764-0.512823$) do not vary significantly with increasing SiO_2 (this would be expected if the magma had been contaminated by the metamorphic and sedimentary antecedent rocks of the region). This is further corroborated by other key elemental concentrations (such as MgO vs SiO_2), which display trends indicative of magma differentiation.

Via B analysis, the subduction signature ($\delta^{11}B$ = -0.75 to -5.1‰) has been determined to have been imparted to the mantle during metasomatism by a sediment melt. The signature has been consistent for at least 41Myrs (around the time the Neotethys Ocean closed), and the sediment origin has been linked to metamorphosed Tethyan sediments through similarities in the $\delta^{11}B$ values. Despite this metasomatic subduction signal, the Vardenis samples are now relatively depleted in boron ([B] = 1.44-7.17ppm), indicating that the mantle source has been dehydrated. It has been determined that the subduction signature (specifically the $\delta^{11}B$ ratio) was imparted to the overlying mantle by the sediment melt and preserved in a repository mineral, in this case amphibole. After this, the source was dehydrated, leaving very little boron. When mantle melting occurred, the amphiboles released the preserved boron, giving the boron-poor magmas of Vardenis a Neotethyan subduction signature. All of these observations and conclusions were in line with those made by Sugden et al. (2020), who's work focused on the SVH – the southernmost region of the Armenian Lesser Caucasus.

When the new Vardenis dataset is combined with Sugden et al. (2020)'s isotopic data for the SLC, a distinct reservoir in Sr-Nd-B systematics can be highlighted (Figure 5.4.2), separate from MORB and other global arcs. This dataset reveals that subduction modification can produce signatures that are preserved in the mantle for millions of years to come and become incorporated into more recent volcanism. This unique reservoir is indicative of arc settings with unclear source origins or where single/multi-phase mantle source reworking is occurring.

Whilst the adjacent volcanic highlands of Vardenis and Syunik share this subduction signature, they have been typically considered to have different sources and magmatic systems based on trace element and Sr-Nd isotope systematics. Sugden et al. (2019) showed that Vardenis and Syunik were similar, but that Syunik was more enriched (in Sr-Nd) and distinct from Vardenis. However, with this new dataset, the Sr and Nd isotopic data shows an almost identical range for both Vardenis and Syunik, suggesting that they may well have similar melt generation mechanisms and sources.. The most significant discrepancy between the highlands is reflected by P_2O_5, which is significantly raised in Syunik compared to Vardenis (this study). It is thought that Syunik is fed by the same apatite-rich source as NW Iran, which causes this difference between the highlands. Vardenis has a very limited range of temperature and depth of melting, suggesting a single, shallow source across the whole highland. In contrast, Syunik (as seen in

Sugden, 2021) has a very wide range in melting temperature and depth, potentially because of more complex melting sources, one of which is shared with Vardenis and the other is apatite-rich and similar to the one common for NW Iran. It is clear that the relationship between Vardenis and Syunik is far more complex than simply distinct volcanic fields.

6.2 Future research

In this investigation, a potential connection between the VVH and SVH has been highlighted, especially in the isotope data. The transition between these adjacent regions should be further interrogated to distinguish if the magmatic systems are connected or just have similar sources. In order to do this, an examination of the geochemistry along a transect from the N of Vardenis, moving south into and across Syunik would be beneficial, to see if there are measurable variations on a scale smaller than the currently identified, inter-highland ones.

I would also recommend a further investigation into this dataset, utilising melt inclusions as a source for isotopic investigation as opposed to whole rock data. This would further minimise the potential impact of alteration, giving the most accurate record of the isotopic ratios in the mantle source. New sampling should also focus on the currently under-sampled regions of south Vardenis, especially those closest to SVH.

7. Bibliography

Allen, M.B., Kheirkhah, M., Neill, I., Emami, M.H. and McLeod, C.L., 2013. Generation of arc and within-plate chemical signatures in collision zone magmatism: Quaternary lavas from Kurdistan Province, Iran. *Journal of Petrology*, *54*(5), pp.887-911.

Aspinall, W., Charbonnier, S., Connor, C.B., Connor, L.J., Costa, A., Courtland, L., Delgado Granados, H., Hibino, K., Hill, B., Komorowski, J.C., McNutt, S., Meliksetian, K., Nakada, S., Newhall, C., Samaddar, S., Savov, I.P., Self, S., Uchiyamer, Y., Wilson, T. and Yamamoto, T. 2016. Volcanic Hazard Assessment for Nuclear Installations: Methods and Examples in Site Evaluation. International Atomic Energy Agency TECDOC series, 1795.

Aydinçakir, E. and Şen, C., 2013. Petrogenesis of the post-collisional volcanic rocks from the Borçka (Artvin) area: implications for the evolution of the Eocene magmatism in the Eastern Pontides (NE Turkey). *Lithos*, *172*, pp.98-117.

Baghdasaryan, G.P. and Ghukasyan, R.K. 1985. Geochrnology of magmatic, metamorphic and ore formations of Armenian SSR. Yerevan: Academy of Sciences of Armenian soviet socialist republic.

Balassanian, S.Y., Arakelian, A.R., Nazaretian, S.N., Avanessian, A.S., Martirossian, A.H., Igoumnov, V.A., Melkoumian, M.G., Manoukian, A.V. and Tovmassian, A.K., 1995. Retrospective analysis of the Spitak earthquake. *Annali di Geofisica*. Volume 38, pp. 345-372

Brenan, J.M., Neroda, E., Lundstrom, C.C., Shaw, H.F., Ryerson, F.J. and Phinney, D.L., 1998. Behaviour of boron, beryllium, and lithium during melting and crystallization: constraints from mineral-melt partitioning experiments. *Geochimica et Cosmochimica Acta*, *62*(12), pp.2129-2141.

Castillo, P.R., 2012. Adakite petrogenesis. *Lithos*, *134*, pp.304-316.

Cohen, R.S. and O'nions, R.K., 1982. Identification of recycled continental material in the mantle from Sr, Nd and Pb isotope investigations. *Earth and Planetary Science Letters*, *61*(1), pp.73-84.

Connor, C., Connor, L., Halama, R., Meliksetian, K. and Savov, I. 2011. Volcanic Hazard Assessment of the Armenia Nuclear Power Plant Site, Final Report. Tampa, FL, USA; Leeds, UK; Yerevan, Armenia.

Davidson, J., Turner, S. and Plank, T., 2013. Dy/Dy*: variations arising from mantle sources and petrogenetic processes. *Journal of Petrology*, *54*(3), pp.525-537.

De Hoog, J.C.M. and Savov, I.P. 2018. Boron Isotopes as a Tracer of Subduction Zone Processes *In*: H. Marschall and G. Foster, eds. *Boron Isotopes: The Fifth Element* [Online]. Springer International Publishing AG, pp.217–247.

Di Giuseppe, P., Agostini, S., Lustrino, M., Karaoglu, Ö., Savaşçin, M.Y., Manetti, P. and Ersoy, Y. 2017. Transition from compression to strike-slip tectonics revealed by miocene-pleistocene volcanism west of the karliova triple junction (east anatolia). *Journal of Petrology*. 58(10), pp.2055–2087

Ewart, A., 1982. The mineralogy and petrology of Tertiary-Recent orogenic volcanic rocks; With special reference to the andesitic-basaltic compositional range. *Andesites: Orogenic Andesites and Related Rocks* 7, pp. 25-98.

Gaetani, G.A. and Grove, T.L., 1998. The influence of water on melting of mantle peridotite. *Contributions to Mineralogy and Petrology*, *131*(4), pp.323-346.

Hawkesworth, C.J. and Vollmer, R., 1979. Crustal contamination versus enriched mantle: 143Nd/144Nd and 87Sr/86Sr evidence from the Italian volcanics. *Contributions to Mineralogy and Petrology*, *69*(2), pp.151-165.

Hu, F., Ducea, M.N., Liu, S. and Chapman, J.B., 2017. Quantifying crustal thickness in continental collisional belts: Global perspective and a geologic application. *Scientific reports*, *7*(1), pp.1-10.

Ishikawa, T. and Nakamura, E., 1994. Origin of the slab component in arc lavas from across-arc variation of B and Pb isotopes. *Nature*, *370*(6486), pp.205-208.

Ishikawa, T. and Tera, F., 1999. Two isotopically distinct fluid components involved in the Mariana arc: Evidence from Nb/B ratios and B, Sr, Nd, and Pb isotope systematics. *Geology*, *27*(1), pp.83-86.

Jacobsen, S.B. and Wasserburg, G.J., 1980. Sm-Nd isotopic evolution of chondrites. *Earth and Planetary Science Letters*, *50*(1), pp.139-155.

Jarosewich, E., Nelen, J.A. and Norberg, J.A., 1980. Reference samples for electron microprobe analysis. *Geostandards Newsletter*, *4*(1), pp.43-47.

Kaislaniemi, L., Van Hunen, J., Allen, M.B. and Neill, I., 2014. Sublithospheric small-scale convection—a mechanism for collision zone magmatism. *Geology*, *42*(4), pp.291-294.

Kakihana, H., Kotaka, M., Satoh, S., Nomura, M. and Okamoto, M., 1977. Fundamental studies on the ion-exchange separation of boron isotopes. *Bulletin of the chemical society of Japan*, *50*(1), pp.158-163.

Karakhanian, A., Djrbashian, R., Trifonov, V., Philip, H., Arakelian, S. and Avagian, A., 2002. Holocene-historical volcanism and active faults as natural risk factors for Armenia and adjacent countries. *Journal of Volcanology and Geothermal Research*, *113*(1-2), pp.319-344.

Karakhanian, A., Jrbashyan, R., Trifonov, V., Philip, H., Arakelian, S., Avagyan, A., Baghdassaryan, H., Davtian, V. and Ghoukassyan, Y. 2003. Volcanic hazards in the region of the Armenian Nuclear Power Plant. *Journal of Volcanology and Geothermal Research*. 126(1–2), pp.31–62.

Kasemann, S., Meixner, A., Rocholl, A., Vennemann, T., Rosner, M., Schmitt, A.K. and Wiedenbeck, M., 2001. Boron and oxygen isotope composition of certified reference materials NIST SRM 610/612 and reference materials JB-2 and JR-2. *Geostandards Newsletter*, *25*(2-3), pp.405-416.

Kelemen, P.B., Hanghøj, K. and Greene, A.R., 2003. One view of the geochemistry of subduction-related magmatic arcs, with an emphasis on primitive andesite and lower crust. *Treatise on geochemistry*, *3*, p.659.

Keskin, M. 2007. Eastern Anatolia: a hot spot in a collision zone without a mantle plume In: G. R. Foulger and D. M. Jurdy, eds. *Plates, plumes and planetary processes*. Geological Society of America Special Paper, pp.693–722.

Keskin, M., Pearce, J.A., Kempton, P.D. and Greenwood, P., 2006. Magma-crust interactions and magma plumbing in a postcollisional setting: geochemical evidence from the Erzurum-Kars volcanic plateau, eastern Turkey. *Special Papers-Geological Society of America*, *409*, p.475.

Keskin, M., Pearce, J.A. and Mitchell, J.G., 1998. Volcano-stratigraphy and geochemistry of collision-related volcanism on the Erzurum–Kars Plateau, northeastern Turkey. *Journal of Volcanology and Geothermal Research*, *85*(1-4), pp.355-404.

Kessel, R., Schmidt, M.W., Ulmer, P. and Pettke, T., 2005. Trace element signature of subduction-zone fluids, melts and supercritical liquids at 120–180 km depth. *Nature*, *437*(7059), pp.724-727.

Kharazyan, E., 2005. Geological map of Republic of Armenia. *Ministry of Nature Protection of Republic of Armenia, Yerevan.*

LaTourrette, T., Hervig, R.L. and Holloway, J.R., 1995. Trace element partitioning between amphibole, phlogopite, and basanite melt. *Earth and Planetary Science Letters*, *135*(1-4), pp.13-30.

Le Bas, M., Maitre, R.L., Streckeisen, A., Zanettin, B. and IUGS Subcommission on the Systematics of Igneous Rocks, 1986. A chemical classification of volcanic rocks based on the total alkali-silica diagram. *Journal of petrology*, *27*(3), pp.745-750.

Lebedev, V.A., Goltsman, Y.V., Oleinikova, T.I., Parfenov, A.V. and Yakushev, A.I., 2021. The Pliocene Post-Collisional Volcanism of Central Armenia: Isotope-Geochronology and Geochemical Evolution of Magmatic Melts. *Petrology*, *29*(6), pp.627-656.

Leeman, W.P., Tonarini, S., Chan, L.H. and Borg, L.E., 2004. Boron and lithium isotopic variations in a hot subduction zone—the southern Washington Cascades. *Chemical Geology*, *212*(1-2), pp.101-124.

Mandler, B.E. and Grove, T.L., 2016. Controls on the stability and composition of amphibole in the Earth’s mantle. *Contributions to Mineralogy and Petrology*, *171*(8), pp.1-20.

Marschall, H.R., Altherr, R., Kalt, A. and Ludwig, T., 2008. Detrital, metamorphic and metasomatic tourmaline in high-pressure metasediments from Syros (Greece): intra-grain boron isotope patterns determined by secondary-ion mass spectrometry. *Contributions to Mineralogy and Petrology*, *155*(6), pp.703-717.

Marschall, H.R., Wanless, V.D., Shimizu, N., Von Strandmann, P.A.P., Elliott, T. and Monteleone, B.D., 2017. The boron and lithium isotopic composition of mid-ocean ridge basalts and the mantle. *Geochimica et Cosmochimica Acta*, *207*, pp.102-138.

McCaig, A.M., Titarenko, S.S., Savov, I.P., Cliff, R.A., Banks, D., Boyce, A. and Agostini, S., 2018. No significant boron in the hydrated mantle of most subducting slabs. *Nature communications*, *9*(1), pp.1-10.

Mederer, J., Moritz, R., Ulianov, A. and Chiaradia, M., 2013. Middle Jurassic to Cenozoic evolution of arc magmatism during Neotethys subduction and arc-continent collision in the Kapan Zone, southern Armenia. *Lithos*, *177*, pp.61-78.

Morimoto, N., Fabries, J., Ferguson, A.K., Ginzburg, I.V., Ross, M., Seifert, F.A., Zussman, J., Aoki, K. and Gottardi, G., 1988. Nomenclature of pyroxenes. *Mineralogical magazine*, *52*(367), pp.535-550.

Neill, I., Meliksetian, K., Allen, M.B., Navarsardyan, G. and Karapetyan, S., 2013. Pliocene–Quaternary volcanic rocks of NW Armenia: magmatism and lithospheric dynamics within an active orogenic plateau. *Lithos*, *180*, pp.200-215.

Neill, I., Meliksetian, K., Allen, M.B., Navasardyan, G. and Kuiper, K., 2015. Petrogenesis of mafic collision zone magmatism: The Armenian sector of the Turkish–Iranian Plateau. *Chemical Geology*, *403*, pp.24-41.

Ni, Y., Foster, G.L. and Elliott, T., 2010. The accuracy of δ11B measurements of foraminifers. *Chemical Geology*, *274*(3-4), pp.187-195.

Pang, K.N., Chung, S.L., Zarrinkoub, M.H., Lin, Y.C., Lee, H.Y., Lo, C.H. and Khatib, M.M., 2013. Iranian ultrapotassic volcanism at~ 11 Ma signifies the initiation of post-collisional magmatism in the Arabia–Eurasia collision zone. *Terra Nova*, *25*(5), pp.405-413.

Paul, A.N., Stewart, J.A., Agostini, S., Kirstein, L.A., De Hoog, J.C.M., Savov, I.P., Walowski, K., Rae, J.W.B. and Elliot, T., 2023. An assessment of the reliability of boron isotopic measurements of silicate samples by multi-collector, inductively coupled plasma mass-spectrometry (MC-ICP-MS). (*under review in GGR*)

Pearce, J.A., 1983. Role of the sub-continental lithosphere in magma genesis at active continental margins. *Continental Basalts and Mantle Xenoliths*, pp. 230-249.

Pearce, J.A., Bender, J.F., De Long, S.E., Kidd, W.S.F., Low, P.J., Güner, Y., Saroglu, F., Yilmaz, Y., Moorbath, S. and Mitchell, J.G., 1990. Genesis of collision volcanism in Eastern Anatolia, Turkey. *Journal of Volcanology and Geothermal Research*, *44*(1-2), pp.189-229.

Pearce, J.A. and Stern, R.J., 2006. Origin of back-arc basin magmas: trace element and isotope perspectives. *Geophysical Monograph-American Geophysical Union*, *166*, p.63.

Plank, T. and Langmuir, C.H., 1993. Tracing trace elements from sediment input to volcanic output at subduction zones. *Nature*, *362*(6422), pp.739-743.

Plank, T. and Langmuir, C.H., 1998. The chemical composition of subducting sediment and its consequences for the crust and mantle. *Chemical geology*, *145*(3-4), pp.325-394.

Prelević, D., Foley, S.F., Romer, R. and Conticelli, S., 2008. Mediterranean Tertiary lamproites derived from multiple source components in postcollisional geodynamics. *Geochimica et Cosmochimica Acta*, *72*(8), pp.2125-2156.

Priestley, K., McKenzie, D., Barron, J., Tatar, M. and Debayle, E., 2012. The Zagros core: deformation of the continental lithospheric mantle. *Geochemistry, Geophysics, Geosystems*, *13*(11).

Ridolfi, F., Renzulli, A. and Puerini, M., 2010. Stability and chemical equilibrium of amphibole in calc-alkaline magmas: an overview, new thermobarometric formulations and application to subduction-related volcanoes. *Contributions to Mineralogy and Petrology*, *160*(1), pp.45-66.

Rolland, Y., 2017. Caucasus collisional history: Review of data from East Anatolia to West Iran. *Gondwana Research*, *49*, pp.130-146.

Rolland, Y., Hässig, M., Bosch, D., Bruguier, O., Melis, R., Galoyan, G., Topuz, G., Sahakyan, L., Avagyan, A. and Sosson, M., 2020. The East Anatolia–Lesser Caucasus ophiolite: An exceptional case of large-scale obduction, synthesis of data and numerical modelling. *Geoscience Frontiers*, *11*(1), pp.83-108.

Rolland, Y., Perincek, D., Kaymakci, N., Sosson, M., Barrier, E. and Avagyan, A., 2012. Evidence for∼ 80–75 Ma subduction jump during Anatolide–Tauride–Armenian block accretion and∼ 48

Ma Arabia–Eurasia collision in Lesser Caucasus–East Anatolia. *Journal of Geodynamics*, *56*, pp.76-85.

Rollinson, H., 1993. Using geochemical data. *Evaluation, presentation, interpretation*, *1*. Routledge, UK.

Rudnick, R.L. and Gao, S. 2003. Composition of the Continental Crust *In*: H. D. Holland and K. K. Turekian, eds. *Treatise on Geochemistry*. Elsevier, pp.659– 723.

Schleiffarth, W.K., Darin, M.H., Reid, M.R. and Umhoefer, P.J., 2018. Dynamics of episodic Late Cretaceous–Cenozoic magmatism across Central to Eastern Anatolia: New insights from an extensive geochronology compilation. *Geosphere*, *14*(5), pp.1990-2008.

Schoenbohm, L.M. 2013. Volume 5: Tectonic Geomorphology of Continental Collision Zones. In: Shroder, J.F. ed. *Treatise on Geomorphology*. Volume 2. Elsevier, pp.120-149.

Şengör, A.C. and Yilmaz, Y., 1981. Tethyan evolution of Turkey: a plate tectonic approach. *Tectonophysics*, *75*(3-4), pp.181-241.

Seyitoğlu, G., Esat, K., Kaypak, B., Toori, M. and Aktuğ, B., 2019. Internal deformation of Turkish–Iranian Plateau in the Hinterland of Bitlis–Zagros Suture Zone. In *Developments in Structural Geology and Tectonics*. Volume 3, pp. 161-244.

Smith, I.E.M. and Németh, K., 2017. Source to surface model of monogenetic volcanism: a critical review. *Geological Society, London, Special Publications*, *446*(1), pp.1-28.

Sokół, K., Halama, R., Meliksetian, K., Savov, I.P., Navasardyan, G. and Sudo, M., 2018. Alkaline magmas in zones of continental convergence: the Tezhsar volcano-intrusive ring complex, Armenia. *Lithos*, *320*, pp.172-191.

Staudigel, H., Davies, G.R., Hart, S.R., Marchant, K.M. and Smith, B.M., 1995. Large scale isotopic Sr, Nd and O isotopic anatomy of altered oceanic crust: DSDP/ODP sites417/418. *Earth and Planetary Science Letters*, *130*(1-4), pp.169-185.

Sun, S.S. and McDonough, W.F., 1989. Chemical and isotopic systematics of oceanic basalts: implications for mantle composition and processes. *Geological Society, London, Special Publications*, *42*(1), pp.313-345.

Sun, S.S., Nesbitt, R.W. and Sharaskin, A.Y., 1979. Geochemical characteristics of mid-ocean ridge basalts. *Earth and Planetary Science Letters*, *44*(1), pp.119-138.

Sugden, P.J. 2021. The geochemistry and geochronology of Quaternary collision-related volcanism in the southern Lesser Caucasus: from development of the mantle source to magma generation and eruption. Ph.D. thesis, University of Leeds.

Sugden, P.J., Savov, I.P., Wilson, M., Meliksetian, K., Navasardyan, G. and Halama, R., 2019. The thickness of the mantle lithosphere and collision-related volcanism in the Lesser Caucasus. *Journal of Petrology*, *60*(2), pp.199-230.

Sugden, P.J., Savov, I.P., Agostini, S., Wilson, M., Halama, R. and Meliksetian, K., 2020. Boron isotope insights into the origin of subduction signatures in continent-continent collision zone volcanism. *Earth and Planetary Science Letters*, *538*, p.116207.

Tonarini, S., Agostini, S., Innocenti, F. and Manetti, P., 2005. δ11B as tracer of slab dehydration and mantle evolution in western Anatolia Cenozoic magmatism. *Terra Nova*, *17*(3), pp.259-264.

Tonarini, S., Pennisi, M., Adorni-Braccesi, A., Dini, A., Ferrara, G., Gonfiantini, R., Wiedenbeck, M. and Gröning, M., 2003. Intercomparison of boron isotope and concentration measurements. Part I: Selection, preparation and homogeneity tests of the intercomparison materials. *Geostandards Newsletter*, *27*(1), pp.21-39.

Tonarini, S., Pennisi, M. and Leeman, W.P., 1997. Precise boron isotopic analysis of complex silicate (rock) samples using alkali carbonate fusion and ion-exchange separation. *Chemical Geology*, *142*(1-2), pp.129-137.

Walowski, K.J., Kirstein, L.A., De Hoog, J.C.M., Elliott, T.R., Savov, I.P. and Jones, R.E., 2019. Investigating ocean island mantle source heterogeneity with boron isotopes in melt inclusions. *Earth and Planetary Science Letters*, *508*, pp.97-108.

Walowski, K.J., Kirstein, L.A., De Hoog, J.C.M., Elliott, T., Savov, I.P. and Jones, R.E., 2021. Boron recycling in the mantle: Evidence from a global comparison of ocean island basalts. *Geochimica et Cosmochimica Acta*, *302*, pp.83-100.

Weis, D., Kieffer, B., Maerschalk, C., Barling, J., De Jong, J., Williams, G.A., Hanano, D., Pretorius, W., Mattielli, N., Scoates, J.S. and Goolaerts, A., 2006. High-precision isotopic characterization of USGS reference materials by TIMS and MC-ICP-MS. *Geochemistry, Geophysics, Geosystems*, *7*(8).

White, W.M., 1995. Geochemical tracers of mantle processes. *Reviews of Geophysics*, *33*(S1), pp.19-24.

White, W.M. and Hofmann, A.W., 1982. Sr and Nd isotope geochemistry of oceanic basalts and mantle evolution. *Nature*, *296*(5860), pp.821-825.

Workman, R.K. and Hart, S.R., 2005. Major and trace element composition of the depleted MORB mantle (DMM). *Earth and Planetary Science Letters*, *231*(1-2), pp.53-72.

Wyss, M. and Martirosyan, A.H., 1998. Seismic quiescence before the M 7, 1988, Spitak earthquake, Armenia. *Geophysical Journal International*, *134*(2), pp.329-340.

Yılmaz, Y., Güner, Y. and Şaroğlu, F., 1998. Geology of the Quaternary volcanic centres of the East Anatolia. *Journal of volcanology and geothermal research*, *85*(1-4), pp.173-210.

Yoshikawa, M., Tamura, A., Arai, S., Kawamoto, T., Payot, B.D., Rivera, D.J., Bariso, E.B., Mirabueno, M.H.T., Okuno, M. and Kobayashi, T., 2016. Aqueous fluids and sedimentary melts as agents for mantle wedge metasomatism, as inferred from peridotite xenoliths at Pinatubo and Iraya volcanoes, Luzon arc, Philippines. *Lithos*, *262*, pp.355-368.

8. Appendices

8.1 Appendix 1 – Full petrographic observations for the new Vardenis dataset.

Sample	Phenocrysts	Groundmass	Alteration	Overall Rock Texture	Groundmass Texture
1.1.19	ol, opx	plag, px, ol	low	Vesicular + porphyritic	Pilotaxitic + intergranular
1.2.19	ol, qtz (xen)	plag, ol, cpx, ox	medium/high - clays in groundmass	Porphyritic	Seriate + intergranular (patches of intersertal)
2.1.19	cpx, ol, amph (pseud)	plag, ol, cpx, ox	low	Porphyritic + rare sub-ophitic phenocrysts	Seriate + intergranular
2.2.19	cpx, ol	plag, ox, ol, clays	high	Porphyritic + glomeroporphyritic + amygdaloidal	Pilotaxitic + intergranular
2.3.19	ol, cpx	plag, cpx, ox	low/medium	Porphyritic + glomeroporphyritic; zoned + sieve texture plag	Sub-ophitic + intergranular
2.5.19	cpx, ol	plag, cpx, ox	low	Microvesicular + porphyritic + glomeroporphyritic; sub-ophitic phenocrysts (rare); sieve-textured plag	Hypocrystalline (30% crystals) + seriate
3.1.19	plag, amph, cpx, ol, kspar	plag, ox, cpx	low/medium - some clay formation	Porphyritic + glomeroporphyritic; rare sub-ophitic phenocrysts	Seriate + intergranular
3.4.19	plag, cpx, ol	50%crystalline, 50%glass	low	Vesicular + porphyritic + hypocrystalline	Hyaline
3.5.19	cpx, amph (pseud), ol, plag (xen), qtz(xen)	plag, ox, ol	high - clays common	Porphyritic + glomeroporphyritic	Dacitic + intergranular + sub-ophitic
4.1.19	plag, cpx, ol	plag, cpx, ol, ox	low	Aphyric + vesicular + xenocrystic	Pilotaxitic + intergranular
4.3.19	plag, ox, cpx, ol	plag, cpx, ox	high - clays common	Porphyritic + glomeroporphyritic + xenocrystic; corona texture on many phenocrysts; sub-ophitic on some phenocrysts; sieve texture on some xenocrysts	Seriate + intergranular
4.4.19	plag, cpx, amph (pseud)	plag, cpx, glass	medium - clays common	Aphyric + devitrified + vesicular	Pilotaxitic + seriate (range of sizes) + intergranular
4.5.19	plag, cpx, ol	plag, cpx, ox, ol	low	Vesicular + devitrified + aphyric	Pilotaxitic + seriate (range of sizes) + intersertal
4.6.19	ol, plag	glass	low	Porphyritic + vesicular	Pilotaxitic + fine-intergranular
4.7.19	plag, bt, ol, cpx	plag, cpx, ol, ox, bt	medium - oxidised ol + zeolite/calcite veins	Porphyritic + glomeroporphyritic + vesicular	Pilotaxitic + intergranular
4.8.19	plag, bt, cpx, ol	plag, cpx, ol, ox, bt	low/medium - some clays	Porphyritic	Pilotaxitic + intergranular
4.9.19	plag, cpx, ol	plag, ox, cpx	low/medium - some oxidation + clays	Porphyritic; sub-ophitic plag & amph phenocrysts	Devitrified + seriate + mostly intergranular w/ some intersertal patches
4.10.19	plag, cpx, qtz, ol	plag, cpx, ox	low (pockets of medium - clays)	Porphyritic + glomeroporphyritic	De-vitrified + hypocrystalline (50% crystals) (thus intersertal)

5.2.19	Aphyric	Glass	N/A	N/A	N/A
6.1.19	cpx, ol	plag, cpx, ox	low (very rare clays)	Porphyritic + vesicular	Sub-ophitic (in places) + intergranular
6.2.19	cpx (xen)	plag, cpx	medium - oxidised ol + clays	Porphyritic + glomeroporphyritic + vesicular	Sub-ophitic + seriate + intergranular
6.3.19	aphyric	plag, ox, bt, px	medium - oxidised ol + clays	Porphyritic + vesicular	Sub-ophitic + pilotaxitic + intergranular
7.1.19	plag, cpx, amph (pseud), ox, qtz (xen)+ ol (pseud)	plag, cpx, ox	low/medium	Porphyritic + glomeroporphyritic + vesicular	Seriate + intergranular
7.2.19	aphyric	plag, px, ox	low	Porphyritic + vesicular	Pilotaxitic + devitrified + intergranular (intersertal in rare areas)
7.4.19	aphyric, qtz (xen)	plag, ol, cpx, ox, glass	low/medium - some oxidation	Aphyric + vesicular	Pilotaxitic + intergranular
7.5.19	plag (xen), qtz (xen), cpx, ol	plag, ox, ol, cpx	low	Porphyritic + xenocrystic; xenocrysts w/ sieve texture (+coronas)	Seriate + intergranular

8.2 Appendix 2

Appendix 2a – Major element data summary for the new Vardenis dataset. Data collected at ALS labs, Vancouver.

Sample	SiO_2	Al_2O_3	Fe_2O_3	CaO	MgO	Na_2O	K_2O	Cr_2O_3	TiO_2	MnO	P_2O_5	SrO	BaO	LOI	Mg#
1.1.19	50.7	16.3	9.48	8.27	6.17	4.27	2.01	0.021	1.34	0.15	0.74	0.15	0.09	0.92	56.3
1.2.19	51.7	16.5	9.11	8.4	6.2	4.5	1.99	0.017	1.34	0.14	0.75	0.15	0.08	0.38	57.4
2.1.19	51.9	17.65	9.12	8.61	4.48	4.21	2.66	0.009	1.13	0.14	0.9	0.19	0.11	0.67	49.3
2.2.19	46.2	17.25	9.82	11.15	6.18	4.11	2.45	0.007	1.31	0.15	0.93	0.19	0.12	0.56	55.5
2.3.19	49.3	16.55	10.55	9.53	6.43	4.3	2.02	0.025	1.25	0.15	0.85	0.18	0.1	0.13	54.7
2.5.19	55.1	16.15	6.9	7.95	4.03	4.69	3.13	0.009	0.9	0.12	0.66	0.17	0.11	1.35	53.6
3.1.19	65	15.85	5.25	4.13	2.09	4.41	3.3	0.005	0.57	0.08	0.31	0.1	0.1	0.23	44.1
3.4.19	64.7	16.5	4.31	4.42	1.68	4.91	3.06	0.004	0.53	0.09	0.34	0.11	0.1	0.6	43.6
3.5.19	55.1	17.2	7.28	7.37	2.87	4.59	2.46	0.011	0.98	0.12	0.72	0.14	0.09	1.29	43.9
4.1.19	59.2	16.55	5.87	5.99	3.18	4.38	2.94	0.009	0.75	0.09	0.51	0.13	0.11	0.6	51.8
4.3.19	58.7	16.6	6.48	4.46	1.98	4.68	2.99	0.011	0.85	0.18	0.56	0.14	0.11	2.76	37.7
4.4.19	57.5	16.45	7.22	5.95	2.94	4.38	2.52	0.006	1.02	0.14	0.64	0.12	0.09	0.41	44.6
4.5.19	53.5	16.9	9.41	7.52	4.29	4.74	2.11	0.008	1.35	0.14	0.79	0.15	0.09	0.1	47.5
4.6.19	52.5	17.25	9.34	7.09	3.43	4.43	2.16	0.006	1.34	0.12	0.75	0.14	0.09	1.11	42.1
4.7.19	51.9	16.35	9.43	7.23	4.16	4.56	2.07	0.009	1.3	0.14	0.77	0.15	0.08	0.08	46.6
4.8.19	53.8	17.2	9.26	7.64	4.01	4.71	2.11	0.006	1.38	0.14	0.8	0.15	0.09	0.39	46.2
4.9.19	57	16.25	7.39	6.15	3.65	4.47	2.83	0.005	0.86	0.12	0.6	0.12	0.1	0.07	49.5
4.10.19	61.8	16.6	5.13	4.88	2.26	4.59	2.7	0.005	0.76	0.05	0.46	0.11	0.1	0.83	46.6
5.2.19	76.7	12	0.88	0.47	0.06	4.14	4.41	0.002	0.1	0.06	0.01	<0.01	<0.01	0.61	11.9
6.1.19	51.9	16.8	9.07	8.08	4.5	4.11	2.61	0.003	1.36	0.14	1	0.22	0.12	0.65	49.6
6.2.19	48.8	15.8	8.29	7.53	4.35	4.1	2.42	0.004	1.24	0.13	0.94	0.2	0.11	0.67	51.0
6.3.19	50.9	16.65	8.73	7.65	4.05	4.2	2.55	0.004	1.3	0.13	0.93	0.21	0.11	0.62	47.9
7.1.19	58.6	15.15	6.42	6.6	3.01	4.69	3	0.008	0.97	0.1	0.72	0.14	0.1	0.31	48.2
7.2.19	58.6	15.5	6.52	5.82	3.06	4.32	2.94	0.007	0.82	0.11	0.61	0.11	0.11	1.25	48.2
7.4.19	56.4	16.9	8.26	6.41	3.78	4.18	2.72	0.013	0.96	0.13	0.72	0.13	0.1	0.9	47.5
7.5.19	54.5	16.15	7.47	6.9	4.28	4.63	2.55	0.013	1.03	0.13	0.78	0.13	0.1	0.23	53.2

Appendix 2b – Trace element data summary for new Vardenis dataset. Data collected at ALS labs, Vancouver.

Sample	Ba	Ce	Cr	Cs	Dy	Er	Eu	Ga	Gd	Hf	Ho	La	Lu	Nb	Nd
1.1.19	744	101	160	0.45	4.4	2.6	1.9	18.6	5.56	4.2	0.92	55.8	0.34	19.8	39.8
1.2.19	751	101	130	0.43	4.34	2.39	1.91	18.8	5.69	4.1	0.9	55.6	0.33	19.8	40.2
2.1.19	964	138.5	70	0.62	3.88	1.98	2.09	20.3	5.79	4.4	0.74	73.5	0.26	26.9	52.6
2.2.19	1025	127.5	50	1.24	4.2	2.09	2.38	20.2	6.81	4.2	0.81	63.2	0.28	27	55.4
2.3.19	853	105	190	0.7	3.8	2.05	1.99	19	5.85	3.3	0.76	52.5	0.26	21.4	46.1
2.5.19	1005	117.5	70	0.92	3.08	1.59	1.66	19	4.84	4.4	0.59	63.8	0.19	27.1	43.7
3.1.19	862	79.4	40	1.66	2.29	1.2	1.1	18.8	3.15	4.2	0.48	45.6	0.19	18.3	29.2
3.4.19	892	91.2	30	1.6	2.55	1.4	1.17	19.6	3.47	5	0.5	49.4	0.22	26.9	33.4
3.5.19	821	105.5	80	0.64	3.25	1.59	1.64	19.2	4.76	3.9	0.61	57.7	0.25	19.8	40.2
4.1.19	934	92.4	60	1.22	2.63	1.38	1.39	18.8	4.04	4.4	0.51	51.3	0.18	18.7	35.6
4.3.19	971	102	80	1.41	2.97	1.57	1.58	19.1	4.62	4.5	0.61	55.1	0.22	21.3	39.4

4.4.19	847	98.7	40	0.47	3.28	1.86	1.53	20	4.61	4.7	0.71	54.8	0.25	20.7	37.7
4.5.19	752	104.5	60	0.25	4.2	2.17	1.8	19.6	5.48	4.2	0.8	56	0.28	20.9	42.3
4.6.19	757	101.5	50	0.24	3.96	2.33	1.88	19.2	5.76	4.2	0.83	56.3	0.3	20.9	42.4
4.7.19	758	107	60	0.18	4	2.1	1.96	19.2	5.83	4.1	0.77	58.5	0.29	21.2	43
4.8.19	827	107.5	40	0.26	4.3	2.37	1.99	18.3	5.35	4.1	0.82	60.6	0.3	21.8	44
4.9.19	920	105.5	40	0.59	3.37	1.85	1.53	17.4	4.36	4.3	0.67	63.3	0.24	20.6	37.8
4.10.19	935	89.3	40	2.11	3.75	2.07	1.56	18	4.81	4.2	0.74	48	0.27	19.6	37.9
5.2.19	32.4	55	20	3.68	1.32	1.03	0.17	14.7	1.16	3.5	0.29	36.9	0.21	34.2	12.6
6.1.19	1080	143	20	0.36	4.22	2.09	2.35	17.6	6.2	4.1	0.79	75.1	0.28	24.1	61.5
6.2.19	1050	138	30	0.36	4.1	1.98	2.13	17.3	6.23	3.9	0.76	73	0.27	22.9	59.1
6.3.19	1075	137.5	20	0.18	4.13	2.12	2.22	18	6.03	4	0.81	73.7	0.27	23.6	57.9
7.1.19	965	110.5	60	1.24	3.48	1.87	1.72	17.6	5.04	4.2	0.69	63.3	0.25	24.2	43.4
7.2.19	998	106.5	50	0.92	3.35	1.8	1.54	17.5	4.52	4.6	0.67	64.4	0.25	22.1	39
7.4.19	929	116	90	0.73	3.74	2.02	1.74	17.9	4.82	4.5	0.73	68	0.29	24.7	43.5
7.5.19	891	115.5	90	0.4	3.76	1.92	1.72	18	4.99	4.6	0.77	67.1	0.28	24.2	43.3

Appendix 2b continued.

Sample	Pr	Rb	Sm	Sn	Sr	Ta	Tb	Th	Tm	U	V	W	Y	Yb	Zr
1.1.19	11.3	32.1	6.99	2	1255	0.9	0.82	4.8	0.35	1.09	182	1	23.5	2.4	206
1.2.19	11.3	32.5	7.13	1	1260	0.9	0.81	4.85	0.34	1.22	180	<1	22.8	2.36	207
2.1.19	15.6	42.7	8.48	2	1655	1.1	0.74	7.93	0.26	1.42	191	1	19.5	1.78	214
2.2.19	15.35	49.6	9.69	1	1635	1	0.85	7.08	0.28	1.72	267	1	21.4	1.97	196
2.3.19	12.45	43	7.76	1	1490	1	0.75	4.64	0.29	1.26	239	<1	19.2	1.84	153
2.5.19	12.95	58.8	6.92	1	1400	1.3	0.62	10.6	0.23	2.87	160	1	16	1.61	213
3.1.19	8.52	88.3	4.45	1	799	1.1	0.43	15.85	0.18	4.84	78	1	12.3	1.21	185
3.4.19	9.86	88.4	5.19	1	922	1.6	0.47	20.4	0.22	5.72	78	2	13.7	1.43	221
3.5.19	11.7	38.5	6.22	1	1230	0.9	0.59	6.6	0.22	1.44	154	3	16.2	1.56	182
4.1.19	10.4	59.4	5.82	2	1060	0.9	0.53	9.82	0.21	2.43	124	1	13.4	1.44	206
4.3.19	11.35	64.6	6.7	1	1065	1.1	0.59	11.5	0.21	2.95	138	1	15.6	1.44	212
4.4.19	10.95	50.1	6.47	1	1045	1	0.67	9.28	0.25	2.17	171	1	18.3	1.82	216
4.5.19	11.95	29.7	7.35	1	1265	0.9	0.79	4.58	0.31	0.96	192	<1	21.4	2.22	202
4.6.19	11.95	34.1	7.67	3	1215	1	0.8	4.73	0.3	1.05	190	<1	21.4	2.09	203
4.7.19	12.3	30	7.38	2	1295	1	0.74	4.71	0.31	1.02	192	1	21.8	2.07	200
4.8.19	13	30.2	7.44	1	1385	1	0.78	5.08	0.31	1.11	204	<1	23	2.09	198
4.9.19	12.05	57.4	6.13	1	1075	0.9	0.62	9.72	0.24	2.21	139	1	18.2	1.68	206
4.10.19	11.05	63.4	6.46	1	989	1.1	0.71	10.95	0.29	2.98	126	1	22.7	1.98	186
5.2.19	5.1	152	1.71	1	15.1	2.2	0.2	28.1	0.2	8.29	<5	3	10.1	1.28	108
6.1.19	18.05	32.6	9.45	1	2020	0.9	0.8	4.38	0.27	1	220	<1	21.5	1.89	196
6.2.19	17.15	32.2	9.35	2	1920	0.9	0.8	4.29	0.29	0.89	199	1	20.9	1.92	190
6.3.19	16.95	32.2	9.19	1	1900	1	0.79	4.51	0.3	0.94	185	<1	21.5	1.8	198
7.1.19	13.05	69.7	7.24	1	1335	1.2	0.68	11.1	0.26	3.7	134	1	19	1.75	197
7.2.19	12.25	68.1	5.99	13	1060	1.1	0.6	11	0.24	2.48	128	1	17.7	1.55	224
7.4.19	13.65	45.9	7.08	9	1205	1.1	0.7	8.54	0.27	2.16	146	1	20.4	1.8	220
7.5.19	13.25	46.3	7.17	1	1215	1	0.74	7.29	0.29	1.67	157	1	20.5	1.79	220

8.3 Appendix 3

Appendix 3a – Individual Olivine grain core and rim averages from EMPA. Zoning type determined by Mg# difference between the core and rim of a single grain; Normal zoning; Reverse Zoning; No Zoning; N/A (only one of core or rim available for that grain). Grain number is the original label of the grain – not necessarily accurate to the EMPA results.

Grain Number	Core or Rim	FeO	SiO_2	MgO	CaO	Cr_2O_3	MnO	TiO_2	Al_2O_3	Na_2O	NiO	**TOTAL**	Mg#
1.2.19													
ol1	C	14.96	40.50	44.52	0.08	0.02	0.25	0.02	0.01	0.00	0.27	100.65	83.92
ol1	R	15.38	40.36	43.87	0.12	0.01	0.47	0.02	0.04	0.02	0.13	100.42	83.14
ol3	C	15.23	40.45	43.97	0.09	0.08	0.24	0.02	0.14	0.02	0.29	100.55	83.51
ol3	R	15.38	40.53	44.03	0.12	0.01	0.48	0.03	0.03	0.01	0.16	100.78	83.18
ol4	C	14.81	40.41	44.30	0.09	0.03	0.27	0.01	0.01	0.00	0.28	100.22	83.97
ol4	R	15.04	40.42	44.04	0.11	0.01	0.42	0.01	0.02	0.00	0.18	100.26	83.55
ol5	C	15.03	40.31	44.55	0.09	0.03	0.28	0.02	0.01	0.00	0.27	100.59	83.83
ol5	R	14.77	40.58	44.54	0.12	0.01	0.42	0.02	0.03	0.01	0.19	100.70	83.93
ol6	C	15.08	40.44	44.52	0.09	0.02	0.25	0.01	0.02	0.01	0.29	100.74	83.81
ol6	R	15.64	40.36	43.65	0.13	0.02	0.51	0.02	0.06	0.02	0.13	100.54	82.81
ol7	C	14.83	40.41	44.64	0.09	0.02	0.29	0.02	0.01	-0.01	0.27	100.57	84.03
ol7	R	15.70	40.43	43.62	0.14	0.02	0.51	0.02	0.06	0.01	0.14	100.65	82.74
ol8	C	15.07	40.41	44.52	0.09	0.01	0.26	0.02	0.02	0.00	0.30	100.70	83.82
ol8	R	14.82	40.48	44.99	0.10	0.02	0.33	0.02	0.03	0.00	0.24	101.02	84.10
ol9	C	15.02	40.56	44.82	0.08	0.03	0.25	0.02	0.02	-0.01	0.30	101.08	83.96
ol9	R	15.36	40.28	44.14	0.12	0.00	0.47	0.02	0.04	0.01	0.14	100.57	83.25
ol10	C	15.09	40.37	44.87	0.08	0.02	0.26	0.00	0.02	0.01	0.26	100.99	83.90
ol10	R	15.38	40.61	44.86	0.12	0.01	0.46	0.02	0.04	0.02	0.15	101.67	83.47
3.4.19													
ol1	C	11.32	41.37	48.46	0.10	0.03	0.16	0.01	-0.01	0.00	0.26	101.70	88.27
ol1	R	13.43	41.09	46.55	0.07	0.04	0.27	0.01	0.00	0.00	0.26	101.73	85.82
ol3	C	12.53	40.79	46.73	0.10	0.02	0.23	0.02	0.01	0.00	0.24	100.66	86.72
ol3	R	13.43	41.54	45.47	0.07	0.02	0.28	0.01	0.02	0.00	0.23	101.06	85.54
ol4	C	11.75	41.10	47.80	0.09	0.04	0.16	0.00	0.00	0.00	0.34	101.30	87.73
ol4	R	15.47	40.48	44.43	0.10	0.02	0.31	0.01	0.01	0.00	0.23	101.05	83.38
ol6	C	21.00	38.76	39.32	0.05	0.01	0.65	0.02	-0.01	-0.01	0.08	99.86	76.40
ol6	R	20.31	39.61	39.72	0.05	0.02	0.66	0.01	0.01	-0.01	0.09	100.46	77.14
px15'	C	18.52	39.25	41.72	0.08	0.02	0.37	0.02	0.01	0.00	0.18	100.15	79.74
px15'	R	16.38	47.10	34.88	0.45	0.00	0.42	0.17	0.65	0.02	0.13	100.20	78.39
4.6.19													
ol1	C	18.22	39.44	41.97	0.08	0.01	0.31	0.01	0.00	0.01	0.18	100.23	80.15
ol1	R	18.47	39.17	41.69	0.08	0.01	0.36	0.01	0.02	0.01	0.17	99.99	79.78
4.7.19													
ol1	C	23.14	38.54	37.72	0.12	0.01	0.80	0.01	0.00	-0.01	0.03	100.35	73.74
ol1	R	23.08	38.74	37.65	0.12	0.01	0.82	0.04	0.01	0.01	0.03	100.49	73.73
ol2	C	23.24	38.34	37.40	0.13	0.00	0.78	0.03	0.01	0.00	0.02	99.96	73.51
ol2	R	23.18	38.49	37.68	0.11	0.00	0.79	0.03	0.00	0.00	0.02	100.31	73.69
ol5	C	22.87	38.37	37.44	0.11	0.00	0.83	0.03	-0.01	0.01	0.03	99.69	73.79
ol5	R	21.77	38.82	38.48	0.11	-0.01	0.81	0.04	0.02	0.00	0.02	100.06	75.23

ol6	C	23.39	38.32	37.57	0.12	-0.01	0.80	0.02	-0.01	0.00	0.03	100.24	73.46
ol6	R	23.05	38.36	37.61	0.11	0.01	0.84	0.03	0.01	0.01	0.03	100.07	73.72
ol7	C	23.30	38.70	37.68	0.12	0.00	0.78	0.02	0.00	0.00	0.02	100.64	73.60
ol7	R	23.35	38.63	37.00	0.11	-0.01	0.84	0.04	0.02	0.01	0.02	100.01	73.16
ol8	C	23.15	38.48	37.67	0.12	0.00	0.78	0.02	0.01	0.00	0.02	100.24	73.72
ol8	R	23.20	38.50	37.55	0.12	0.00	0.80	0.03	0.02	0.01	0.02	100.24	73.60
ol9	C	23.63	38.23	37.04	0.11	0.00	0.82	0.03	0.00	-0.01	0.02	99.88	72.97
ol9	R	23.22	38.85	37.29	0.11	0.00	0.80	0.02	0.01	0.00	0.02	100.34	73.45
ol10	C	23.25	38.56	37.70	0.11	0.00	0.81	0.03	-0.01	-0.01	0.03	100.48	73.63
ol10	R	23.15	38.55	37.66	0.12	0.00	0.82	0.02	0.01	-0.01	0.03	100.34	73.68

Appendix 3b – Individual Clinopyroxene grain core and rim averages from EMPA

Grain Number	Core or Rim	FeO	SiO_2	MgO	CaO	Cr_2O_3	MnO	TiO_2	Al_2O_3	Na_2O	NiO	**TOTAL**	Mg#
3.4.19													
ol2	C	8.41	51.55	15.03	21.79	0.11	0.23	0.58	2.98	0.50	0.02	101.20	73.75
ol2	R	11.19	52.59	15.00	20.05	0.00	0.40	0.46	1.13	0.55	0.01	101.39	69.74
ol5	C	5.93	50.64	15.03	23.01	0.53	0.09	0.99	4.35	0.45	0.02	101.03	81.66
ol5	R	8.79	50.80	14.50	21.61	0.03	0.18	0.87	4.00	0.54	0.02	101.36	74.24
px1	C	9.49	52.46	15.28	20.49	0.02	0.29	0.56	1.97	0.59	0.01	101.15	73.56
px1	R	9.00	51.01	14.94	21.10	0.03	0.21	0.74	3.58	0.49	0.01	101.12	74.29
px2	C	6.41	52.35	15.79	22.41	0.09	0.13	0.68	2.65	0.40	0.03	100.94	81.15
px2	R	7.72	50.34	14.58	22.02	0.12	0.13	1.11	4.44	0.54	0.03	101.03	76.80
px3	C	5.73	52.68	16.11	22.75	0.12	0.12	0.55	2.39	0.37	0.01	100.84	83.08
px3	R	7.98	50.91	14.87	21.53	0.08	0.17	0.90	3.69	0.53	0.02	100.68	76.54
px4	C	5.38	51.71	15.36	23.05	0.56	0.09	0.77	3.18	0.40	0.01	100.52	83.31
px4	R	9.08	50.37	14.55	20.95	0.04	0.19	1.04	3.89	0.58	0.02	100.71	73.68
px5	C	7.39	53.34	16.10	21.38	0.13	0.24	0.46	1.84	0.49	0.03	101.40	78.98
px5	R	8.67	52.92	15.24	21.48	0.00	0.33	0.59	1.86	0.51	0.00	101.60	75.11
px6	C	9.24	53.84	15.99	20.75	0.04	0.48	0.28	1.12	0.41	0.02	102.17	74.57
px6	R	9.54	53.49	15.61	20.47	0.00	0.43	0.45	1.74	0.52	0.01	102.25	73.64
px7	C	9.26	52.97	15.43	21.37	0.02	0.45	0.36	1.41	0.41	0.01	101.69	73.91
px7	R	10.03	52.38	14.85	20.84	0.01	0.42	0.58	2.27	0.53	0.00	101.91	71.67
px8	C	10.30	53.03	15.12	20.50	0.00	0.43	0.51	1.79	0.59	0.01	102.28	71.53
px8	R	9.85	53.10	15.34	21.07	0.00	0.48	0.37	1.17	0.51	0.00	101.90	72.57
px9	C	6.79	49.51	14.17	22.98	0.38	0.10	1.51	5.28	0.50	0.02	101.25	78.56
px9	R	8.53	52.25	15.45	21.63	0.01	0.23	0.62	2.58	0.43	0.01	101.75	75.84
px10	C	6.07	51.64	15.30	23.10	0.33	0.10	0.86	3.77	0.47	0.02	101.65	81.54
px10	R	9.17	50.18	13.99	21.73	0.02	0.19	0.94	4.48	0.58	0.02	101.28	72.71
px11	C	9.53	51.53	14.70	21.12	0.10	0.33	0.79	2.83	0.65	0.01	101.57	72.65
px11	R	7.75	51.01	14.98	22.20	0.11	0.14	0.94	3.83	0.56	0.03	101.55	77.17
px12	C	10.52	51.66	14.52	20.13	0.23	0.33	0.63	2.61	0.73	0.02	101.37	70.45
px12	R	9.79	53.09	15.22	20.83	0.01	0.38	0.42	1.45	0.52	0.00	101.72	72.74
px13	C	8.99	52.90	14.83	22.02	0.05	0.37	0.45	1.92	0.48	0.00	102.00	73.94
px13	R	9.38	52.94	15.97	20.70	0.00	0.35	0.43	1.80	0.34	-0.01	101.90	74.52
px14	C	5.74	51.60	15.52	23.09	0.20	0.08	0.77	3.36	0.41	0.02	100.80	82.60
px14	R	7.24	51.54	15.42	21.95	0.11	0.15	0.74	3.08	0.47	0.02	100.71	78.88

px16	C	8.00	50.57	14.24	22.06	0.71	0.20	0.90	3.80	0.61	0.01	101.11	75.57
px16	R	9.54	53.06	15.54	20.96	0.00	0.41	0.45	1.43	0.46	0.00	101.85	73.58
px17	C	5.67	51.70	15.45	23.40	0.46	0.11	0.81	3.10	0.38	0.02	101.09	82.66
px17	R	6.56	51.43	15.12	22.77	0.18	0.12	0.93	3.70	0.47	0.02	101.30	80.14
ol7	C	8.12	51.28	15.03	21.51	0.12	0.23	0.89	3.17	0.72	0.02	101.09	76.35
ol7	R	8.09	49.56	14.36	21.86	0.13	0.14	1.18	4.33	0.63	0.02	100.31	75.69
ol8	C	9.93	51.99	15.15	20.18	0.01	0.32	0.64	2.06	0.74	0.01	101.03	72.47
ol8	R	9.05	51.41	14.85	21.48	0.03	0.37	0.59	2.53	0.60	0.01	100.90	73.81
4.7.19													
px1	C	8.17	50.82	15.17	20.37	0.42	0.18	0.81	4.49	0.55	0.03	101.00	76.38
px1	R	9.03	51.50	15.55	20.00	0.07	0.26	0.96	3.11	0.57	0.02	101.07	74.87
px2	C	7.73	52.10	16.05	20.52	0.32	0.18	0.56	2.96	0.45	0.03	100.90	78.35
px2	R	8.39	49.35	14.58	20.47	0.58	0.17	1.01	5.30	0.58	0.03	100.47	75.22
px3	C	9.41	48.05	13.65	20.29	0.30	0.18	1.57	6.36	0.58	0.02	100.42	71.71
px3	R	9.06	49.84	14.52	21.36	0.11	0.22	1.26	3.60	0.53	0.00	100.50	73.61
px4	C	9.27	49.51	14.43	20.46	0.20	0.17	1.20	5.17	0.49	0.02	100.92	73.15
px4	R	8.84	50.13	14.19	21.87	0.02	0.19	1.26	3.93	0.48	0.01	100.91	73.62
px5	C	9.31	48.67	13.97	20.30	0.31	0.16	1.33	6.23	0.59	0.03	100.90	72.44
px5	R	8.59	50.14	14.40	21.24	0.16	0.20	1.05	4.24	0.52	0.01	100.53	74.50
px6	C	9.44	48.58	13.89	20.17	0.26	0.17	1.43	6.12	0.59	0.02	100.68	72.03
px6	R	9.21	48.53	13.86	21.63	0.06	0.16	1.39	5.03	0.47	0.02	100.36	72.50
px8	C	8.61	50.63	15.07	20.21	0.23	0.24	1.00	4.25	0.60	0.01	100.86	75.09
px8	R	9.44	50.13	14.66	20.54	0.09	0.26	1.13	4.15	0.63	0.01	101.02	72.77
px9	C	9.52	50.82	15.45	19.28	0.12	0.24	0.93	4.38	0.53	0.02	101.28	73.70
px9	R	9.39	48.45	13.55	21.40	0.10	0.17	1.58	5.78	0.49	0.01	100.91	71.64
px10	C	9.77	48.33	13.66	19.97	0.14	0.18	1.52	6.64	0.60	0.02	100.82	70.99
px10	R	9.30	50.24	14.34	21.20	0.00	0.27	1.37	3.46	0.62	0.00	100.80	72.76
px11	C	8.50	49.57	14.32	20.62	0.45	0.17	1.12	5.43	0.55	0.02	100.75	74.64
px11	R	8.54	49.37	14.17	20.87	0.53	0.17	1.10	5.53	0.60	0.03	100.90	74.37
px12	C	8.32	49.75	14.56	20.56	0.64	0.16	1.01	5.39	0.58	0.02	101.00	75.36
px12	R	8.78	51.05	14.71	21.23	0.34	0.24	1.15	3.61	0.58	0.00	101.68	74.40
ol3	C	9.94	52.85	18.49	16.32	0.17	0.26	0.47	2.42	0.48	0.03	101.41	76.37
ol3	R	9.13	49.80	14.46	20.88	0.19	0.24	1.19	4.43	0.74	0.01	101.07	73.34
ol4	R	9.39	48.47	13.65	20.39	0.16	0.22	1.35	5.99	0.78	0.01	100.41	71.70
3.1.19													
px1	C	7.99	51.07	15.73	20.80	0.17	0.15	0.52	3.50	0.48	0.04	100.44	83.72
px1	R	9.34	50.37	15.67	20.17	0.05	0.18	0.72	3.72	0.38	0.04	100.64	89.61
px2	C	9.92	52.71	14.88	21.52	0.01	0.52	0.22	0.94	0.45	0.01	101.18	88.06
px2	R	9.65	51.26	15.16	20.98	0.01	0.28	0.58	2.39	0.44	0.01	100.76	87.82
px3	C	7.26	51.63	16.07	21.07	0.34	0.15	0.41	3.04	0.47	0.06	100.52	88.21
px3	R	8.05	51.50	15.89	20.91	0.10	0.16	0.46	3.13	0.46	0.05	100.70	90.96
px4	C	7.11	51.82	16.20	21.26	0.42	0.15	0.41	3.04	0.50	0.06	100.97	87.27
px4	R	7.42	51.65	16.04	21.01	0.39	0.14	0.43	3.21	0.51	0.07	100.88	87.87
px5	C	7.42	51.24	15.70	20.72	0.51	0.15	0.44	3.50	0.54	0.05	100.27	87.45
px5	R	7.90	51.68	16.11	20.83	0.10	0.16	0.44	2.86	0.42	0.05	100.56	90.47
px7	C	8.08	50.91	15.36	20.95	0.43	0.16	0.50	3.75	0.53	0.05	100.70	88.22
px7	R	8.02	50.76	15.29	19.96	0.41	0.16	0.45	4.53	0.74	0.05	100.36	90.69
px10	C	8.08	51.36	15.86	19.98	0.19	0.16	0.44	3.66	0.62	0.04	100.40	91.47

px10	R	9.66	52.06	15.04	21.25	0.06	0.34	0.39	1.69	0.44	0.01	100.93	87.05
px11	C	9.43	51.51	14.93	21.06	0.16	0.29	0.40	2.24	0.42	0.03	100.48	87.84
px11	R	9.56	52.21	15.23	21.09	0.04	0.33	0.39	1.71	0.42	0.02	101.00	87.76
px12	C	9.97	52.70	14.54	21.70	0.00	0.58	0.21	0.91	0.42	0.00	101.03	88.30
px12	R	10.17	52.57	14.63	21.57	0.01	0.45	0.23	1.02	0.47	0.00	101.12	88.11
px13	C	9.38	51.15	15.30	20.86	0.04	0.23	0.66	2.52	0.44	0.02	100.59	86.60
px13	R	9.59	51.35	15.25	20.87	0.00	0.26	0.60	2.32	0.44	0.01	100.68	87.11
px14	C	10.18	52.49	14.53	21.42	0.02	0.55	0.21	1.06	0.50	0.01	100.95	89.37
px14	R	9.52	51.42	15.19	20.91	0.01	0.24	0.63	2.28	0.42	0.01	100.63	86.38
px15	C	7.96	51.63	16.22	20.55	0.15	0.18	0.42	2.85	0.45	0.05	100.44	90.07
px15	R	8.05	50.87	15.54	21.23	0.12	0.15	0.57	3.54	0.43	0.05	100.54	90.26
ol1	C	7.86	52.33	15.89	20.93	0.12	0.16	0.48	3.22	0.46	0.05	101.49	90.70
ol1	R	7.89	52.72	16.20	21.01	0.14	0.16	0.41	2.83	0.44	0.05	101.85	90.33
ol2	C	7.36	52.35	15.89	21.16	0.41	0.16	0.42	3.35	0.50	0.04	101.65	88.24
ol2	R	7.84	52.45	16.05	20.93	0.18	0.15	0.43	3.24	0.50	0.06	101.84	90.50
ol5	C	7.91	52.04	15.73	20.79	0.16	0.16	0.52	3.39	0.46	0.05	101.20	89.94
ol5	R	7.88	52.02	15.63	20.66	0.17	0.17	0.47	3.59	0.50	0.05	101.13	90.97
ol6	C	7.66	52.69	16.10	20.50	0.21	0.17	0.41	3.16	0.49	0.06	101.45	90.35
ol6	R	7.77	52.84	16.03	20.75	0.12	0.17	0.41	2.91	0.45	0.05	101.49	90.83
ol9	C	8.00	52.16	15.71	20.91	0.07	0.16	0.52	3.10	0.41	0.04	101.08	90.41
ol9	R	8.14	52.26	15.66	20.95	0.09	0.18	0.49	2.95	0.41	0.03	101.16	90.06
ol10	C	7.92	52.08	15.53	20.59	0.14	0.16	0.55	3.44	0.46	0.04	100.92	89.99
ol10	R	8.30	52.74	16.18	19.78	0.08	0.18	0.38	3.30	0.57	0.05	101.56	92.79
ol11	C	7.94	52.01	16.02	20.37	0.23	0.16	0.51	3.38	0.48	0.05	101.15	89.26
ol11	R	8.21	52.40	15.96	20.50	0.07	0.18	0.45	2.90	0.43	0.05	101.16	90.83

Appendix 3c – Individual Amphibole grain core and rim averages from EMPA.

Grain Number	Core or Rim	SiO_2	TiO_2	Al_2O_3	Cr_2O_3	FeO	MnO	MgO	CaO	Na_2O	K_2O	Cl	F	**Total**	Mg#
3.1.19															
amph1	C	44.44	2.79	12.79	0.05	10.48	0.11	15.13	11.84	2.56	1.00	0.02	0.52	101.73	72.02
amph1	R	45.85	2.17	11.35	0.09	12.15	0.24	14.84	11.60	2.37	1.01	0.03	0.66	102.35	68.52
amph2	C	46.41	3.07	10.60	0.01	11.99	0.20	14.96	11.69	2.67	1.13	0.04	1.56	104.32	68.98
amph2	R	45.93	3.03	10.70	0.00	12.77	0.21	14.52	11.57	2.63	1.09	0.03	2.01	104.49	66.97
amph3	R	43.30	3.41	11.86	0.00	11.86	0.16	14.39	11.69	2.44	1.11	0.03	0.79	101.03	68.39
amph4	C	44.19	3.43	11.53	0.00	12.56	0.18	14.31	11.51	2.50	1.10	0.02	0.78	102.11	66.99
amph4	R	46.19	3.10	11.81	0.01	12.62	0.18	14.08	11.52	2.60	1.09	0.03	1.59	104.82	66.54
amph5	C	43.78	3.11	12.12	0.02	11.58	0.16	14.81	11.57	2.48	1.10	0.02	0.52	101.26	69.51
amph5	R	44.25	2.94	11.89	0.01	11.95	0.19	14.67	11.59	2.54	1.07	0.03	0.90	102.02	68.63
amph7	C	44.35	3.29	11.56	0.07	12.30	0.21	14.36	11.56	2.51	1.08	0.03	0.86	102.18	67.55
amph7	R	44.61	2.66	12.56	0.01	11.18	0.13	14.86	11.64	2.60	0.99	0.02	1.87	103.13	70.32
amph8	C	45.14	3.21	12.23	0.00	11.99	0.15	14.57	11.44	2.55	1.01	0.02	0.56	102.87	68.41
amph8	R	44.58	2.98	11.74	0.02	12.27	0.18	14.40	11.55	2.49	1.07	0.03	0.77	102.09	67.66
amph9	C	44.64	3.09	11.61	0.01	12.12	0.18	14.50	11.55	2.45	1.09	0.03	0.40	101.67	68.07
amph9	R	45.08	3.30	11.23	0.01	12.34	0.19	14.25	11.68	2.55	1.17	0.01	1.56	103.36	67.30
amph10	C	43.82	3.69	11.51	0.00	11.85	0.16	14.40	11.55	2.52	1.14	0.03	0.38	101.06	68.42
amph10	R	43.99	3.40	11.60	0.01	11.94	0.19	14.39	11.53	2.49	1.10	0.03	0.61	101.28	68.23

amph11	C	42.95	3.61	11.59	0.01	11.94	0.18	14.33	11.60	2.51	1.16	0.03	0.40	100.30	68.14
amph11	R	43.52	3.27	11.09	0.01	12.35	0.21	14.58	11.42	2.52	1.13	0.03	1.44	101.58	67.78
amph12	C	43.78	2.79	11.85	-0.01	12.05	0.21	14.59	11.59	2.47	1.10	0.03	0.38	100.83	68.34
amph12	R	44.02	2.74	10.96	-0.01	12.31	0.18	15.07	11.51	2.51	1.09	0.03	1.53	101.94	68.59
amph13	C	43.76	3.22	11.01	0.01	12.14	0.22	14.51	11.44	2.43	1.16	0.03	0.53	100.46	68.06
amph13	R	43.64	3.25	10.81	0.00	12.29	0.23	14.37	11.45	2.37	1.16	0.04	0.41	100.02	67.57
amph14	C	42.82	3.32	12.09	0.03	11.30	0.12	14.72	11.75	2.56	1.01	0.02	0.32	100.06	69.91
amph15	C	43.38	3.06	12.51	0.02	11.69	0.14	14.65	11.70	2.67	1.00	0.02	0.51	101.35	69.09
amph15	R	43.69	3.33	11.51	0.03	12.62	0.19	14.40	11.59	2.67	1.06	0.03	1.34	102.47	67.04
amph16	C	43.59	3.38	12.01	0.03	11.33	0.13	14.73	11.62	2.53	1.03	0.02	0.45	100.85	69.85
amph16	R	44.75	3.30	11.01	-0.01	12.34	0.19	14.55	11.57	2.51	1.12	0.04	1.04	102.40	67.77
amph17	C	41.59	3.07	12.75	0.03	11.87	0.14	14.59	11.48	2.57	0.97	0.02	0.52	101.60	68.66
amph17	R	41.96	2.45	12.17	-0.01	12.86	0.21	14.59	11.40	2.58	0.99	0.03	1.19	102.42	66.91
amph18	C	43.64	3.67	11.40	0.02	11.73	0.18	14.38	11.72	2.57	1.12	0.03	0.42	102.88	68.60
amph18	R	43.02	3.49	11.11	0.01	12.15	0.20	14.42	11.55	2.51	1.12	0.03	0.76	102.38	67.92

4.4.19

amph1	C	43.48	3.30	13.38	0.07	12.07	0.14	15.64	11.23	2.90	0.89	0.01	0.53	103.64	69.79
amph1	R	42.32	3.61	12.59	0.01	12.14	0.16	14.82	11.49	2.65	0.96	0.01	0.83	103.59	68.52
amph2	C	40.86	3.73	12.75	0.01	11.61	0.13	14.45	11.53	2.63	0.99	0.01	1.10	101.80	68.94
amph2	R	42.11	3.76	13.07	0.01	12.23	0.14	14.46	11.46	2.57	0.94	0.01	0.54	103.31	67.82
amph3	C	42.52	3.38	12.53	0.03	12.23	0.15	14.29	11.36	2.59	0.95	0.01	0.41	102.46	67.55
amph3	R	41.28	3.61	12.50	0.01	12.19	0.14	14.35	11.45	2.57	0.94	0.01	0.80	101.86	67.74
amph4	C	41.28	3.32	12.57	0.01	12.77	0.15	14.03	11.44	2.69	0.94	0.02	0.83	102.06	66.21
amph4	R	42.82	3.56	13.25	0.01	12.60	0.13	13.76	11.37	2.61	0.96	0.02	1.03	104.14	66.07
amph5	C	42.25	3.22	12.52	0.00	12.62	0.18	14.02	11.35	2.52	0.93	0.02	0.31	101.93	66.45
amph5	R	41.98	3.63	12.64	0.02	12.01	0.13	14.16	11.46	2.54	0.96	0.01	0.71	102.23	67.77
amph7	C	41.18	3.59	13.03	0.01	12.48	0.13	14.08	11.42	2.65	0.94	0.01	0.90	102.41	66.78
amph7	R	41.63	3.66	12.71	0.01	12.44	0.15	14.04	11.42	2.49	0.96	0.02	0.81	102.34	66.80
amph8	C	41.55	3.89	12.82	0.02	11.61	0.11	14.28	11.60	2.53	0.99	0.01	0.37	101.78	68.67
amph8	R	42.72	3.41	12.32	0.00	10.27	0.16	15.04	11.48	3.06	1.04	0.02	1.68	103.21	72.30
amph9	C	41.43	3.28	12.62	0.02	12.64	0.18	14.39	11.38	2.71	0.95	0.02	0.50	102.09	67.00
amph9	R	42.50	3.30	12.13	0.02	12.72	0.19	14.78	11.33	2.61	0.93	0.02	0.59	103.12	67.45
amph10	C	41.98	3.52	12.44	0.01	12.16	0.16	14.24	11.51	2.61	0.97	0.02	0.56	102.17	67.61
amph10	R	41.82	3.42	12.48	0.01	12.73	0.18	14.16	11.45	2.45	0.98	0.02	0.95	102.63	66.47
amph11	C	42.78	3.52	12.62	0.01	12.14	0.16	14.19	11.43	2.49	0.97	0.02	0.40	102.72	67.56
amph11	R	40.78	3.73	12.63	0.02	11.94	0.13	14.26	11.56	2.54	1.00	0.01	0.49	101.11	68.04
amph12	C	41.78	3.69	12.81	0.00	12.06	0.14	14.17	11.51	2.61	0.99	0.02	0.47	102.25	67.68
amph12	R	42.29	3.66	12.54	-0.01	12.04	0.16	14.32	11.49	2.53	0.97	0.02	0.50	102.51	67.95
amph13	C	41.31	3.71	12.73	0.00	12.06	0.15	14.28	11.49	2.52	0.95	0.01	0.31	101.52	67.86
amph13	R	42.36	3.56	12.60	0.00	12.24	0.15	14.26	11.47	2.46	0.97	0.02	0.63	102.71	67.51
amph14	C	41.93	3.39	12.58	0.00	12.66	0.17	14.01	11.43	2.60	0.98	0.02	0.36	102.14	66.35
amph14	R	42.00	3.66	12.42	0.02	12.04	0.14	14.24	11.49	2.50	0.98	0.02	0.69	102.19	67.83
amph15	C	45.04	3.46	11.97	0.01	12.07	0.19	14.79	11.52	2.67	0.97	0.02	0.39	105.10	68.60
amph15	R	41.59	3.70	12.71	0.01	12.32	0.13	14.11	11.54	2.54	0.96	0.01	0.56	102.17	67.12
amph16	C	42.19	3.02	12.88	0.01	12.90	0.16	13.88	11.48	2.49	0.91	0.02	0.35	102.29	65.74
amph16	R	41.76	3.51	12.84	-0.02	12.62	0.15	14.07	11.39	2.62	0.96	0.01	1.15	103.07	66.52
amph17	C	42.31	3.47	12.50	0.00	12.30	0.18	14.18	11.47	2.58	0.92	0.01	0.52	102.44	67.26
amph17	R	42.74	3.54	12.59	0.01	12.25	0.16	14.13	11.60	2.50	0.99	0.02	0.79	103.31	67.27

amph18	C	43.21	3.36	12.56	0.51	12.28	0.19	14.06	11.49	2.54	0.94	0.02	0.29	103.44	67.13
amph18	R	44.54	3.58	12.55	0.02	12.16	0.17	14.25	11.47	2.52	0.97	0.01	0.33	104.57	67.62
amph19	C	42.50	3.28	12.67	0.00	12.75	0.17	14.02	11.39	2.51	0.95	0.01	0.62	102.88	66.22
amph19	R	42.39	3.67	12.58	0.01	12.24	0.15	14.27	11.64	2.53	0.95	0.01	0.72	103.16	67.52
amph20	C	43.00	3.55	12.86	0.01	12.20	0.17	14.01	11.65	2.59	0.91	0.01	0.61	103.58	67.19
amph20	R	42.77	3.16	12.19	0.00	12.48	0.21	14.11	11.50	2.59	0.96	0.02	0.59	102.58	66.84
amph21	C	43.71	3.25	12.85	0.02	12.95	0.18	14.01	11.25	2.61	0.94	0.02	0.59	104.38	65.86
amph21	R	42.61	3.35	12.20	0.00	12.46	0.19	14.13	11.42	2.58	0.96	0.02	0.73	102.65	66.91
amph22	C	42.83	3.35	12.67	0.00	12.38	0.20	13.80	11.28	2.52	0.98	0.02	0.34	102.36	66.53
amph22	R	43.42	3.33	12.72	1.13	12.15	0.16	13.65	11.24	2.49	0.96	0.02	0.43	103.71	66.70
amph23	C	43.33	3.60	12.85	0.02	12.09	0.16	13.83	11.48	2.59	0.99	0.02	0.34	103.30	67.11
amph23	R	45.11	3.48	12.69	0.00	12.27	0.19	13.06	11.56	2.29	1.00	0.02	0.78	104.45	65.49
amph24	C	41.21	3.48	12.70	0.00	12.45	0.17	13.87	11.43	2.59	0.97	0.02	0.35	101.24	66.50
amph24	R	41.82	3.60	12.37	0.00	12.80	0.15	14.05	11.43	2.48	0.95	0.01	0.96	102.62	66.17

Appendix 3d – Individual Orthopyroxene grain core and rim averages from EMPA.

Grain Number	Core or Rim	FeO	SiO_2	MgO	CaO	Cr_2O_3	MnO	TiO_2	Al_2O_3	Na_2O	NiO	**TOTAL**	Mg#
3.1.19													
ol3	C	11.77	54.13	29.17	0.81	0.17	0.25	0.20	2.85	0.04	0.10	99.49	81.22
ol3	R	11.63	54.71	30.00	0.66	0.11	0.25	0.20	2.22	0.02	0.09	99.90	81.81
ol4	C	12.61	54.53	28.99	0.73	0.03	0.30	0.23	2.16	0.02	0.07	99.68	80.01
ol4	R	12.79	54.52	28.96	0.69	0.04	0.31	0.22	2.11	0.02	0.08	99.73	79.76
ol7	C	19.44	54.09	24.14	0.51	0.00	0.81	0.13	0.45	0.01	0.02	99.59	68.00
ol7	R	17.41	54.29	25.23	0.66	0.02	0.69	0.14	0.71	0.02	0.03	99.19	71.28
ol8	C	19.50	53.90	24.08	0.52	-0.01	0.79	0.14	0.43	0.01	0.01	99.37	67.90
ol8	R	17.05	53.96	25.86	0.57	0.01	0.67	0.17	1.19	0.00	0.01	99.49	72.24
ol10	C	12.70	54.42	28.76	0.70	0.03	0.30	0.18	2.39	0.03	0.08	99.58	79.78
ol10	R	12.52	55.14	29.22	0.69	0.05	0.29	0.19	1.60	0.02	0.06	99.78	80.26
ol12	C	18.61	54.15	24.85	0.53	0.00	0.81	0.14	0.45	0.00	0.02	99.55	69.52
ol12	R	16.14	54.02	26.24	0.79	0.00	0.64	0.26	1.16	0.02	0.02	99.28	73.59
ol13	C	18.98	54.06	24.64	0.53	0.01	0.84	0.15	0.43	-0.01	0.01	99.64	68.90
ol13	R	16.84	54.52	26.33	0.60	0.00	0.71	0.18	0.73	0.00	0.02	99.93	72.78
ol14	C	15.86	54.61	26.99	0.67	0.00	0.63	0.18	0.79	-0.01	0.02	99.73	74.48
ol14	R	16.53	54.23	26.13	0.60	0.00	0.68	0.22	0.97	-0.01	0.01	99.36	73.01
ol15	C	16.14	54.17	26.45	0.71	0.01	0.71	0.20	1.16	0.00	0.02	99.56	73.66
ol15	R	15.37	54.66	26.90	0.76	0.01	0.47	0.18	0.87	0.02	0.02	99.26	75.16
ol16	C	19.46	53.98	24.33	0.51	0.00	0.79	0.12	0.37	0.02	0.01	99.57	68.16
ol16	R	13.89	54.98	27.97	0.89	0.01	0.35	0.18	0.95	0.00	0.05	99.26	77.78
px8	C	11.97	54.16	29.83	0.69	0.06	0.28	0.19	1.82	0.02	0.08	99.10	81.28
px8	R	12.08	53.87	29.53	0.73	0.05	0.27	0.21	1.94	0.02	0.08	98.78	80.99
px9	C	19.91	52.73	24.02	0.50	0.01	0.98	0.17	0.64	0.00	0.01	98.97	67.21
px9	R	17.86	53.17	25.13	0.67	0.01	0.69	0.16	0.72	0.01	0.03	98.43	70.69
3.4.19													
ol9	C	14.96	54.76	27.11	0.78	0.00	0.48	0.27	1.50	0.02	0.01	99.90	75.78
ol9	R	14.89	55.52	27.30	0.75	0.01	0.52	0.21	0.90	0.02	0.01	100.14	75.94

8.4 Appendix 4 – Core and Rim averages for EMPA amphibole data that underwent geothermobarometric calculations using Ridolfi et al. (2010)'s method.

Grain number		T (°C)	uncertainty (σ_{est})	P (MPa)	uncertainty (Max error)	$logfO_2$	uncertainty (σ_{est})	H_2O_{melt} (wt.%)	uncertainty (σ_{est})
3.1.19									
amph1	core	971	22	397	44	-9.8	0.4	5.2	0.8
amph1	rim	921	22	279	31	-10.5	0.4	4.7	0.7
amph2	core	917	22	232	26	-10.9	0.4	3.5	0.5
amph2	rim	917	22	240	26	-10.9	0.4	3.7	0.6
amph3	rim	966	22	336	37	-10.1	0.4	4.1	0.6
amph4	core	948	22	301	33	-10.5	0.4	4.0	0.6
amph4	rim	927	22	305	34	-10.9	0.4	4.8	0.7
amph5	core	964	22	346	38	-10.0	0.4	4.3	0.6
amph5	rim	954	22	326	36	-10.2	0.4	4.3	0.7
amph7	core	947	22	303	33	-10.5	0.4	4.1	0.6
amph7	rim	960	22	376	41	-10.0	0.4	5.1	0.8
amph8	core	947	22	339	37	-10.4	0.4	4.9	0.7
amph8	rim	945	22	314	35	-10.4	0.4	4.4	0.7
amph9	core	943	22	305	34	-10.4	0.4	4.3	0.6
amph9	rim	936	22	278	31	-10.7	0.4	3.9	0.6
amph10	core	956	22	305	34	-10.4	0.4	3.8	0.6
amph10	rim	952	22	311	34	-10.4	0.4	4.1	0.6
amph11	core	967	22	319	35	-10.2	0.4	3.6	0.5
amph11	rim	950	22	279	31	-10.3	0.4	3.4	0.5
amph12	core	956	22	330	36	-10.1	0.4	4.3	0.6
amph12	rim	942	22	266	29	-10.1	0.4	3.4	0.5
amph13	core	944	22	275	30	-10.4	0.4	3.5	0.5
amph13	rim	941	22	265	29	-10.4	0.4	3.4	0.5
amph14	core	979	22	358	39	-9.8	0.4	4.2	0.6
amph15	core	977	22	382	42	-9.9	0.4	4.6	0.7
amph15	rim	957	22	303	33	-10.3	0.4	3.7	0.6
amph16	core	967	22	342	38	-10.1	0.4	4.3	0.6
amph16	rim	936	22	266	29	-10.6	0.4	3.6	0.5
amph17	core	996	22	425	47	-9.4	0.4	4.5	0.7
amph17	rim	977	22	368	40	-9.5	0.4	4.2	0.6
amph18	core	960	22	301	33	-10.4	0.4	3.7	0.6
amph18	rim	958	22	287	32	-10.2	0.4	3.3	0.5
4.4.19									
amph1	core	990	22	423	47	-9.4	0.4	4.5	0.7
amph1	rim	991	22	388	43	-9.6	0.4	4.2	0.6
amph2	core	1011	22	435	48	-9.4	0.4	4.2	0.6
amph2	rim	997	22	435	48	-9.7	0.4	4.7	0.7
amph3	core	980	22	392	43	-9.9	0.4	4.6	0.7
amph3	rim	998	22	404	44	-9.6	0.4	4.3	0.6
amph4	core	995	22	412	45	-9.7	0.4	4.4	0.7
amph4	rim	984	22	454	50	-10.1	0.4	5.4	0.8
amph5	core	978	22	398	44	-9.9	0.4	4.9	0.7
amph5	rim	990	22	411	45	-9.8	0.4	4.7	0.7

amph7	core	1004	22	454	50	-9.6	0.4	4.7	0.7
amph7	rim	993	22	420	46	-9.8	0.4	4.7	0.7
amph8	core	1003	22	433	48	-9.7	0.4	4.6	0.7
amph8	rim	990	22	380	42	-9.7	0.4	3.8	0.6
amph9	core	996	22	408	45	-9.5	0.4	4.2	0.6
amph9	rim	977	22	349	38	-9.7	0.4	4.0	0.6
amph10	core	988	22	393	43	-9.8	0.4	4.4	0.7
amph10	rim	986	22	394	43	-9.8	0.4	4.5	0.7
amph11	core	978	22	398	44	-10.0	0.4	4.9	0.7
amph11	rim	1008	22	426	47	-9.5	0.4	4.2	0.6
amph12	core	997	22	427	47	-9.8	0.4	4.6	0.7
amph12	rim	986	22	395	43	-9.9	0.4	4.5	0.7
amph13	core	1001	22	424	47	-9.6	0.4	4.5	0.7
amph13	rim	984	22	399	44	-9.9	0.4	4.7	0.7
amph14	core	987	22	405	45	-9.9	0.4	4.6	0.7
amph14	rim	987	22	391	43	-9.8	0.4	4.5	0.7
amph15	core	950	22	317	35	-10.4	0.4	4.4	0.7
amph15	rim	997	22	419	46	-9.8	0.4	4.6	0.7
amph16	core	983	22	431	47	-9.8	0.4	5.3	0.8
amph16	rim	993	22	427	47	-9.8	0.4	4.7	0.7
amph17	core	983	22	393	43	-9.9	0.4	4.7	0.7
amph17	rim	981	22	396	44	-10.0	0.4	4.8	0.7
amph18	core	972	22	384	42	-10.1	0.4	5.0	0.7
amph18	rim	958	22	369	41	-10.4	0.4	5.1	0.8
amph19	core	979	22	404	44	-9.9	0.4	4.9	0.7
amph19	rim	988	22	395	43	-9.9	0.4	4.6	0.7
amph20	core	982	22	416	46	-10.1	0.4	5.2	0.8
amph20	rim	971	22	365	40	-10.1	0.4	4.6	0.7
amph21	core	965	22	400	44	-10.2	0.4	5.2	0.8
amph21	rim	973	22	367	40	-10.0	0.4	4.5	0.7
amph22	core	972	22	408	45	-10.2	0.4	5.1	0.8
amph22	rim	965	22	398	44	-10.3	0.4	5.4	0.8
amph23	core	975	22	416	46	-10.3	0.4	5.2	0.8
amph23	rim	943	22	394	43	-11.0	0.4	6.3	0.9
amph24	core	997	22	430	47	-9.7	0.4	4.6	0.7
amph24	rim	985	22	385	42	-9.9	0.4	4.5	0.7